ELECTRONIC STRUCTURE OF PHOSPHORUS, SULFUR AND CHLORINE STUDIED BY HIGH ENERGY RESOLUTION X-RAY EMISSION SPECTROSCOPY

Marko Petric

Doctoral Dissertation
Jožef Stefan International Postgraduate School
Ljubljana, Slovenia

Supervisor: Assist. Prof. Dr. Matjaž Kavčič, Jožef Stefan Institute, Ljubljana, Slovenia

Evaluation Board:
Prof. Dr. Primož Pelicon, Chair, Jožef Stefan Institute, Ljubljana, Slovenia
Prof. Dr. Milena Horvat, Member, Jožef Stefan Institute, Ljubljana, Slovenia
Assist. Prof. Dr. Jakub Szlachetko, Member, Institute of Physics, Jan Kochanowski University, Kielce, Poland

MEDNARODNA PODIPLOMSKA ŠOLA JOŽEFA STEFANA
JOŽEF STEFAN INTERNATIONAL POSTGRADUATE SCHOOL



Marko Petric

ELECTRONIC STRUCTURE OF PHOSPHORUS, SULFUR AND CHLORINE STUDIED BY HIGH ENERGY RESOLUTION X-RAY EMISSION SPECTROSCOPY

Doctoral Dissertation

ANALIZA ELEKTRONSKE STRUKTURE FOSFORJA, ŽVEPLA IN KLORA Z UPORABO RENTGENSKE EMISIJSKE SPEKTROSKOPIJE Z VISOKO ENERGIJSKO LOČLJIVOSTJO

Doktorska disertacija

Supervisor: Assist. Prof. Dr. Matjaž Kavčič

Ljubljana, Slovenia, December 2016

Acknowledgments

In the first place I am very thankful to Matjaž Kavčič, my supervisor; without his guidance, knowledge and support I would not have been able to carry out this work. I am very grateful for his patience and effort which he invested in many conversations during these three years. Also I want to thank all the people from MIC. Matjaž Žitnik for many interesting discussions and advice. Rok Bohinc for his patience when he explained the StoBe program package to me. Also I want to thank to Žiga Barba, Klemen Bučar, Helena Fajfar, Boštjan Jenčič, Mitja Kelemen, Sabina Markelj, Andrej Mihelič, and Anže Založnik for creating a friendly atmosphere at MIC. Mitja Kelemen, Primož Pelicon, and Primož Vavpetič for the help in preparing the protons beam. Franz Gasser and Zdravko Rupnik for constructing the new parallel beam wavelength dispersive spectrometer.

I want to thank my SPRITE friends; Anne-Catherine Wéra, Matthias George, Julien Demarche, Giovanna Muggiolu, Dietrich Walsh, Marios Sotiropoulos, Sérgio Costa Miranda, Victor Alarcon Diez, Djibril Ndiack Fay, Josef Buchriegler, Lidija Matjačić, Valentin Stoytschew and a especially Stanisław Nowak, for nice time during different workshops.

I want to thank Danijela who pushed me to take on this project and Tajana who helped me a lot with English. Finally, I wish to thank my family: my father, my mother, my sister and my grandparents, they have supported me in every moment and I wish to thank Kristina, who became my wife during this thesis, for her support.

This work has been supported by Marie Curie Actions - Initial Training Networks (ITN) as an Integrating Activity Supporting Postgraduate Research with Internships in Industry and Training Excellence (SPRITE) under EC contract no. 317169.

Abstract

In this work the x-ray emission spectroscopy is used to experimentally and theoretically study the electronic structure of phosphorus, sulfur, and chlorine in a series of compounds covering the full range of oxidation states and different local symmetries. High energy resolution $K\alpha$ core-to-core and $K\beta$ valence-to-core x-ray emission spectra were recorded by the Bragg crystal spectrometer in Johansson focusing geometry optimized for tender x-ray range. The experimental energy resolution was comparable to the natural linewidth of the measured emission lines defined by the lifetime of the 1s core hole, which is crucial to resolve the fine structure of the measured spectra reflecting the electronic structure. X-ray emission was induced by irradiating the targets with 2 MeV protons accelerated by the electrostatic Tandem accelerator and also 3 keV monochromatic synchrotron radiation. Experimental K x-ray emission spectra are critically compared to the results of *ab-initio* quantum chemical calculations. Density functional theory is used to calculate the wavefunctions of the molecular system and the calculated structure is discussed in terms of molecular orbital theory. The measured $K\alpha$ spectra exhibit characteristic atomic-like doublet free from chemical bonding effects except for small energy shifts that reflect partial electronic charge and can be used to determine the oxidation state of the investigated element in different chemical environments. Chemical sensitivity is increased further in the $K\beta$ emission spectra probing directly the p-density of occupied valence states. Generally, the main $K\beta$ spectral structure is reproduced by the theoretical model spectra of isolated anions including only the first coordination sphere around the central atom. The effects of hydrogen atoms in the second coordination sphere were observed in the measured phosphorus $K\beta$ emission spectra of different hydrogen phosphates and were explained by the hydrogen covalent bonding to the phosphate ion. The influence of the local geometrical symmetry of the molecular system to the electronic structure was also studied. $K\beta$ emission spectra of P, S, and Cl oxides in T_d, C_{3v}, and C_{2v} local symmetry were measured and characteristic spectral shapes were interpreted by the molecular orbital theory. These results were used in the analysis of a slightly larger more complex molecular system and the measured $K\beta$ spectral shape of a large oxide molecule was successfully explained as a combination of smaller blocks with a well-defined local symmetry. Finally, the potential of x-ray emission spectroscopy to identify and characterize different lithium polysulfides produced electrochemically in a Li-S battery during the discharge/charge is discussed.

Povzetek

V doktorskem delu z uporabo rentgenske emisijske spektroskopije preučujemo elektronsko strukturo fosforja, žvepla in klora v spojinah z različnimi okidacijskimi števili in lokalno geometrijsko simetrijo okolice centralnega atoma. Z Braggovim kristalnim spektrometrom v Johanssonovi geometriji, ki je optimiziran za delovanje v energijskem področju »nežnih« rentgenskih žarkov, smo izmerili emisijske spektre $K\alpha$, ki ustrezajo prehodom med notranjimi elektronskimi nivoji, in spektre $K\beta$, ki ustrezajo prehodom iz valenčnih elektronskih stanj. Eksperimentalna energijska ločljivost merjenih spektrov je bila primerljiva z naravno razširitvijo spektralnih črt zaradi končnega življenskega časa vrzeli v notranji atomski lupini 1s in je omogočila določitev fine strukture merjenih spektrov, ki odraža elektronsko strukturo centralnega atoma. Rentgensko emisijo smo vzbujali z obsevanjem vzorcev s protoni z energijo 2 MeV, ki smo jih pospešili z elektrostatičnim tandemskim pospeševalnikom, in z monokromatsko sinhrotonsko renetgensko svetlobo z energijo 3 keV. Izmerjene spektre smo kritično primerjali z rezultati *ab-initio* kvantno kemijskih računov. Valovne funkcije posameznih molekularnih sistemov smo izračunali s teorijo gostotnih funkcionalov in izračunano strukturo interpretirali v shemi molekularnih orbital. Izmerjeni spektri $K\alpha$ imajo karakteristično atomsko dubletno strukturo in ne kažejo vpliva kemijske vezave, razen drobnih energijskih premikov, ki odražajo efektivni delni naboj in jih lahko uporabimo za določitev oksidacijskega stanja elementa v različnih kemijskih okolicah. Vpliv kemijske okolice je bolj izrazit v emisijskih spektrih $K\beta$, ki direktno odražajo gototo zasedenih valenčnih stanj. V splošnem lahko glavne spektralne oblike dobro opišemo s teoretičnim modelom izoliranega aniona, ki vsebuje zgolj prvo koordinatno sfero okoli centralnega atoma. V primeru različnih vodikovih fosfatov smo opazili vpliv vodikovih atomov v drugi koordinatni sferi na izmerjeno obliko emisijskih spektrov $K\beta$, kar pojasnimo s kovalentno vezjo med vodikovim atomom in fosfatnim ionom. Preučevali smo tudi vpliv geometrijske simetrije okolice na lokalno elektronsko strukturo. Izmerjeno strukturo emisijskih spektrov $K\beta$ fosforjevih, žveplovih in klorovih oksidov v lokalnih simetrijah T_d, C_{3v}, in C_{2v} smo pojasnili s teorijo molekularnih orbital. Te rezultate lahko uporabimo pri analizi bolj kompleksnega molekulskega sistema, kar smo pokazali z analizo emisijskega spektra $K\beta$ večje molekule, ki smo jo opisali s kombinacijo manjših sestavnih blokov z dobro definiranimi lokalnimi simetrijami. Na koncu je predstavljena tudi možnost uporabe rentgenske emisijske spektroskopije za karaterizacijo žveplovih polisulfidov, ki elektrokemijsko nastajajo v ciklu praznjenja/polnjenja Li-S baterije.

Contents

List of Figures **xiii**

List of Tables **xvii**

1 Introduction **1**

2 Theory **7**
2.1 Kramers-Heisenberg Equations for X-Ray Emission Process 7
2.2 Many-Body Systems 10
2.2.1 Thomas-Fermi theory 12
2.3 Density Functional Theory 12
2.3.1 Approximation of exchange-correlation functional 14
2.3.2 Kohn-Sham orbitals 15
2.3.3 StoBe-deMon program package 16
2.3.4 Population analysis 17
2.4 Molecular Orbital Theory 18
2.4.1 Diatomic molecule 19
2.5 Symmetry Classification of Molecules 22

3 Experimental Part **25**
3.1 The PIXE Technique 25
3.1.1 PIXE experimental set-up at JSI 27
3.2 ESRF ID26 Beamline Description 30
3.3 Wavelength Dispersive X-Ray Spectroscopy 32
3.3.1 Dynamic theory of diffraction 34
3.3.2 Different types of WDX spectrometers 37
3.4 Measurements of $K\alpha$ and $K\beta$ XES Spectra of P, S, and Cl Compounds . . 38

4 Results **47**
4.1 Oxidation State Analysis Using Core-to-Core XES 47
4.2 P, S, and Cl Oxides in Different Local Symmetries Studied by Valence-to-Core XES 54
4.2.1 Molecular systems with T_d local symmetry 55
4.2.2 Molecular systems with C_{3v} local symmetry 60
4.2.3 Molecular systems with C_{2v} local symmetry 66
4.3 The Influence of Hydrogen Atoms Breaking the T_d Symmetry of the Phosphate Group 69
4.4 Electronic Structure of Sodium Metabisulfite 73
4.5 X-ray Emission Spectroscopy as a Possible Analytical Tool for Sulfur Speciation in Li-S Batteries 76

5 Conclusions **83**

Appendix A Mulliken Population Analysis of Phosphorus Compounds **87**

Appendix B The Example of StoBe-deMon Code **91**

References **93**

Bibliography **99**

List of Figures

Figure 1.1: *(left)* A schematic picture of x-ray absorption process. Horizontal lines indicate electron levels and blue dots indicate electrons. *(right)* The example of S K-edge XANES spectrum for the ZnS compound. 2
Figure 1.2: A schematic picture of *(left)* electron excitation via photon/proton, *(center)* fluorescence decay of the 1s vacancy. Horizontal lines indicate electron levels and blue dots indicate electrons. *(right)* The example of S Kβ XES spectrum for the ZnS compound. 3
Figure 1.3: Energy levels and corresponding x-ray transitions [8]. 4

Figure 2.1: Comparison of the hydrogen 1s Slater type wavefunction ($\zeta = 1.0$) and corresponding STO-3G. 16
Figure 2.2: (*left*) Two 1s atomic orbitals forming: (*center*) σ bonding orbitals and (*right*) σ^* antibonding orbitals. The blue and red colors represent the positive and negative values of the orbital. 19
Figure 2.3: (*left-up*) Two p atomic orbitals forming: (*center-up*) σ bonding and (*right-up*) σ^* antibonding molecular orbitals. (*left-bottom*) Two p atomic orbitals forming: (*center-bottom*) π bonding and (*right-bottom*) π^* antibonding molecular orbitals. The blue and red colors represent different signs of orbital. 20
Figure 2.4: The molecular diagram of the O_2 molecule with the corresponding valence MO. 21

Figure 3.1: *(left)* The K-shell ionization cross section σ_K for P and Cu atoms as a function of proton energy. *(right)* Comparison of P σ_K ionization cross section calculated with the PWBA and ECPSSR model. 26
Figure 3.2: Blue and green lines depict K- and L-shell fluorescence yields, respectively, as a function of atomic number Z. 27
Figure 3.3: Photo of the laboratory with the accelerator and beamline end stations at the MIC of the JSI. 28
Figure 3.4: Photo of the vacuum chamber of the high energy resolution x-ray emission spectrometer at MIC. 28
Figure 3.5: PIXE spectrum of 1 Slovenian tolar (1 SIT) coin induced with 2 MeV protons. 29
Figure 3.6: Photo of the European Synchrotron Radiation Facility in Grenoble. . . 30
Figure 3.7: The examples of the few sulfur x-ray absorption spectra. 31
Figure 3.8: Linewidths of the atomic K levels [99]. 32
Figure 3.9: Reflection of x-ray on the crystal planes according to the Bragg law. . . 33
Figure 3.10: The basic working principle of the Bragg crystal spectrometer. 33
Figure 3.11: Reflection and transmission of the incident beam on a single atomic layer [102]. 34
Figure 3.12: Symmetric Bragg diffraction from an infinite set of atomic planes [102]. 35

Figure 3.13: The Darwin reflectivity curve calculated without *(green)* and with absorption effects *(blue and red)*. 36
Figure 3.14: The schematic presentation of the Von Hamos (*top*), Johann (*left bottom*) and Johansson geometry (*right bottom*). 38
Figure 3.15: *(left)* The geometrical layout of the JSI tender x-ray emission spectrometer. *(right)* The photo of the spectrometer showing the target holder *(a)*, the analyzer crystal holder *(b)*, and the CCD detector *(c)* [4]. . . . 40
Figure 3.16: *(left)* The CCD image corresponding to $K\alpha$ spectrum of pure S target induced by 2 MeV protons. *(right)* High energy resolution S $K\alpha$ proton-induced spectrum decomposed by the fitting model. The $K\alpha_{3,4}$ satellite line on the high energy side is due to KL double ionization induced in proton-atom collision. 42
Figure 3.17: The examples of the high energy resolution experimental $K\alpha$ *(left)* and $K\beta$ *(right)* x-ray emission spectra of the P, S, and Cl compounds from the top to bottom. 44
Figure 3.18: High resolution $K\beta$ emission spectra of pure S diluted with BN. 45

Figure 4.1: The high energy resolution $K\alpha_{1,2}$ x-ray emission spectra of two P *(upper)*, *S (center)*, and Cl *(bottom)* compounds corresponding to the lowest and the highest oxidation state. All spectra were induced by 2 MeV proton beam. 48
Figure 4.2: *(left)* The experimental and theoretical $K\alpha_1$ emission energies versus formal oxidation state. *(right)* The experimental $K\alpha_1$ emission energies vs DFT calculated number of valence electrons. 51
Figure 4.3: S $K\alpha$ emission spectrum of ZnS / Na_2SO_4 mixed sample fitted with a linear combination of pure ZnS and Na_2SO_4 reference measured spectra. 53
Figure 4.4: P-$K\beta$ emission spectra of four different phosphates induced by *(left)* 3 keV photons and *(right)* 2 MeV protons. 54
Figure 4.5: The presentation (*left*) of the XO_4^{n-} ion with the T_d local symmetry, (*center*) the XO_3^{n-} ion with C_{3v} local symmetry and (*right*) the XO_2 molecule with C_{2v} local symmetry. The investigated atoms X (X=P, S, or Cl) are presented with yellow and oxygen atoms with red. 55
Figure 4.6: Experimental and theoretical $K\beta$ x-ray emission spectra of phosphorus (left), sulfur (center) and chlorine (right) in T_d local symmetry. 56
Figure 4.7: (*left*) Qualitative molecular diagram for the XO_4^{n-} ions, only occupied MO contributing to the $K\beta$ emission spectrum are presented. (*center*) The calculated isosurfaces of electron density for corresponding valence MO are plotted. (*right-up* and *right-down*) Construction of the $4t_2$ and $3t_2$ MOs with atomic X $3p$ and O $2s$, $2p$ orbitals is presented. 59
Figure 4.8: Experimental and theoretical $K\beta$ x-ray emission spectra of phosphorus (left), sulfur (center) and chlorine (right) in C_{3v} local symmetry. 61
Figure 4.9: Theoretical P $K\beta$ emission spectra of Na_2HPO_3 with different distances between the Na_2PO_3 molecular fragment and the hydrogen atom. The calculated stick spectra were convoluted with 0.9 eV FWHM Gaussian function. 63
Figure 4.10: Schematic arrangement of X $3p_z$ and O $2s$ orbitals producing zero overlap. 63
Figure 4.11: (*left*) Qualitative molecular diagram for the XO_3^{n-} ions, only occupied MO contributing to the spectrum are presented. (*center*) The calculated isosurfaces of electron density for corresponding valence MO are plotted. (*right*) The schematic presentation of the $3e$ and $7a_1$ MO. . . . 65

Figure 4.12: Experimental *(green)* P $K\beta$ emission spectrum of $CaH_4O_4P_2$ compared to the theoretical model *(blue)* calculated for the $H_2PO_2^{1-}$ ion. 68
Figure 4.13: Theoretical spectra of (left) SO_2 and (right) ClO_2^+ molecule. The calculated stick spectra were convoluted with the Gaussian function. . . . 69
Figure 4.14: Theoretical spectra of (from bottom to top) PO_4^{3-}, HPO_4^{2-}, $H_2PO_4^{1-}$ and H_3PO_4 phosphate ions. Geometrical structure of the molecule is presented on the left with green, red and white representing the P, O and H atoms, respectively. The development of the $4th$ ($5a_1$) orbital building, the $K\beta'$ peak is presented on the right side. The red and blue color represent the negative and positive values of the wavefunction. . . 70
Figure 4.15: Experimental P $K\beta$ emission spectra of *(left)* K_3PO_4, *(right)* Na_2HPO_4 and *(botton)* NaH_2PO_4 compared to theoretical model spectra *(blue)*. . 72
Figure 4.16: P $K\beta$ emission spectrum of H_3PO_4 measured by Sugiura [47]. 73
Figure 4.17: (*top*) The experimental and (*bottom*) the theoretical S $K\beta$ emission spectrum of the $Na_2S_2O_5$ molecule, with the model of $Na_2S_2O_5$ molecule, where yellow, red, and brown represent S, O, and Na atoms, respectively. 75
Figure 4.18: (*left*) Schematical picture of a Li-S battery cell. (*right*) Voltage profiles of Li-S battery. During discharge sulfur is reduced by Li to reach the final discharge product Li_2S [28]. 77
Figure 4.19: (*upper*) The high energy resolution S $K\alpha$ spectra of α-S_8 and Li_2S compounds. (*bottom*) The experimental $K\alpha_1$ x-ray emission energies versus the effective oxidation state. 78
Figure 4.20: Experimental and theoretical S $K\beta$ emission spectrum of α-S_8 sample. 80
Figure 4.21: Theoretical S $K\beta$ x-ray emission spectra of Li_2S_2 (*left-up*), Li_2S_3 (*right-up*), Li_2S_4 (*left-bottom*), and Li_2S_5 (*right-bottom*) polysulfides. 81

List of Tables

Table 2.1: The orbital and auxiliary basis set for elements building the molecules studied in this thesis. 17

Table 2.2: Differences between the results of Mulliken (**M**) and Loewdin (**L**) population analysis for the phosphorus $5a_1$ orbital within the PO_4^{3-} ion using different phosphorus basis sets. 18

Table 2.3: The character table of the T_d point group. 22

Table 2.4: The character table of the C_{3v} point group. 22

Table 2.5: The character table of the C_{2v} point group. 22

Table 3.1: Coefficients for Bambynek semi-empirical formula used to calculate the fluorescence yield [8]. 27

Table 3.2: The calculated Darwin widths of silicon and germanium crystals for different crystal cuts [102]. 37

Table 3.3: The chemical formula and the name of compounds used in this thesis. . 39

Table 4.1: The experimental $K\alpha_1$ emission energies of various phosphorus, sulfur and chlorine compounds extracted from the fit. 49

Table 4.2: Calculated energy position of $K\alpha_1$ lines and DFT-calculated valence electron population of the first coordination sphere of P compounds. . . 49

Table 4.3: Calculated energy position of $K\alpha_1$ lines and DFT-calculated valence electron population. 50

Table 4.4: The DFT calculated distances between central P, S, Cl atom and neighboring oxygen atoms in XO_4^{n-} and XO_3^{n-} ions and in neutral molecules. Existing literature crystallographic data is added for comparison. 55

Table 4.5: Extracted experimental energies and relative intensities of main spectral components for the K_3PO_4, K_2SO_4 and $KClO_4$ compounds. The error estimates from the fit are given in parentheses. 57

Table 4.6: The overall shift of the absolute energy scale applied to each calculated XO_4^{n-} and XO_3^{n-} spectrum. 57

Table 4.7: Ground state electronic configuration of separate XO_4^{n-} ions with T_d local symmetry performed by Mulliken population analysis. For comparison ground state electronic configuration of corresponding neutral molecules is also given. Contribution of particular MO to the corresponding spectral components is noted in the first column. 58

Table 4.8: Extracted experimental energies and relative intensities of main spectral components for the Na_2HPO_3, Na_2SO_3 and $NaClO_3$ compounds. The fitting errors are reported in parentheses. 62

Table 4.9: Ground state electronic configuration of separate XO_3^{n-} ions with C_{3v} local symmetry performed by Mulliken population analysis. For comparison ground state electronic configuration of corresponding neutral molecules is also given. Contributions of particular MO to the corresponding spectral components are noted in the first column. 64
Table 4.10: Experimental energies and intensities of the main spectral components for $CaH_4O_4P_2$ together with the average atomic character of the group of transitions building the model spectra. 67
Table 4.11: Ground state electronic configuration of separate SO_2 and ClO_2^+ molecule obtained by Mulliken population analysis. Contribution of particular MO to the corresponding spectral components are noted in the first column. 67
Table 4.12: Atomic orbital contributions to the molecular orbitals in PO_4^{3-}, HPO_4^{2-}, $H_2PO_4^{1-}$ and H_3PO_4 used to build the model spectra. The $1t_1$ and $4a_1$ orbitals are omitted since they do not contribute to the spectra. 71
Table 4.13: Experimental energies and intensities of the main spectral components for the phosphate group along with the average atomic character of the group of transitions building the model spectra. The error estimates from the fit are given in parentheses. 74
Table 4.14: Experimental energies and intensities of the spectral components together with the average atomic character of the group of transitions building the $Na_2S_2O_5$ model spectrum. The error estimates from the fit are given in parentheses. 76
Table 4.15: Electron density on the various Li_2S_x polysulfides calculated by Bader analysis. 79
Table 4.16: The results of Mulliken population analysis for the Li_2S_x compounds. In the last column the difference between the electronic charge on the terminal and internal sulfur atoms is given. 79

Table A.1: Atomic orbital contributions to the molecular orbitals used to build the K_3PO_4 model spectra. Besides atomic character calculated energies and intensities corresponding to electronic transition to 1s atomic orbital are also given. An overall shift of absolute calculated energies by -3.61 eV used to match experimental energies is already applied in the tabulated energies. 87
Table A.2: Atomic orbital contributions to the molecular orbitals used to build the Na_2HPO_4 model spectra. An overall shift of absolute calculated energies by -4.35 eV is already applied. 88
Table A.3: Atomic orbital contributions to the molecular orbitals used to build the NaH_2PO_4 model spectra. An overall shift of absolute calculated energies by -4.38 eV is already applied. 88
Table A.4: Atomic orbital contributions to the molecular orbitals used to build the KH_2PO_4 model spectra. An overall shift of absolute calculated energies by -3.77 eV is already applied. 89
Table A.5: Atomic orbital contributions to the molecular orbitals used to build the HPO_3^{2-} model spectra. An overall shift of absolute calculated energies by -3.89 eV is already applied. 89
Table A.6: Atomic orbital contributions to the molecular orbitals used to build the $H_2PO_2^{1-}$ model spectra. An overall shift of absolute calculated energies by -3.36 eV is already applied. 89

Chapter 1

Introduction

Inner shell x-ray spectroscopies are based on the ionization of the atomic inner-shell. An inner shell electron can be excited by an x-ray absorption or scattering, in an atom collision with electron or ion, and in some isotopes also by an electron capture. An atom with the inner shell vacancy is extremely unstable and its characteristic lifetime is 10^{-15} s, and the inner vacancy is subsequently filled with the electron from a higher occupied electronic state. When an electron from higher energy level is transferred into the inner shell, it releases energy. The decay can be non-radiative (Auger decay) when the released energy is transferred to another electron from higher energy level, which is ejected from the atom. The result of Auger decay are two vacancies in higher shell. If the released energy is emitted by an x-ray photon, we talk about radiative (fluorescence) decay. X-ray analytical techniques are based on the detection of emitted x-rays whose energies are given by the energy difference of the electron states in the transition, bulding characteristic atomic lines in the emitted x-ray spectrum. Intensities of these characteristic lines are used to determine the elemental composition of the target. These x-ray fluorescence techniques use solid-state energy dispersive Si(Li) x-rays detectors with typical energy resolution around 150 eV at energy of few kiloelectronvolts (keV)[1]. This resolution is good enough to resolve separate emission lines needed to determine elemental concentrations. However, at such resolution the emission spectra are not sensitive to the chemical environment of the x-ray emitting atom and a different experimental approach is required to also study its electronic structure.

At the moment x-ray spectroscopies, in particular x-ray absorption spectroscopy (XAS), are a standard technique implemented on third-generation synchrotron radiation sources to probe local electron density and local symmetry around the center atom. The core levels of different atoms are very well separated in energy, consequently the method is element selective. Because of a large penetration depth of keV x-rays, the XAS technique is bulk sensitive. High sensitivity is provided by the large absorption cross section and high photon fluxes delivered by the third generation synchrotron sources. Therefore, the method can be successfully applied also to diluted samples.

From the experimental view, the tunable monochromatic source of x-ray photons with high energy resolution is needed to perform XAS measurements. The energy resolution of incoming photons provided by the beamline monochromator is around $\Delta E/E \approx 10^{-4}$. There are two possibilities for measuring the absorption coefficient: transmission and total fluorescence yield (TFY) approach. In transmission mode the absorption coefficient is directly determined according to the Beer's law:

$$I(z) = I_0 \mathrm{e}^{-\mu z} \tag{1.1}$$

where I_0 is the intensity of incoming photon beam and $I(z)$ is the intensity transmitted through the sample of a thickness z. In case of third-row elements studied in this work,

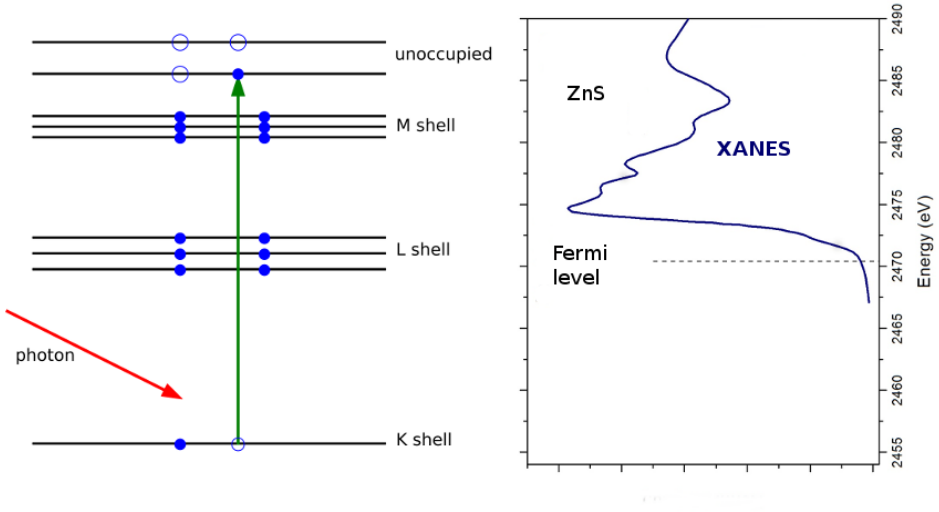


Figure 1.1: *(left)* A schematic picture of x-ray absorption process. Horizontal lines indicate electron levels and blue dots indicate electrons. *(right)* The example of S K-edge XANES spectrum for the ZnS compound.

the K absorption edge lies in tender x-ray range (between 2-5 keV) and the absorption in the sample is too strong for transmission measurements. The absorption coefficient can then be approximately determined by measuring the fluorescence yield, while scanning the energy of incident beam across the corresponding edge. In this type of measurements the fluorescence yield is proportional to the absorption coefficient.

The XAS spectrum is commonly divided into two parts, x-ray absorption near edge structure (XANES) and extended x-ray absorption fine structure (EXAFS). The XANES is a region of spectrum around the edge and the shape of the spectrum reflects the density of the unoccupied molecular orbitals. The basis of the XANES technique is a process of the absorption of x-ray photon by the atom, where the electron is transfered from core orbitals to unoccupied states above the Fermi energy, Figure 1.1. The electron transition needs to satisfy the dipole selection rules for the atomic orbital momentum. This part of the spectrum contains chemical information, for example the energy position of the edge represents oxidation state and the shape of spectrum can be a fingerprint of the local symmetry of the investigated atom. The EXAFS region starts around 100 eV above the edge and can be some thousands eV long. Characteristic for this region are photoelectrons which propagate as spherical waves. After the absorption of an energetic x-ray photon, atom emitted photoelectron waves, which are backscattered by neighboring atoms, produce interferences. The interferences are detected like oscillations in EXAFS tail and after the Fourier analysis had been made, the atomic number, distance and coordination number of neighboring atoms can be determined [2], [3].

Alternatively, electronic structure and chemical state can be studied also with x-ray fluorescence techniques when the energy dispersive detectors (with $\Delta E/E \approx 2 \times 10^{-2}$) are replaced with high energy resolution x-ray emission spectrometer (with $\Delta E/E \approx 1 - 2 \times 10^{-4}$ [4]). The energy window of the spectrum is reduced to only a few eV and we are concentrated on only one element. However, the resolution at the level of natural lifetime broadening allows us to study small shifts and details in the spectral shape of emission spectra. These effects can be correlated with chemical environment of the atom. This technique is called high resolution x-ray emission spectroscopy (XES). The emission is a second-order process which occurs after inner shell ionization of the target atoms.

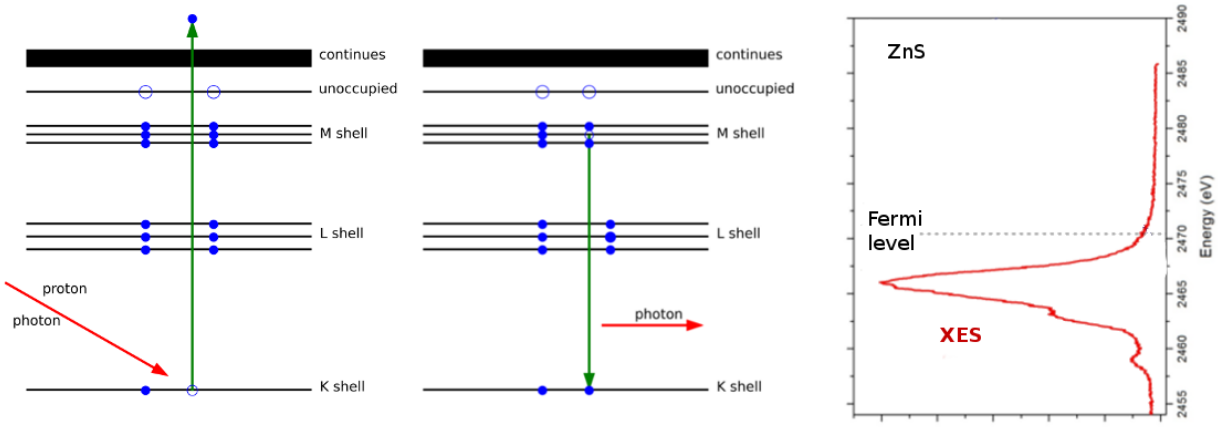


Figure 1.2: A schematic picture of *(left)* electron excitation via photon/proton, *(center)* fluorescence decay of the 1s vacancy. Horizontal lines indicate electron levels and blue dots indicate electrons. *(right)* The example of S Kβ XES spectrum for the ZnS compound.

In contrast to XANES, XES probes the occupied electronic states below the Fermi level, Figure 1.2. Both techniques provide complementary information on the electronic structure and choice of the technique depends on the information one is looking for. However, there is one important experimental difference between these two techniques. XAS spectroscopy relies on the usage of a monochromatic tunable x-ray source which is available only at synchrotron facilities [1]. On the other hand, the XES is based on a second-order process and is therefore not restricted to synchrotron facilities, but can also be used in combination with laboratory excitation sources.

XES spectroscopy can therefore also be combined with MeV proton excitation, which is available at the Jožef Stefan Institute in Ljubljana. The particle (in our case protons) induced x-ray emission (PIXE) is a multielemental, fast, non-destructive and relatively inexpensive analytical technique commonly used to determine the concentration of the elements in the samples. Different elements are distinguished by the characteristic energies of x-ray emission lines building the PIXE spectrum. This was first established already by Moseley's empirical law [6], connecting the frequency of the $K\alpha$ emission line with the atomic number

$$\nu_{K\alpha} = KR_{\infty}c(Z-\sigma)^2. \tag{1.2}$$

Here $K = \frac{3}{4}$ for $K\alpha$ lines, σ is approximately equal to 1 and $R_{\infty} = (\frac{1}{4\pi\epsilon_0})^2 me^4/4\pi\hbar^3 c$ is the Rydberg constant. With the increasing number of protons (Z) in the atom nuclei, the characteristic emission energy also increases. The law is historically important because it established the definite order of chemical elements in a period table. Until Moseley's work, the position of an element in the periodic table was evaluated by the weight and not the atomic number. This is demonstrated in a famous cobalt and nickel example, where the measurements of the $K\alpha$-line energies (cobalt = 6.930 keV and nickel = 7.477 keV) established a correct order of the cobalt-nickel position [7].

The spectroscopic nomenclature of the characteristic emission lines building the PIXE spectrum is based on the Bohr model of an atom. The electron energy levels in the atom are quantized according to the following equation

$$E_n = -R_{\infty}hc\frac{M}{M+m}\frac{Z_{eff}^2}{n^2} \quad , \quad n = 1, 2, 3, \cdots \tag{1.3}$$

[1] Recently, also x-ray tube-based instrumentation for XAS spectroscopy in the transmission mode has been introduced for hard x-ray range [5].

where m is the electron mass and M is the nucleus mass. The lowest occupied electronic level has the principal quantum number $n = 1$ and corresponds to the K-shell, followed by the next two higher energy levels with the principal quantum numbers $n = 2$ and $n = 3$ corresponding to the L and M shells, respectively. The vacancy can be spontaneously filled by electron dipole transition from higher energy level. The emission lines which are generated by filling the vacancy in the K-shell from L and M shells electrons correspond to $K\alpha$ and $K\beta$ spectra, respectively. This is schematically represented in Figure 1.3. In case of third-row elements studied in this work only K lines are relevant for x-ray analysis and in this case the $K\alpha$ and $K\beta$ can be described as core-to-core (CtC) and valence-to-core (VtC) electron transitions, respectively.

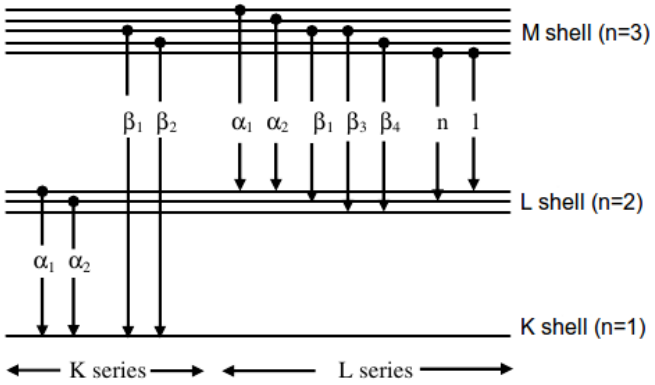


Figure 1.3: Energy levels and corresponding x-ray transitions [8].

Currently, electronic structure studies employing XES are driven by fast instrumental development. For this purpose several large in-air Johann type x-ray emission spectrometers have been developed at several synchrotron facilities. Since these spectrometers are limited to hard x-ray region, most of the XES studies are focused on the $3d$-transition metal complexes, with corresponding emission lines in the hard x-ray range [9], [10]. The characteristic emission lines of third-row elements studied in this work are situated at lower energies in the so-called tender x-ray range (2-5 keV). At these energies in-air emission spectrometers are not applicable due to enhanced in air x-ray absorption and full in vacuum environment is mandatory. Consequently, this energy range has not been scientifically exploited so far to the same extent as the hard x-ray range. We would like to fill this gap and also push the XES technique towards the tender x-ray range and address the electronic structure of three chemically and biologically very relevant elements, phosphorus (P), sulfur (S), and chlorine (Cl).

The P, S, and Cl with their wide range of oxidation states form chemical bonds with a variety of atoms of different electronegativity. These three elements are the essential elements for all living systems. The P and S are two of the six macronutrients present in plant tissues in relatively large amounts and Cl belongs to the group of micronutrients also necessary for plant growth [11]. The plants take up P and S minerals by plant roots from the soil solution as phosphate (PO_4^{3-}) and sulfate (SO_4^{2-}). Commonly, P remains in its oxidised form, where S in the reducing environment created by floods can give rise to sulfides such as FeS, FeS_2 and H_2S [12]. The phosphate group has an important role in plant hormones which regulate plant growth and development [13]. Phosphate group is also crucial for the adenosine triphosphate (ATP) molecule being the reservoir of biochemical energy [14]. The production and distribution of the plankton in the world's ocean primarily depends on the availability of phosphorus [15]. Deposition of P from aerosols to oceanic

ecosystem changes bioavailability of P. One of the most important roles of phosphorus is that of ocean photosynthesis. The chemical equation can be written as

$$106CO_2 + 16HNO_3 + H_3PO_4 + 122H_2O + \text{trace elements} \xrightarrow{light} C_{106}H_{263}O_{110} + 138O_2$$

Thus, the availability of P in marine systems can strongly influence the marine carbon cycle and the sequestration of atmospheric carbon dioxide [16]. We can emphasize two phosphorus-based products which are important for human civilization, match [17] and fertilizers containing phosphorus [18]. It can be assessed that 90% of industrial production of the phosphorus is for the fertilizers involved in food production [19].

The sulfur is not only important for plant growth, but also for the human body. For example, in vital enzyme for human health like cysteine dioxygenase [20], or in thyroid hormones [21], which are essential for the development and differentiation of all cells of the human body the sulfur plays an important role. On the other hand, the major source of the world's metals are the metal sulfide minerals, which result in an extensive study of chemical properties of the sulfide minerals with different spectroscopy techniques [22]–[25]. The climate changes are closely related to water activity and droplets of water in the atmosphere, where the sulfate molecules affect significantly the hydrological cycle [26] and sulfuric acid is crucial in the formation of new particles in the atmosphere [27]. From the industrial aspect the speciation of sulfur is also of great interest. For example, for new generation of Li-S batteries [28] the sulfur plays a critical role. Different forms of sulfur are important components of petroleum and coal hydrocarbons and have been widely studied in these systems to solve environmental problems [29]–[31].

Maybe the most famous compound of chlorine is life's essential salt (NaCl). The chlorine also appears in the daily life in chlorination water to protect the public from outbreaks of waterborne disease [32]. In the agriculture it is a base for various pesticides and herbicides [33]. More than 1500 organochlorines exist, which are involved in the structure of the ubiquitous fungal and plant's metabolite to the life-saving antibiotic [34]. Perchlorate and chlorate compounds are involved in the oxidation process of organic matter and they are ubiquitous all across the Earth' surface [35]. Recently, (per)chlorate was extracted also from non-planetary samples [36]. From the industrial aspect it is important to highlight the group of chlorinated hydrocarbons (CHC) including the polyvinyl chloride (PVC), which is one of the widely produced synthetic plastic polymers [37]. Also, the group of chlorofluorocarbons (CFCs) is often used in the chemical industry, but these compounds from the environment drift into the stratosphere, where they decompose to free chlorine radicals. The chlorine radicals react with oxygen in the ozone and result in serious environmental problems [38].

In order to characterize this particular group of compounds and understand their role in the chemical processes, a detailed knowledge of the chemical environment of central atom is of prime importance. X-ray analytical techniques, in particular XES, can be successfully applied to characterize the electronic structure of these elements in different materials. As it is based on inner-shell ionization the method is element selective, a relatively large penetration of x-rays enables the analysis of bulk materials and provides compatibility with in-situ conditions. Currently, the main limitation is the availability of high quality tender x-ray emission spectrometers because of several experimental constraints imposed by this specific x-ray range.

Consequently, only a few authors used the XES method for chemical speciation of the P, S, and Cl. For example, the $K\alpha$ line was used to specify the oxidation state in some P [39], [40] and S [41], [42] compounds. It was shown that XES combined with proton excitation (high resolution PIXE) can be applied to oxidation state analysis of S in aerosol sample [41], [43]–[45] or P in lake sediments [40]. All of these studies were based on the

fingerprint approach using the comparison with measured standards. Only recently, in the work of Alonso Mori *et al.* [46] *ab-initio* calculations were used to explain the chemical shift of S $K\alpha$ line. They show that the chemical shift arises from screening effects, the energy of the core level is modified by the change of the electron density in the valence band. Similar as $K\alpha$, also $K\beta$ XES measurements using different excitation sources were performed to try to specify chemical state of P, S, and Cl in some materials. Also, the empirical approach was used to interpret the spectra, as for example in the analysis of phosphate/phosphite [47]–[50], sulfate/sulfite [50]–[53] and (per)chlorate [53] compounds. Some theoretical interpretations based on the *ab-initio* quantum chemical calculations were performed only by a few authors for P [54], S [55]–[57], or Cl [55] elements.

The main goal of this thesis is to spread the applicability of XES spectroscopy for electronic structure analysis also in the tender x-ray range, which has so far not been well exploited. In addition, XES spectroscopy is coupled with MeV proton excitation in order to enhance further the analytical capabilities of PIXE technique also towards chemical state analysis. A thorough and systematic experimental and theoretical XES study of electronic structure of P, S, and Cl in different compounds is provided. The approach presented in this work can be used in the analysis of different materials from several research areas.

Chapter 2

Theory

In this chapter the theoretical framework used to interpret the measured emission spectra is introduced. The basic equation of the x-ray emission process is obtained from the more general Kramers-Heisenberg equation describing x-ray scattering. In this picture x-ray emission is described as x-ray scattering following excitation into non-bound states. This approach can be generalized for x-ray fluorescence following inner-shell ionization independent of the source of excitation. Density functional theory (DFT) is applied to calculate wavefunctions of many-body molecular systems and interpret the measured emission spectra in terms of one-electron picture. At the end of this chapter the molecular orbital (MO) theory and symmetry classification of molecules are briefly introduced to explain calculated molecular wavefunctions in terms of linear combination of atomic orbitals (LCAO).

2.1 Kramers-Heisenberg Equations for X-Ray Emission Process

The total Hamiltonian of the interaction of electromagnetic field with electrons in a molecule can be separated into three parts, which can be independently discussed

$$H = H_{molecule} + H_{rad} + H_{int}. \tag{2.1}$$

The Hamiltonian of a free molecule consisting of N_e electrons and N_n nuclei is written as

$$\hat{H}_{molecule} = \sum_{i}^{N_e} \frac{p_i^2}{2m} - \sum_{i}^{N_e}\sum_{l}^{N_n} \frac{1}{4\pi\epsilon_0}\frac{Z_l e^2}{|\mathbf{r}-\mathbf{R}_l|} + \frac{1}{2}\sum_{j\neq i}^{N_e}\sum_{i}^{N_e} \frac{1}{4\pi\epsilon_0}\frac{e^2}{|\mathbf{r}_j-\mathbf{r}_i|} \tag{2.2}$$

and will be discussed in more detail in Section 2.2. H_{rad} is the Hamiltonian of the free radiation field. Electromagnetic waves are oscillations of the electromagnetic field, which allow to quantize them in a similar way as the harmonic oscillator. The electromagnetic vector potential, $\hat{\mathbf{A}}(\mathbf{r})$ can be written in the Schrödinger representation using the creation ($\hat{a}^\dagger_{\mathbf{k},\boldsymbol{\lambda}}$) and annihilation ($\hat{a}_{\mathbf{k},\boldsymbol{\lambda}}$) operators as,

$$\hat{\mathbf{A}}(\mathbf{r},t) = \sum_{k,\lambda} A_0(\hat{a}_{\mathbf{k},\lambda}\varepsilon_{\mathbf{k},\lambda}\mathsf{e}^{i\mathbf{kr}-i\omega_k t} + \hat{a}^\dagger_{\mathbf{k},\lambda}\varepsilon^*_{\mathbf{k},\lambda}\mathsf{e}^{-i\mathbf{kr}+i\omega_k t}) \tag{2.3}$$

where the abbreviation $A_0 = \sqrt{2\pi\hbar c^2/V_s\omega_k}$ with the system volume V_s, $\mathbf{k}$ is a quantum wave vector and $\boldsymbol{\epsilon}_\lambda$ represents two polarization vectors. The Hamiltonian of the free radial field is then

$$\hat{H}_{rad} = \sum_{\mathbf{k},\lambda} \hbar\omega_{\mathbf{k},\lambda}\left(\hat{a}^\dagger_{\mathbf{k},\lambda}\hat{a}_{\mathbf{k},\lambda} + \frac{1}{2}\right). \tag{2.4}$$

The interaction term H_{int} is obtained by replacing $\mathbf{p}_i$ in the $H_{molecule}$ with $\mathbf{p}_i - \frac{e}{c}\mathbf{A}(\mathbf{r},t)$. Applying the Coulomb gauge $\nabla\mathbf{A} = 0$, the two leading terms that contribute to the amplitude are [2]

$$\hat{H}^1_{int} = \frac{e}{m_e c}\sum_i \hat{\mathbf{p}}_i\hat{\mathbf{A}}(\mathbf{r_i}) \quad \& \quad \hat{H}^2_{int} = \frac{e^2}{2m_e c}\sum_i \hat{\mathbf{A}}^2(\mathbf{r_i}). \tag{2.5}$$

This interaction between the molecule (atom) and the electromagnetic field is treated as a small perturbation to the system which causes transition from the initial ground state of a system described with the wavefunction $|G\rangle = |g, \mathbf{k_{in}}, \epsilon_{\mathbf{in}}\rangle$ with corresponding energy $E_G = E_g + \hbar\omega_{in}$, into the final state described with the wavefunction $|F\rangle = |f, \mathbf{k_{out}}, \epsilon_{\mathbf{out}}\rangle$ with corresponding energy $E_F = E_f + \hbar\omega_{out}$. Here $|g\rangle$ and $|f\rangle$ correspond to the initial ground state and the final state of the molecule with corresponding energies E_g, E_f and $\mathbf{k_{in}}$, $\epsilon_{\mathbf{in}}$ and $\mathbf{k_{out}}$, $\epsilon_{\mathbf{out}}$ are wave vector and polarization of the incoming and outgoing photons, respectively. The transition rate for the scattering process can be written using the Fermi golden rule [58]

$$W_{f,g} = \frac{2\pi}{\hbar}\sum_f \left| \langle F|\hat{H}^2_{int}|G\rangle + \sum_i \frac{\langle F|\hat{H}^1_{int}|I\rangle\,\langle I|\hat{H}^1_{int}|G\rangle}{E_G - E_I} \right|^2 \times \delta(E_F - E_G). \tag{2.6}$$

where $|G\rangle$, $|F\rangle$, and $|I\rangle$ represent the ground (initial), final and intermediate state of the system, respectively. The delta function in the equation takes care of the energy conservation, so that the energy of the final state equals the energy of the ground state plus the energy of the x-ray photon. In general, the initial and final wavefunctions are composed of the molecular and photon term, but commonly the photon part of the wavefunction can be excluded from the discussion.

In Equation 2.6 the first oder contributions to the transition amplitude come from the H^2_{int}, which has the terms $\hat{a}^\dagger_{\mathbf{k},\lambda}\hat{a}_{\mathbf{k},\lambda}$ and $\hat{a}_{\mathbf{k},\lambda}\hat{a}^\dagger_{\mathbf{k},\lambda}$ and keeps the number of photons constant. The term $\hat{H}^1_{int}$ contributes only to the second-order transition amplitude. This leads to the Kramers-Heisenberg formul a [59], [60] and the total differential cross section can be expressed as

$$\begin{aligned}\frac{d^2\sigma}{d\Omega d(\hbar\omega_{out})} &= r_0^2\left(\frac{\omega_{out}}{\omega_{in}}\right)\sum_f \left| \langle f|\sum_j \mathsf{e}^{i\mathbf{q}\mathbf{r_j}}|g\rangle\,(\boldsymbol{\epsilon}_{in}\cdot\boldsymbol{\epsilon}^*_{out}) \right.\\ &+ \frac{1}{m_e}\sum_i\sum_{jj'}\left[\frac{\langle f|(\boldsymbol{\epsilon}^*_{out}\cdot\mathbf{p}_j)\mathsf{e}^{-i\mathbf{k}_{out}\mathbf{r}_j}|i\rangle\,\langle i|(\boldsymbol{\epsilon}_{in}\cdot\mathbf{p}'_j)\mathsf{e}^{i\mathbf{k}_{in}\mathbf{r}_{j'}}|g\rangle}{E_g - E_i + \hbar\omega_{in} - i\Gamma_i/2}\right.\\ &\left.\left.+ \frac{\langle f|(\boldsymbol{\epsilon}_{in}\cdot\mathbf{p}_j)\mathsf{e}^{i\mathbf{k}_{in}\mathbf{r}_j}|i\rangle\,\langle i|(\boldsymbol{\epsilon}^*_{out}\cdot\mathbf{p}_{j'})\mathsf{e}^{i\mathbf{k}_{out}\mathbf{r}_{j'}}|g\rangle}{E_g - E_i - \hbar\omega_{out}}\right]\right|^2 \delta(E_g - E_f + \hbar(\omega_{in} - \omega_{out}))\end{aligned} \tag{2.7}$$

The sum includes all electrons in the system (j, j') and the $r_0 = \mathsf{e}^2/m_e c^2$ is the classical electron radius. In Equation (2.7) we have taken into account the finite lifetime of the intermediate state and added in the denominator a complex expression of a Lorentz profile with the linewidth Γ_i. The first term arises from the $\mathbf{A}^2$ term in Equation (2.5) and far from any resonances this term is dominant. For historical reason this type of scattering is called Thompson scattering, and corresponding cross section can be written as

$$\frac{d^2\sigma}{d\Omega d(\hbar\omega_{out})} = r_0^2\frac{\omega_{out}}{\omega_{in}}|\boldsymbol{\epsilon}_{in}\cdot\boldsymbol{\epsilon}^*_{out}|^2\sum_f \left|\langle f|\sum_j \mathsf{e}^{i\mathbf{q}\mathbf{r_j}}|g\rangle\right|^2 \delta(E_g - E_f + \hbar(\omega_{in} - \omega_{out})). \tag{2.8}$$

The operator contains the momentum transfer $\mathbf{q} = \mathbf{k}_{in} - \mathbf{k}_{out}$ of the photon. If the momentum transfer is zero, the operator is equal to one and from the orthogonality of the wavefunctions $|g\rangle$ and $|f\rangle$ arises that the cross section is non-zero only when they are equal. If molecular (atomic) ground and final states have the same energy, then the law of energy conservation guarantees that energies of incoming and outgoing photons are also equal (elastic scattering). In case of inelastic scattering the incident photon transfers part of its momentum and energy to the system. Then the dynamic structure factor $S(\mathbf{q}, \omega_{in} - \omega_{out}) = \sum_f \left| \langle f | \sum_j \mathrm{e}^{i\mathbf{q}\mathbf{r}_\mathbf{j}} | g \rangle \right|^2 \delta(E_g - E_f + \hbar\omega_{in} - \hbar\omega_{out})$ provides information on the excitation caused by charge fluctuation [3].

The second term in Equation (2.7) starts to dominate when the incoming photon energy is close to the absorption edge, $E_g \approx E_i - \hbar\omega_{in}$. The essential part of Kramers-Heisenberg cross-section for resonant x-ray process can be in this case written as:

$$\frac{d^2\sigma}{d\Omega d(\hbar\omega_{out})} = \frac{r_0^2}{m_e^2}\left(\frac{\omega_{out}}{\omega_{in}}\right)\sum_f \left| \sum_i \frac{\langle f|\hat{T}_2|i\rangle \langle i|\hat{T}_1|g\rangle}{E_g - E_i + \hbar\omega_{in} - i\Gamma_i/2} \right|^2 \times \delta(E_g - E_f + \hbar\omega_{in} - \hbar\omega_{out}). \tag{2.9}$$

The transition operators are $\hat{T}_1 = (\boldsymbol{\epsilon}_{in} \cdot \mathbf{p}'_j)\mathrm{e}^{i\mathbf{k}_{in}\mathbf{r}_{j'}}$ and $\hat{T}_2 = (\boldsymbol{\epsilon}^*_{out} \cdot \mathbf{p}_j)\mathrm{e}^{-i\mathbf{k}_{out}\mathbf{r}_j}$ and in the long wavelength photon limit they are evaluated as

$$\hat{T} = (\boldsymbol{\epsilon} \cdot \mathbf{p})\mathrm{e}^{-i\mathbf{k}\mathbf{r}} \approx \boldsymbol{\epsilon} \cdot \mathbf{p} + i(\boldsymbol{\epsilon} \cdot \mathbf{p})(\mathbf{k} \cdot \mathbf{r}), \tag{2.10}$$

where the first term corresponds to electric dipole transition and the second term represents electric quadrupole transition. The quadrupole transition probability is smaller by 10^{-4} to the dipole probability for energies below 10 keV and can be neglected [2]. Equation (2.9) describes the second-order process, where the first process is the x-ray absorption from $|g\rangle$ to $|i\rangle$ and then emission from $|i\rangle$ to $|f\rangle$. If the final state $|f\rangle$ is the same as the initial state $|g\rangle$, then the process is the resonant elastic x-ray scattering (REXS) and when there is a difference between these two states we talk about resonant inelastic x-ray scattering (RIXS) [61].

Equation (2.9) is not limited to the description of the resonant process, but it can be applied to all photoexcitation processes. In the special case of the nonresonant process, when the energy of the incident photon is well above the x-ray absorption edge, the emission is no longer coherent with the absorption. Equation (2.9) can be rewritten so that the matrix elements are first squared and then summed over the intermediate states

$$\frac{d^2\sigma}{d\Omega d(\hbar\omega_{out})} = \frac{r_0^2}{m_e^2}\frac{\omega_{out}}{\omega_{in}}\sum_f \sum_i \frac{|\langle f|\hat{T}_2|i\rangle|^2 |\langle i|\hat{T}_1|g\rangle|^2}{(E_g - E_i + \hbar\omega_{in})^2 + \Gamma_i^2/4} \times \delta(E_g - E_f + \hbar\omega_{in} - \hbar\omega_{out}). \tag{2.11}$$

The equation shows that there is no strict distinction between the resonant and the nonresonant process. Therefore, non-resonant x-ray emission can be considered as the Kramers-Heisenberg x-ray scattering following excitation into the non-bound state. The changing of the shape of the emission lines for excitations to bound states, just above the Fermi level, is caused mainly by change of the distribution of the unoccupied state and not by a change of the scattering mechanism [3].

In order to connect the x-ray emission process with the molecular structure Equation 2.9 can be formulated in a slightly different way. In case of a non-resonant process the electron is excited to a high-energy continuum and can be treated separately from other electrons. The intermediate and final states can be written as

$$\begin{aligned} |i\rangle &= |\phi_\epsilon\rangle |i'\rangle, \quad & E_i &= E_{i'} + E_\epsilon \\ |f\rangle &= |\phi_\epsilon\rangle |f'\rangle, \quad & E_f &= E_{f'} + E_\epsilon \end{aligned} \tag{2.12}$$

where $|\phi_\epsilon\rangle$ is a photoelectron state with energy E_ϵ. When we insert this in Equation 2.9 we obtain

$$\frac{d^2\sigma}{d\Omega d(\hbar\omega_{out})} = \frac{r_0^2}{m_e^2}\left(\frac{\omega_{out}}{\omega_{in}}\right)\sum_f \int dE_\epsilon \rho(E_\epsilon) t^2 \left|\sum_i \frac{\langle f'|\hat{T}_2|i'\rangle \langle i'|\hat{T}_1|g\rangle}{E_g - E_{i'} - E_\epsilon + \hbar\omega_{in} - i\Gamma_{i'}/2}\right|^2 \times \delta(E_g - E_{f'} - E_\epsilon + \hbar\omega_{in} - \hbar\omega_{out}). \quad (2.13)$$

The t is the dipole transition amplitude from a core state to the photoelectron state and $\rho(E_\epsilon)$ is the density of photoelectron states, which can be approximated with a constant. Most importantly, after integration over energy E_ϵ, the spectral shape of non-resonant emission process does not depend on the incoming photon energy, $\hbar\omega_{in}$, and Equation 2.13 can be formulated as

$$\frac{d^2\sigma}{d\Omega d(\hbar\omega_{out})} = \frac{r_0^2}{m_e^2}\left(\frac{\omega_{out}}{\omega_{in}}\right)\rho t^2 \sum_i^{occ.} \frac{|\langle f'|T|i'\rangle|^2}{(\hbar\omega_{out} - E_{i'} + E_{f'})^2 + \Gamma_{i'}^2/4} \quad (2.14)$$

where the $\langle f'|T|i'\rangle$ is one-electron transition matrix element of the x-ray emission process.

The relaxation process of a molecule (atom) is therefore independent of the excitation of a core electron to high-energy continuum. This can be generalized also for other types of core-hole ionization and different ionization techniques can be used for excitation yielding the same x-ray emission spectrum. The shape of the x-ray emission spectrum can be finally written as

$$F(E_{emission}) \propto \sum_i^{occ.} \frac{|\langle\phi_f|T|\phi_i\rangle|^2}{(E_{emission} - E_i + E_f)^2 + \Gamma_i^2/4} \quad (2.15)$$

where $\phi_{i,f}$ are wavefunctions of the molecular system in the initial ionized core-hole and the final state with corresponding energies E_i and E_f, and $E_{emission}$ is the energy of the emitted x-ray. In our study Equation 2.15 represents a starting point. At this point we did not discuss how to describe the wavefunction of the molecular system, which is the most difficult part in the calculation and this will be presented in the following chapter.

2.2 Many-Body Systems

The electronic state of the molecule can be in principle obtained by solving the Schrödinger equation. The most common simplification in the calculation is a well-known Born-Oppenheimer approximation [62], [63]. The idea of the approximation is to separate the nuclei motion from the electron because the nuclei are several thousands of times heavier than the electrons and consequently the response time of the electron to any change in the position of the nuclei is considered to be immediate. Also, we assume that the nuclei are in fixed arrangement and that the potential is invariant to time.

In our study of the electronic structure of third elements Equation 2.14 is a starting point. The process of excitation of electron in high-energy continuum is independent of the relaxation process of a molecule (atom). Therefore, different techniques can be used for excitation and x-ray emission spectra will provide the same information. This leads to time-independent Schrödinger equation for the electronic part

$$\hat{H}_{molecule}\Psi(\mathbf{r}_1, \cdots, \mathbf{r}_{N_e}; \mathbf{R}) = E(\mathbf{R})\Psi(\mathbf{r}_1, \cdots, \mathbf{r}_{N_e}; \mathbf{R}) \quad (2.16)$$

where $\Psi(\mathbf{r}_1, \cdots, \mathbf{r}_{N_e}; \mathbf{R})$ is the electronic wavefunction, which is associated with each of the electron coordinates $\{\mathbf{r}_i\}$ and parametrically on $3N_n$ nuclei coordinates $\mathbf{R}$. Also, the total energy $E(\mathbf{R})$ is a function of the nuclear coordinates. Using Hartree atomic units,

the electronic part of the Hamiltonian for the system of N_e electrons and N_n nuclei can be written as

$$\hat{H} = -\frac{1}{2}\sum_{i}^{N_e}\nabla_i^2 - \sum_{i}^{N_e}\sum_{l}^{N_n}\frac{Z_l}{|\mathbf{r}-\mathbf{R}_l|} + \frac{1}{2}\sum_{j\neq i}^{N_e}\sum_{i}^{N_e}\frac{1}{|\mathbf{r}_j-\mathbf{r}_i|} \tag{2.17}$$

where the first part corresponds to the kinetic energy of the electrons $\hat{T}$, second to the "external" nuclear potential $\hat{V}_{en}$ and the last part to the electron-electron interaction, $\hat{V}_{ee}$. The electron-electron interaction term represents the most complicated part in terms of calculations and the quality of the particular method depends in many cases on the quality of the approximation of electron-electron interaction. Different classes of method were developed to calculate electronic states of many-body Hamiltonian. The wavefunction-based and density-based methods are two most important representatives. The wavefunction-based methods calculate observables using the wavefunction (or spinors), and they can be subdivided into perturbational and variational approaches. The wavefunction depends on the coordinates (spatial+spin) of all particles, meaning that its complexity depends on the number of particles. Consequently, for large many-body systems the wavefunction becomes very complex and it is difficult to treat it computationally. The Moller-Plesset and Hartree-Fock are the most known examples of perturbational and variational methods, respectively [64].

For density-based methods the electron density is a "fundamental" variable which completely characterizes the system and the electron density depends only on three space variables independent of the number of particles and can be handled more easily. In this thesis density functional theory (DFT) was used to simulate the electronic structure. The electron density $\rho(\mathbf{r})$ is the probability of measuring one of the particles at coordinates $\mathbf{r}_1 \cdots \mathbf{r}_{N_e}$ at the point $\mathbf{r}$

$$\rho(\mathbf{r}) = N_e \int |\Psi(\mathbf{r}, \mathbf{r}_2 \cdots \mathbf{r}_{N_e})|^2 d\mathbf{r}_2 \cdots d\mathbf{r}_{N_e}. \tag{2.18}$$

If the wavefunction is normalized, integrating the electron density over all space yields the total number of electrons

$$N_e = \int \rho(\mathbf{r}) d\mathbf{r} \tag{2.19}$$

The electron density can be considered as the special case of a single-particle (reduced) density matrix, which is a more general quantity. The single-particle density matrix is defined as

$$\gamma_1(\mathbf{r}_1; \mathbf{r}_1') = N_e \int \Psi(\mathbf{r}_1, \mathbf{r}_2 \cdots \mathbf{r}_{N_e})\Psi^*(\mathbf{r}'_1, \mathbf{r}_2 \cdots \mathbf{r}_{N_e}) d\mathbf{r}_2 \cdots d\mathbf{r}_{N_e}. \tag{2.20}$$

The matrix density can be interpreted like N_e times the probability density to measure the coordinate $\mathbf{r}_i$ at $\mathbf{r}_1$ and in this case is equal to electron density, $\rho(\mathbf{r}_1) = \gamma_1(\mathbf{r}_1; \mathbf{r}_1)$ [65], [66].

Analog to the single-particle case, the two-particle (reduced) density matrix is defined as

$$\gamma_2(\mathbf{r}_1\mathbf{r}_2; \mathbf{r}_1'\mathbf{r}_2') = \frac{N_e(N_e-1)}{2!} \int \Psi(\mathbf{r}_1, \mathbf{r}_2 \cdots \mathbf{r}_{N_e})\Psi^*(\mathbf{r}_1', \mathbf{r}_2' \cdots \mathbf{r}_{N_e}) d\mathbf{r}_3 \cdots d\mathbf{r}_{N_e}. \tag{2.21}$$

The diagonal of the two-particle density gives the two-particle density $\rho'(\mathbf{r}_1, \mathbf{r}_2) = 2\gamma_2(\mathbf{r}_1\mathbf{r}_2; \mathbf{r}_1\mathbf{r}_2)$ where $\rho'(\mathbf{r}_1, \mathbf{r}_2)$ may be interpreted as the probability to find one particle at $\mathbf{r}_1$ and another at $\mathbf{r}_2$. The higher order (reduced) density matrix can be defined in a similar way.

We can write the Schrödinger Equation (2.16) and find the ground state energy of the electron system in terms of density. The nuclear-electron interaction part is the easiest to write in term of density, since the operator does not contain any derivatives. The expected value can be written in terms of one-particle density

$$\langle \Psi | \hat{V}_{en} | \Psi \rangle = -\sum_{l}^{N_n} \int \rho(\mathbf{r}) \frac{Z_l}{|\mathbf{r} - \mathbf{R}_l|} d\mathbf{r}. \tag{2.22}$$

The other two terms in Equation (2.16) are more difficult to write using the electron density. The electron-electron interaction part can be written only in terms of two-particle density

$$\langle \Psi | \hat{V}_{ee} | \Psi \rangle = \frac{1}{2} \iint \frac{\rho'(\mathbf{r}, \mathbf{r}')}{|\mathbf{r} - \mathbf{r}'|} d\mathbf{r} d\mathbf{r}'. \tag{2.23}$$

The kinetic operator contains derivative and it is impossible to write the wavefunction and its conjugate in the form of a single square. The kinetic energy is therefore written using a single-order density matrix

$$\langle \Psi | \hat{T} | \Psi \rangle = -\frac{1}{2} \int \nabla^2 \gamma_1(\mathbf{r}_1; \mathbf{r}_1') d\mathbf{r}. \tag{2.24}$$

2.2.1 Thomas-Fermi theory

One of the first ideas to use electron density like fundamental variable was provided independently by Thomas [67] and Fermi [68] in 1927. They knew that for homogeneous noninteracting fermion gas the average kinetic energy per particle can be expressed with the particle density, $\epsilon_{kin} = C_F \rho^{2/3}$ where $C_F = \frac{3}{10}(3\pi^2)^{2/3}$ is a constant. They used this to calculate the total kinetic energy

$$T = \int d\mathbf{r} \rho(\mathbf{r}) \epsilon_{kin}(\mathbf{r}). \tag{2.25}$$

In order to calculate the electron-electron energy term, they used a classical model with one-particle electron density so the Thomas-Fermi functional[1] for the total energy of many-body system is

$$E_{TF}[\rho(\mathbf{r})] = C_F \int \rho^{5/3}(\mathbf{r}) d\mathbf{r} - \sum_{l}^{N_n} \int \rho(\mathbf{r}) \frac{Z_l}{|\mathbf{r} - \mathbf{R}_l|} d\mathbf{r} + \frac{1}{2} \iint \frac{\rho(\mathbf{r}_1)\rho(\mathbf{r}_2)}{|\mathbf{r}_1 - \mathbf{r}_2|} d\mathbf{r}_1 d\mathbf{r}_2. \tag{2.26}$$

At that time exchange and correlation functionals were not known so they were not included in the equation producing limited results. However, the Thomas-Fermi equation was the first equation which has shown that the energy of a many-body system can be given in terms of the electron density [64]–[66].

2.3 Density Functional Theory

As the beginning of the density functional theory (DFT), the paper of Hohenberg and Kohn [69] from 1964 is commonly taken. In this paper Hohenberg and Kohn provided the proof for two theorems.

[1] In order to present the meaning of the *functional* we will use example, "Suppose a particle moves in the xy plane from point A to point B with velocity $v(x, y)$. Then the time the particle takes to move from A to B is a functional of the velocity." Atkins and Friedman [62], page 316.

- It states that: "*The external potential $v_{ext}(\mathbf{r})$ is determined, within a trivial additive constant, by the electron density $\rho(\mathbf{r})$*". The theorem has been proven by *reductio ab absurdum*, they showed that there cannot be two different external potentials ($v_{ext}(\mathbf{r})$) yielding the same ground state. If the electron density uniquely determines external potential, which has a unique wavefunction, then all electronic properties of the system are uniquely determined by the electron density.

- In order to complete the theory they formulated a variational principle in terms of the electron density. The universal density functional delivering the energy $E[\rho(\mathbf{r})]$ of the system will yield a global minimum only when the correct ground state input electron density is used.

These two theorems allow to write the ground state energy of the system as a functional of the ground state electron density

$$E[\rho_0(\mathbf{r})] = F[\rho_0(\mathbf{r})] + \int v_{ext}(\mathbf{r})\rho_0(\mathbf{r}) < F[\rho'(\mathbf{r})] + \int v_{ext}(\mathbf{r})\rho'(\mathbf{r}) \tag{2.27}$$

where kinetic and electron-electron interaction functionals are put together $F[\rho] = T[\rho] + V_{ee}[\rho]$, because they are treated in the same way. The Hohenberg and Kohn theory provides the existence of ground state functional, but the explicit form of kinetic and electron-electron functional is not known.

One year later, in 1965, Kohn and Sham [70] turned DFT into a practical calculation tool. In order to write the kinetic functional, Kohn and Sham introduced a system of n non-interacting electrons and expressed the electron density in terms of Slater determinant of orthonormal one-electron orbitals

$$\begin{aligned} \rho(\mathbf{r}) &= \sum_{i}^{N_e} n_i |\phi_i^{KS}(\mathbf{r})|^2 \\ \Psi_0(\mathbf{r}_1 \cdots \mathbf{r}_{Ne}) &= \frac{1}{\sqrt{N!}} det||\phi_i^{KS}(\mathbf{r_k})|| \end{aligned} \tag{2.28}$$

where n_i is the occupation number of the orbital ϕ_i^{KS} and Ψ_0 is a ground state wavefunction of the electron density. Introducing the orbitals allows us to compute kinetic energy with good accuracy. The kinetic energy can be approximated by

$$T_s = -\frac{1}{2}\sum_{i}^{N_e} \int \phi_i^{KS*}(\mathbf{r}_1)\nabla^2\phi_i^{KS}(\mathbf{r}_1)dr_1. \tag{2.29}$$

Difference between the ground state kinetic energy T and the computed T_s was put in exchange-correlation energy. Also, the one-electron orbitals are used to compute the electron-electron interaction term in a classical way

$$J(\rho) = \frac{1}{2}\iint \frac{\rho(\mathbf{r}_1)\rho(\mathbf{r}_2)}{|\mathbf{r}_1 - \mathbf{r}_2|} d\mathbf{r}_1 d\mathbf{r}_2 \tag{2.30}$$

and the difference which originated from the exchange part in true V_{ee} interaction is again put in the exchange-correlation energy. Collecting all equations, the Hohenberg-Kohn functional (2.27) can be expressed as

$$\begin{aligned} F[\rho] &= T_s[\rho] + J[\rho] + E_{xc}[\rho] \\ E_{xc}[\rho] &\equiv T[\rho] - T_s[\rho] + V_{ee}[\rho] - J[\rho] \end{aligned} \tag{2.31}$$

where $E_{xc}[\rho]$ is the exchange-correlation functional. Many authors like to separate these two terms, then the exchange term is the difference between $V_{ee}[\rho]$ and $J[\rho]$ which originates from Coulomb repulsion between electrons. On the other hand, the reason for the difference between $T[\rho]$ and $T_s[\rho]$ is in Pauli repulsion. However, the ground state energy is found by writing the electron density in terms of Kohn-Sham orbitals and applying the variational principle to minimize the energy. The final results are one-electron Kohn-Sham equations

$$\begin{aligned} -\frac{1}{2}\nabla^2\phi_i^{KS}(\mathbf{r}) + v_{eff}\phi_i^{KS}(\mathbf{r}_1) &= \epsilon_i\phi_i^{KS}(\mathbf{r}_1), \\ v_{eff} &= \int \frac{\rho(\mathbf{r}')}{|\mathbf{r}-\mathbf{r}'|}d\mathbf{r}' + v_{ext}(\mathbf{r}) + v_{xc}(\mathbf{r}), \end{aligned} \tag{2.32}$$

where v_{xc} is given as a derivative of E_{xc} with respect to ρ,

$$v_{xc} = \frac{\delta E_{xc}}{\delta \rho}. \tag{2.33}$$

In order to solve the equation, the self-consistent approach is used. The initial set of orbitals is used to compute the electron density from which all energies (T_s, J, E_{ext}, E_{xc}) are obtained and new Kohn-Sham orbitals constructed. The procedure is repeated until the self-consistency is achieved.

2.3.1 Approximation of exchange-correlation functional

Local Density Approximation It is important to note that if the exchange-correlation term is known exactly, the DFT is an exact theory without any approximation. In practice, except in very simple cases, it is impossible to treat the exchange-correlation part exactly, therefore an approximation is needed. The oldest and the simplest model to treat the E_{xc} is the *local density approximation* (LDA). The basis of the LDA for the exchange and correlation energy functional is the model of uniform electron gas [70]. The model can be applied on the system with slowly varying density and then E_{xc} functional depends on the local electron density of the investigated system

$$E_{xc}^{LDA} = \int e_{xc}^{unif}(\rho(\mathbf{r}))\rho(\mathbf{r})d\mathbf{r} \tag{2.34}$$

where e_{xc}^{unif} is the exchange-correlation energy per particle of uniform electron gas. The exchange and correlation part can be separately discussed. The exchange part is well known for electron gas, but the correlation part is already a difficult many-body problem [71], [72]. Introducing Quantum Monte Carlo (QMC) calculation for the electron gas by Ceperley and Alder [73], the quality of the correlation approximation part was significantly improved and different parametrizations of this data are used today.

In the molecule the condition of slowly varying electron density is not completely satisfied, but it has been found that LDA gives useful results. The reason for these unexpectedly good results are two systematic error cancellations. The LDA underestimates E_c, but overestimates E_x resulting in very good E_{xc} values.

General Gradient Approximation To improve the accuracy of calculation in the real systems which have inhomogeneous electron density a few approaches which include non-local information were developed. One way to do this is the so-called *gradient-expansion approximation* (GEA), which includes the gradients of density $|\nabla\rho(\mathbf{r})|$, $|\nabla\rho(\mathbf{r})|^2$, $\nabla^2\rho(\mathbf{r}), \ldots$.

A better way is to define a more general function of $\rho(\mathbf{r})$ and $\nabla\rho(\mathbf{r})$. Such type of approximation is called *general-gradient approximation* (GGA) and can be written as

$$E_{xc}^{GGA}[\rho] = \int d\mathbf{r} f(\rho(\mathbf{r}), \nabla\rho(\mathbf{r})). \tag{2.35}$$

There are different ways in the construction of $f(\rho(\mathbf{r}), \nabla\rho(\mathbf{r}))$ function, which makes a difference between GGA construction compared to LDA, which varies only in parametrization. The exchange and correlation part are also separated like in LDA and can be combined from different authors in order to find the best approach for a particular investigated system [71].

2.3.2 Kohn-Sham orbitals

Strictly speaking, the Kohn-Sham orbitals do not have a direct physical significance since they are primarily used to calculate the electron density, which determines physical observables of the system. However, it is very common to interpret Kohn-Sham orbitals within molecular orbital schemes [74]–[76], which provide a very good description of the molecular electronic structure. The molecular orbital representation of the KS orbitals obtained from the DFT calculations will be used throughout this thesis to discuss the x-ray emission spectra.

The molecular orbitals cannot be expressed in an analytical form. The problem is solved by expanding the orbital in a well known basis set. Practically, for molecular orbitals a *linear combination of atomic orbitals* (LCAO) (for more details see Section 2.4) is used

$$\phi_i^{KS} = \sum_\alpha c_{\alpha i}\chi_\alpha \tag{2.36}$$

where the $c_{\alpha i}$ are the MO expansion coefficients and χ_α are the atomic basis functions. When the basis set is complete, the expanded function is exactly described, but this requires the infinite basis set which is impossible to calculate. On the other hand, the smaller basis set reduces the quality of the representation. So the compromise must be found between the length and accuracy of the calculation [77], [78].

The atomic orbitals can be separated to a radial component $R_{n,l}(r)$ and a spherical component $Y_{l,n}(\theta,\phi)$. The radial part contains the polynominals which are too complex for the calculation and commonly two types of functions are used in approximation of atomic orbitals: *Slater Type Orbitals* (STO) and *Gaussian Type Orbitals* (GTO). The STO have the power of r instead of polynominals

$$STO = NY_{l,n}(\theta,\phi)r^{n-1}\mathsf{e}^{-\zeta r} \tag{2.37}$$

where N is the normalization factor and parameter ζ is determined by fitting the real atomic function. The STO are sometimes difficult to compute, so the GTO are more commonly used

$$GTO = NY_{l,n}(\theta,\phi)r^{l}\mathsf{e}^{-\zeta r^2}. \tag{2.38}$$

The GTO functions are a worse approximation of the atomic orbitals than STO. The r^2 dependence in the exponential of GTO results in zero slope at the nucleus and falls off too rapidly far from the nucleus. In order to improve the description of atomic orbitals, a linear combination of several GTO functions can be used. Generally, more calculation time is needed to compute one STO than to evaluate a few GTO orbitals. In Figure 2.1 a comparison between STO and GTO modelled by a linear combination of three GTO functions is presented for the hydrogen atom $1s$ orbital. The Gaussian type orbitals are poorly described at the nucleus and several Gaussian functions are used to describe the exponential tail.

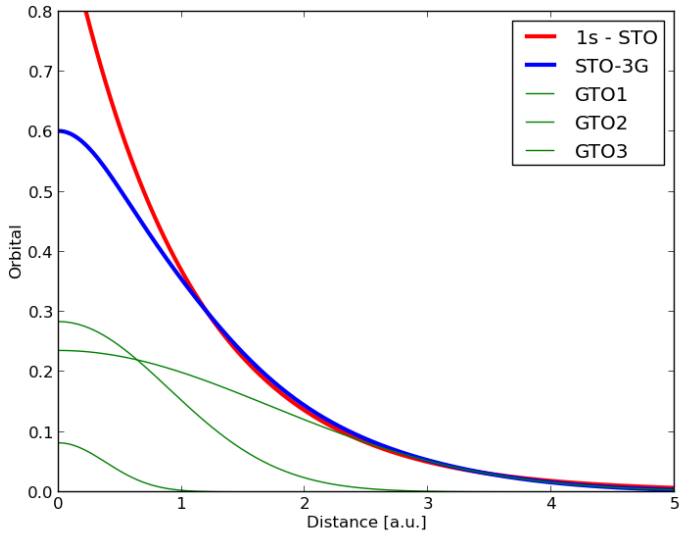


Figure 2.1: Comparison of the hydrogen 1s Slater type wavefunction ($\zeta = 1.0$) and corresponding STO-3G.

2.3.3 StoBe-deMon program package

The $K\alpha$ and $K\beta$ x-ray emission spectra of low-Z elements in the present work were calculated by the StoBe-deMon [79] program package based on the density functional theory (DFT). In these calculations, the geometry optimization of the molecule is performed first yielding energy minimum of the system. The obtained positions of atoms are fixed and used as the input parameter in the calculation of x-ray emission spectra. In the calculations of the first coordinate sphere around P, S and Cl atoms the full symmetry was employed in order to label molecular orbitals according to the irreducible representations of the corresponding symmetry group. The calculations of the full molecule were performed without employing any symmetry. The x-ray spectra were calculated in the ground state approximation in which both the initial $1s^{-1}$ core hole state and the final $2p^{-1}$ or the valence hole state were represented by Kohn-Sham orbitals of the ground state [80], [81]. In this approximation the dipole transition moments were calculated as explicit one-electron transitions. In order to improve the accuracy of calculated absolute emission energies, individual optimization of initial and final state was performed and the corresponding emission energies were calculated as differences in the orbital energies of initial and final states. The convergence of calculation was not achieved for optimization of an individual state for all systems. So, for few systems only ground state calculation was employed. In the final comparison with the experiment an overall shift of the calculated absolute emission energy scale was applied to coincide with the experiment. The difference in the energy scale originates in relativistic effects and approximations for exchange-correlation functional. In case of the ground state calculation the energy shift was around 70 eV and after the optimization of each separate state the correction of energy scale was reduced below |5| eV.

Atoms building the molecular system calculated in this work are presented in Table 2.1 with corresponding orbital and auxiliary basis sets. The K, L and M in the nomenclature *(n1s,...,nKs/ n1p,...,nLp/ n1d,...,nMd)* indicate the number of s, p and d orbitals, respectively, and each orbital is constructed with a different number of Gaussian type orbitals. For P, S and Cl atoms the same triplet-zeta valence polarized (TZVP) (73111/6111/1)[82]

Table 2.1: The orbital and auxiliary basis set for elements building the molecules studied in this thesis.

	basis sets	
elements	orbital	auxiliary
P	(73111/6111/1)	(5,4;5,4)
S	(73111/6111/1)	(5,4;5,4)
Cl	(73111/6111/1)	(5,4;5,4)
O	(6311/311/1)	(5,2;5,2)
H	(3111/111)	(4,2;4,2)
Li	(621/1/1)	(4,3;2,3)
Na	(6321/411/1)	(5,4;5,4)
K	(63321/5211/1)	(5,5;5,5)
Fe	(63321/531/311)	(5,5;5,5)
Zn	(63321/531/311)	(5,5;5,5)

orbital basis set was used, but the coefficients N and ζ are different for each atom. This basis set contains five s, four p and one d orbitals, where the first s orbital was described by seven GTOs orbitals, the second s orbital with three GTOs and so on. In the StoBe-deMon calculations we also need to itemize two auxiliary Gaussian basis sets. The first represents the Coulomb potential and the second represents the exchange-correlation potential over the numerical grid. With this procedure, a coarser grid can be used to speed up the iterations [83], [84]. The nomenclature *(N_C(c),N_C(v); N_{XC}(c), N_{XC}(v))* indicates the number of c (core region) and v (valence region) Gaussian functions which were used to fit and expand the Coulomb (C) and exchange-correlation (XC) potentials, respectively.

In all the calculations the GGA exchange functional by Becke, Be88 [85], and the GGA correlation functional by Perdew, PD91 [86] were employed. The same basis set and the same exchange-correlation functional were used in all calculations to allow direct comparison of the calculated data.

It is also important to note that for some compounds the convergence was not achieved since the effects of the environment were of a longer range than the first two coordination spheres and a balance neutral model could not be achieved. Sometimes difficulties can appear also in geometry optimization if the system is stopped in a local minimum instead of a global one.

2.3.4 Population analysis

The calculated electron density is commonly discussed in terms of partial charges of atoms in the molecule. In order to interpret the electron density in terms of atomic charges different approaches were developed. The concept of atomic charge is very useful, but the problem is that partial atomic charges in a molecule are not physically observable in quantum mechanics. Therefore, the unique proper scheme to determine partial charges does not exist and the results obtained from different methods cannot be compared. In order to analyze the electron density, three approaches can be taken:

- Partitioning the wavefunction in terms of the basis function,
- Fitting schemes,
- Partitioning the electron density into atomic domains.

Table 2.2: Differences between the results of Mulliken (**M**) and Loewdin (**L**) population analysis for the phosphorus $5a_1$ orbital within the PO_4^{3-} ion using different phosphorus basis sets.

	STO-3G		6321/521/1		73111/6111/1		ii_iglo		iii_iglo		DZ-ANO	
AO	M	L	M	L	M	L	M	L	M	L	M	L
P $3s$	31	19	27	21	26	20	26	19	27	19	27	23
O $2s$	28	28	26	27	26	27	26	27	25	26	26	24
O $2p$	41	52	47	52	47	53	48	53	48	54	47	53

Details about this topic can be found in Ref. [63]. In this thesis the Mulliken population analysis [87]–[90] is applied to all investigated molecules. The Mulliken analysis belongs to the group of methods which are partitioning the wavefunction. The starting point in this type of analysis is the electron density in Equation (2.19), which is expressed as the square of the one electron molecular orbitals (MO)

$$N_e = \sum_{i}^{N_{orbitals}} n_i \langle \phi_i | \phi_i \rangle = \sum_{i}^{N_{orbitals}} \sum_{\alpha\beta}^{M_{basis}} c_{\alpha i} c_{\beta i} \langle \chi_\alpha | \chi_\beta \rangle = \sum_{\alpha\beta}^{M_{basis}} D_{\alpha\beta} S_{\alpha\beta}, \tag{2.39}$$

where the sum of the product of MO coefficients and occupation numbers is the density matrix $D_{\alpha\beta} = \sum_i^{N_{orbitals}} n_i c_{\alpha i} c_{\beta i}$. The number of electrons in the atomic orbital α is the product of the type $D_{\alpha\alpha} S_{\alpha\alpha}$. For the off-diagonal elements $D_{\alpha\beta} S_{\alpha\beta}$ the number is equally shared between atomic orbitals α and β. The number of electrons associated with the atom A in Mulliken population analysis is defined as

$$\rho_A = \sum_{\alpha \in A}^{M_{basis}} \sum_{\beta}^{M_{basis}} D_{\alpha\beta} \langle \chi_\alpha | \chi_\beta \rangle \tag{2.40}$$

and the total charge on the atom A is the sum of nuclear and Mulliken's charge

$$Q_A = Z_A - \rho_A. \tag{2.41}$$

Normalized and non-orthogonal atomic basis sets are used in Mulliken scheme, which can lead to nonphysical results. For example, the diagonal elements may be larger than two, which is forbidden by the Pauli principle. Off-diagonal elements may become negative, which is not physically possible. To solve the orthogonality problem, different schemes were developed, for example Löwdin population analysis [91] or natural population analysis (NPA) [92]. In the orthogonal basis all off-diagonal elements are by default zero and the diagonal elements are restricted to values between zero and two. In Table 2.2 the Mulliken and Löwdin population analysis of one ($5a_1$) MO of the PO_4^{3-} ions are presented. During the calculation the parameters were kept the same, only different phosphorus atom basis sets were used. Generally, the influence of the basis set on the results of population analysis can be significant, but in our case of phosphate ion it was found almost negligible.

2.4 Molecular Orbital Theory

The molecular orbital (MO) theory is commonly used to describe the electronic structure of molecules. The idea of MO theory is that the electronic structure in a molecule can be expressed in terms of molecular orbitals which have well defined energies. Each MO is formed as the linear combination of atomic orbitals (LCAO) from all atoms in the

molecule. With increasing nuclear distances the interaction between atoms diminishes and the orbitals become atomic justifying the usage of atomic orbitals as the basis set. The MO theory is integrated in StoBe-deMon package employing the expression of the atomic orbital basis set (see Section 2.3.2). This led to the interpretation of the calculation and then also measured emission spectra in terms of MO theory. The theory will be introduced on the simplest model of the diatomic molecules such as H_2 and O_2. The concept and terminology from diatomic molecules can be then applied to the electronic structure of larger molecules.

2.4.1 Diatomic molecule

The s-type orbitals in a diatomic molecule can form two types of σ wavefunctions

$$\begin{aligned} \sigma &= N(c_a\psi(1s_a) + c_b\psi(1s_b)) \\ \sigma^* &= N(c_a\psi(1s_a) - c_b\psi(1s_b)) \end{aligned} \tag{2.42}$$

where the $\psi(1s_a)$ and $\psi(1s_b)$ are an atomic $1s$ wavefunction on the atom A and B, respectively. The coefficients c_a and c_b determine the magnitude of the contribution of A and B atomic orbitals relative to each other and factor N normalizes the wavefunction. Looking at the structure of σ and σ^* wavefunction presented in Figure 2.2 we can see that for σ wavefunction the electron density is increased in space between the nuclei. All those wavefunctions with increased electron density between the nuclei are called bonding MO. In case of σ^*, electron density is concentrated on the nuclei. This type of wavefunctions where a nodal plane perpendicular to the molecular axis exists between the nuclei is called antibonding MO and they are labeled with *. Compared to the energy of individual $1s$ orbital, the energy of bonding and antibonding orbitals is decreased and increased, respectively. The label σ is used for MO which do not have the nodal plane on the molecular axis, they are symmetrical to rotation around the molecular axis. If the MO have 1 or 2 nodal planes on the molecular axis, they are labeled as π and δ, respectively [93].

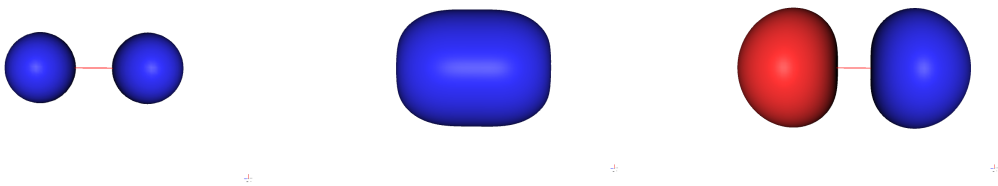


Figure 2.2: (*left*) Two $1s$ atomic orbitals forming: (*center*) σ bonding orbitals and (*right*) σ^* antibonding orbitals. The blue and red colors represent the positive and negative values of the orbital.

In case of H_2 molecule the two equal atomic orbitals $\psi(1s)$ form the bonding $\sigma = \frac{1}{\sqrt{2}}(\psi(1s_a) + \psi(1s_b))$ and antibonding $\sigma^* = \frac{1}{\sqrt{2}}(\psi(1s_a) - \psi(1s_b))$ MO. The two electrons occupy the bonding MO with an opposite spin state, according to the Pauli principle. Because the energy of the bonding orbital is lower than individual $1s$ atomic orbital, the energy of the system is reduced and the molecule is stable. Antibonding orbital with higher energy is occupied in a H_2^- molecule, with two electrons in bonding MO and one in the antibonding MO resulting in increased total energy of the system compared to H_2 molecule. However, the increase of energy due to the occupancy of the antibonding MO is compensated by the two electrons occupying the bonding MO and the system is still stable. The same picture can be used also to explain why a He_2 molecule cannot be formed. In

this case the energy increases because two electrons in the antibonding MO are too large and the system is not stable.

In case of the H_2^+ molecule the energy position of MO can be presented more exactly, calculating $E = \langle\Psi|H|\Psi\rangle$. Equation (2.42) with two identical atomic orbitals ϕ_A and ϕ_B, one on atom A and the other on atom B, respectively, but with the same energy $\varepsilon_A = \varepsilon_B$ can be used to describe the wavefunction. The secular determinant is then 2×2 matrix with Coulomb integral written as $\langle\phi_A|H|\phi_A\rangle = H_{AA} = H_{BB} = \varepsilon_A$ and resonance integral $\langle\phi_A|H|\phi_B\rangle = H_{AB} = H_{BA}$. For the overlap integrals we can write $\langle\phi_A|\phi_A\rangle = \langle\phi_B|\phi_B\rangle = 1$ and $\langle\phi_A|\phi_B\rangle = \langle\phi_B|\phi_A\rangle = S$. The final result for the real coefficients of the normalized wavefunction is

$$\begin{aligned} c_A = c_B \quad c_A &= \frac{1}{(2+2S)^{1/2}} \quad \text{for} \quad E_+ = \frac{\varepsilon + H_{AB}}{1+S} \\ c_A = -c_B \quad c_A &= \frac{1}{(2-2S)^{1/2}} \quad \text{for} \quad E_- = \frac{\varepsilon - H_{AB}}{1-S}. \end{aligned} \tag{2.43}$$

H_{AB} and ε are both negative, so the lower energy E_+ is associated with σ wavefunction, as already explained previously. The overlap integral can vary between 0 and 1 moving both energies up. This is the reason why the system is not completely symmetrical and the decrease of energy of bonding MO selective to the energy of atomic orbital is smaller than the increased energy of antibonding MO.

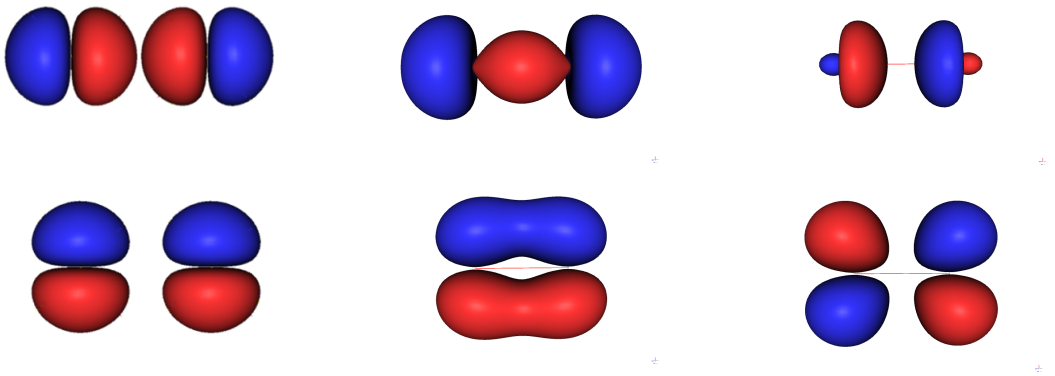


Figure 2.3: (*left-up*) Two p atomic orbitals forming: (*center-up*) σ bonding and (*right-up*) σ^* antibonding molecular orbitals. (*left-bottom*) Two p atomic orbitals forming: (*center-bottom*) π bonding and (*right-bottom*) π^* antibonding molecular orbitals. The blue and red colors represent different signs of orbital.

In the description of the electronic structure of the diatomic molecules from second-row elements we need to include p atomic orbitals. The p atomic orbitals have wavefunctions with separate regions of the opposite sign. If the region of two p orbitals with the same sign overlaps, the electron probability in this space increases. In case of the overlapping region with the opposite sign, the electron probability decreases. The orientation in space of p atomic orbitals results in two types of MO, σ and π. When p orbitals are oriented along the molecular axis with the same sign of the wavefunction between nuclei, then the σ type orbital is formed. The σ^* is formed when the sign of the wavefunction between the nuclei is opposite and the electron probability between the nuclei is decreased. In this case the nodal plane between nuclei exists, as it can be seen in the top part of Figure 2.3. If the p orbitals are oriented perpendicular to the molecular axis, they form a π type of MO.

The π orbital with an equal sign in the direction along the molecular axis is bonding and with the opposite sign it is antibonding, as shown at the bottom part of Figure 2.3.

The interaction between two atomic orbitals forming the MO is stronger if their orbital energies are similar. When atomic orbitals are too diffuse or compact, their participation in MO will be negligible. These effects can be seen in the molecular diagram of the O_2, presented in Figure 2.4. The $1s$ orbitals have the same energy but they are localized around nuclei and their interaction is non-significant. This type of the orbitals where the energy and shape are atomic-like are called core-orbitals. The valence orbitals are formed from O $2s$ and $2p$ atomic orbitals. In the first approximation, the energy of $2s$ and $2p$ are far from each other and they do not interact. The result is the formation of 2σ and $2\sigma^*$ from $2s$ and the separate formation of 3σ, 1π, $1\pi^*$ and $3\sigma^*$ MO from $2p$ oxygen atomic orbitals. Generally, the molecular diagram is more complex, as we need to include different phenomena, for example electronegativity, nonbonding orbitals and orbital mixing. These effects change the orbital features and energy order in the molecular diagram [77], [93].

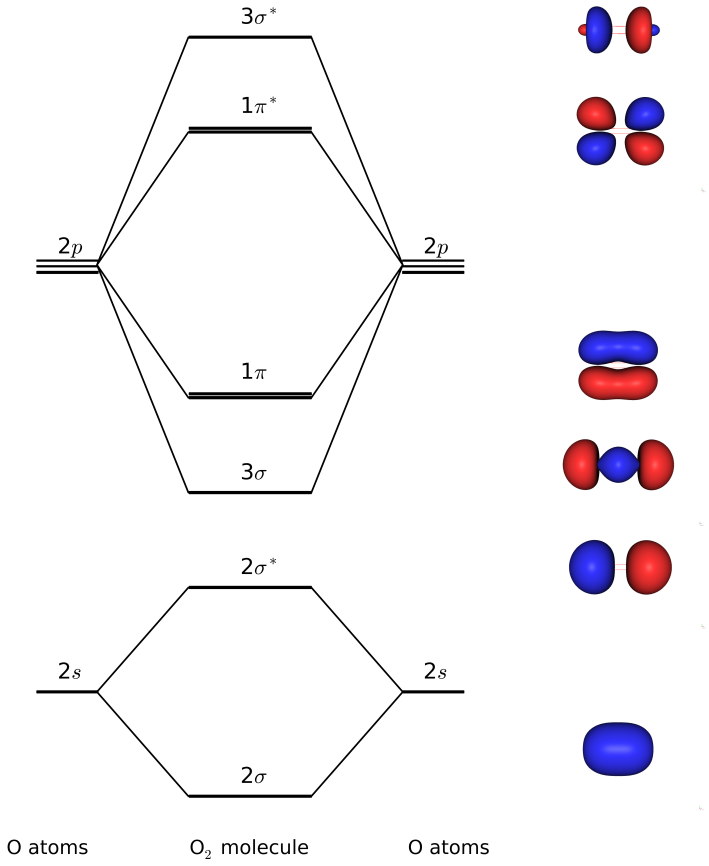


Figure 2.4: The molecular diagram of the O_2 molecule with the corresponding valence MO.

2.5 Symmetry Classification of Molecules

In complex molecules MO are commonly classified according to the symmetry of the molecule. Symmetry operation is an action that does not change the molecular features after it has been executed. Each symmetry operation has a symmetry element according to which the symmetry operation is carried out. In molecules we can have five different types of symmetry operation:

- The identity operation, E, does not do anything and the corresponding symmetry element is the molecule itself.
- The n-fold axis rotation, C_n, rotation of the molecule by $2\pi/n$ around an axis. The element of symmetry is the axis of rotation and the molecule can have more than one C_n type rotation axes.
- The reflection, σ, reflects the molecule according to the mirror plane.
- The operation i is the inversion through the center of symmetry.
- An n-fold improper rotation, S_n, is a composite operation consisting first of rotation through an angle $2\pi/n$ followed by a reflection in a plane perpendicular to the axis.

Table 2.3: The character table of the T_d point group.

T_d	E	$8C_3$	$3C_2$	$6S_4$	$6\sigma_d$
A_1	1	1	1	1	1
A_2	1	1	1	-1	-1
E	2	-1	2	0	0
T_1	3	0	-1	1	-1
T_2	3	0	-1	-1	1

Table 2.4: The character table of the C_{3v} point group.

C_{3v}	E	$2C_3$	$6\sigma_d$
A_1	1	1	1
A_2	1	1	-1
E	2	-1	0

Table 2.5: The character table of the C_{2v} point group.

C_{2v}	E	C_2	$\sigma_v(xz)$	$\sigma_v(yz)$
A_1	1	1	1	1
A_2	1	1	-1	-1
B_1	1	-1	1	-1
B_2	1	-1	-1	1

More than one symmetry operation can be applied to a given molecule, depending on the combination of symmetry operations molecules are classified in point groups. To form the point group at least one point in space should exists which is unchanged in all symmetry operations in a group. All important properties of the point group can be summarized in the character table. In this thesis we will discuss molecules with T_d, C_{3v}, and C_{2v} symmetry whose character tables are presented in Tables 2.3, 2.4, and 2.5,

respectively. The first row in the character table represents the symmetry operations of the point group. If the symmetry operations are related to each other, they are grouped in the same class. For example, a molecule with T_d symmetry has eight independent C_3 rotations, three independent C_2 rotations, six independent improper rotations S_4 and six independent reflections through dihedral plane σ_d. The columns of numbers are orthogonal to one another. In the first column the labels of irreducible representation are listed. The labels A and B are used for one-dimensional representations. If the dimension of irreducible representation is two or three, the labels E and T are used, respectively. Consequently, the E and T irreducible representations have two and three degenerated states, respectively. Each row of numbers is a representation and indicates the effect of the corresponding symmetry operation on the molecular orbital. The character 1 means that after symmetry operations the molecular wavefunction is unchanged, where the -1 reverses the sign of wavefunction.

One of the most important applications of the molecular symmetry is to determine the possibility for chemical bonding. It can be shown that only atomic orbitals with the same symmetry can form the molecular orbitals. This leads us to the formulation of the general stepwise process for the construction of molecular orbitals.

1. Put the molecule in the coordinate system, assign x, y, and z coordinates to the atoms.

2. Determine the point group of the molecule.

3. For each type of atoms use separately $s, p, d \ldots$ valence orbitals to form representations and then reduce the representation to the corresponding irreducible representation.

4. Identify the atomic and molecular fragment orbitals within the irreducible representations.

5. Join the orbitals with the same symmetry and similar energy to form molecular orbitals.

The molecular orbitals are then labeled according to the irreducible representation to which they belong.

Chapter 3

Experimental Part

As already explained in the introduction, XES is an inner shell x-ray spectroscopic technique and different types of ionizing radiation can be used to induce x-ray fluorescence from the sample. At the Microanalytical center (MIC) of the J. Stefan Institute (JSI) a proton beam accelerated to the MeV energy range by an electrostatic accelerator is used and this proton-induced x-ray emission (PIXE) is regularly applied to analyze elemental content of samples from a broad range of disciplines. The basic properties of the PIXE technique and the PIXE experimental set-up available at MIC are presented in the first part of this chapter. In addition to the proton-induced measurements performed at JSI, the whole set of phosphorus XES spectra was also recorded using monochromatic synchrotron radiation for target excitation to experimentally verify that XES spectra do not depend on the excitation mode. For that purposes our high energy resolution x-ray emission spectrometer was installed at the ID26 beamline of the European Synchrotron Radiation Facility (ESRF) in Grenoble. A very brief description of the ESRF synchrotron and the ID26 beamline is therefore also presented. The most important part in the full experimental set-up is the high energy resolution x-ray emission spectrometer, which is mandatory to perform XES spectroscopy, regardless of the excitation mode. The general physical principle exploited in Bragg crystal spectrometers used to perform high energy resolution x-ray emission spectroscopy is introduced and different types of spectrometers are presented. Finally, the main characteristics of the JSI tender x-ray emission spectrometer used in our experiment are described, followed by a detailed report of the specific experimental conditions during our XES measurements.

3.1 The PIXE Technique

High sensitivity reaching detection limits below 1 ppm, a nondestructive approach, the possibility to focus the proton beam down to micrometer size or to perform in-air analysis are only some of the features which contribute to the large range of applications of the PIXE method in biology, archeology, ecology, and art. The PIXE method is commonly used to determine elemental composition of the sample by analyzing the x-ray emission spectra induced by MeV proton beam. The intensity of emitted characteristic lines is described by the x-ray production cross section. The x-ray cross section for the strongest diagram line ($K\alpha$) is given by

$$\sigma_K^X = \frac{\sigma_K \omega_K}{1 + K_\beta / K_\alpha} \tag{3.1}$$

where $K\beta/K\alpha$ is the intensity ratio of the strongest diagram line. Two physical quantities are defining the intensity of emitted characteristic lines, the ionization cross section (σ_K) and the fluorescence yield (ω_K). The ionization cross section, σ_i, gives the probability for

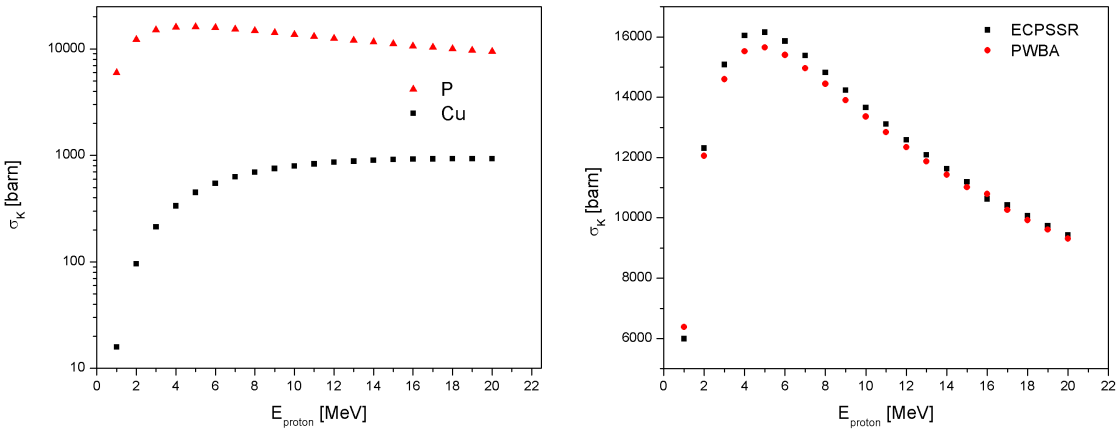


Figure 3.1: *(left)* The K-shell ionization cross section σ_K for P and Cu atoms as a function of proton energy. *(right)* Comparison of P σ_K ionization cross section calculated with the PWBA and ECPSSR model.

inner shell ionization in a collision of the atom with a MeV proton. In case of the PIXE technique we are exploring the radiative decay of the atom with inner shell vacancy, and the probability for radiation decay is given by the fluorescence yield, ω_i.

The basic ionization mechanism in a proton-atom collision is driven by Coulomb's interaction between the projectile and the inner shell electrons. In case of the proton-induced ionization $Z_{projectile} \ll Z_{atom}$, where $Z_{projectile}$ and Z_{atom} refer to the nuclear charges of the projectile and the target atom, respectively, the inner shell ionization can be theoretically treated within the first-order perturbation theory. The projectile far from the atom, before and after the collision, is approximately a free particle and can be described by the plane wave. This is a well known plane wave Born approximation (PWBA), which qualitatively reproduces the experimentally observed behavior of the cross section. However, for better quantitative agreement with the experimental data, PWBA framework was modified to account for the deflection of the projectile in the Coulomb field of the nucleus (C), perturbation of the atomic states by the projectile (PSS), relativistic effects (R), and projectile energy loss (E) into the ECPSSR theory [94]. Correction of the PWBA model with ECPSSR is presented in Figure 3.1 for the case of phosphorus K-shell. ECPSSR cross sections are in very good agreement with experimental data and they can be used effectively in PIXE analysis to extract elemental concentrations from the measured x-ray yields. ECPSSR σ_K ionization cross sections of P and Cu calculated with the ERCS08 [95] program are also presented in Figure 3.1. In general, the maximum of the cross section σ_i for ionizing an i-shell of the atom is achieved when the projectile velocity matches the velocity of the electron in the i-shell. At a given proton energy the σ_K ionization cross section reduces with increasing atomic number of target element.

The second important term in Equation 3.1 describing the x-ray production cross section is the fluorescence yield ω_i. An atom with the K shell vacancy can be relaxed by a radiative or non-radiative Auger transition. Both transitions contribute to the natural level width Γ, which is given as a sum of partial widths for the radiative and Auger decay

$$\Gamma = \Gamma_{rad} + \Gamma_{Aug}. \tag{3.2}$$

Γ is related to the lifetime of the inner shell vacancy τ according to the uncertainty principle

Table 3.1: Coefficients for Bambynek semi-empirical formula used to calculate the fluorescence yield [8].

	K-shell	L-shell
B_0	$(3.70 \pm 0.52) \times 10^{-2}$	0.17765
B_1	$(3.112 \pm 0.044) \times 10^{-2}$	2.98937×10^{-3}
B_2	$(5.44 \pm 0.11) \times 10^{-5}$	8.91297×10^{-5}
B_3	$-(1.25 \pm 0.07) \times 10^{-6}$	-2.67184×10^{-7}

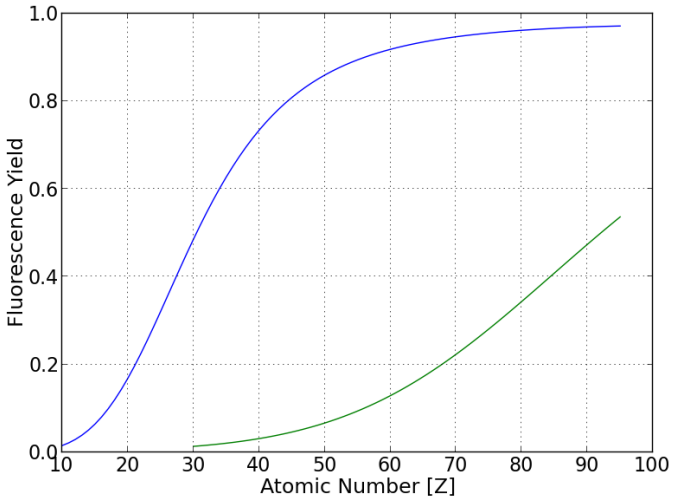


Figure 3.2: Blue and green lines depict K- and L-shell fluorescence yields, respectively, as a function of atomic number Z.

$\Gamma\tau = \hbar$. The fluorescence yield given in Equation (3.1) gives the probability for radiative transition and is defined as

$$\omega = \frac{\Gamma_{rad}}{\Gamma}. \tag{3.3}$$

The ratio of Auger and radiative transition depends on the atomic number Z. Bambynek, Crasemann, Fink, *et al.* [96] formulated a semi-empirical formula for the calculation of the fluorescence yield

$$\left(\frac{\omega_j}{1-\omega_j}\right)^{1/4} = \sum_{i=0}^{3} B_i Z^i \tag{3.4}$$

where B_i are the coefficients whose values are tabulated (see Table 3.1) and ω_i is the fluorescence yield for K or L-shells. In Figure 3.2 showing the fluorescence yield for K and L shell, we can see that for third-row elements the fluorescence yield is below 20% and in most cases the inner shell vacancy is filled by an Auger transition. This relatively low probability for fluorescence decay is compensated by a relatively high cross section for K-shell ionization of third-row elements.

3.1.1 PIXE experimental set-up at JSI

At the Microanalytical Center of the J. Stefan Institute in Ljubljana the PIXE technique is being routinely used to analyze multi-elemental composition of the studied samples. Several dedicated end stations have been constructed during the years, where different



Figure 3.3: Photo of the laboratory with the accelerator and beamline end stations at the MIC of the JSI.



Figure 3.4: Photo of the vacuum chamber of the high energy resolution x-ray emission spectrometer at MIC.

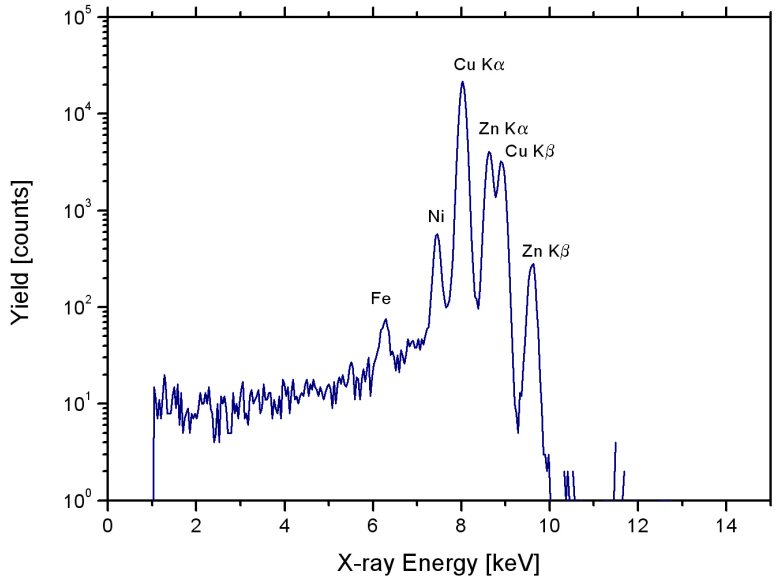


Figure 3.5: PIXE spectrum of 1 Slovenian tolar (1 SIT) coin induced with 2 MeV protons.

types of PIXE analysis can be performed. Besides conventional broad beam PIXE analysis used to determine average bulk concentrations, proton microbeam can be used to record 2D distributions of elements within the studied sample with micron lateral resolution. Large archeological objects, which cannot be inserted in the vacuum chamber, can be studied in air using the external proton beam. Finally, the high resolution x-ray emission measurements can be used to address also the chemical state of the elements in the sample. A photo of the laboratory is presented in Figure 3.3 and the vacuum chamber of the high energy resolution emission spectrometer connected to one of the beamlines is shown in Figure 3.4.

Common to all endstations is the preparation of the accelerated proton beam, which is provided by the electrostatic ion accelerator. JSI is equipped with 2MV Tandetron accelerator produced by High Voltage Engineering Europa. It is possible to produce and accelerate different ion beams by using three different types of the ion source: duoplasmatron, sputter, and multicusp. In order to prepare a bright and high current proton beam we typically use multicusp source [97]. The multicusp source is used to prepare negatively charged ions H^-, which are accelerated to the Tandetron tank by the extraction voltage of 30 keV. Both ends of the Tandetron accelerator are at ground potential. Negative ions from multicusp are first accelerated by the positive terminal voltage, thus gaining the first half of their final energy. In the middle of the accelerator the negative ions pass through the nitrogen gas (stripper channel), where they lose electrons and become positively charged ions (protons). A positive voltage is used to further accelerate the protons until they reach the final energy.

After going through the accelerator tank, the MeV beam is shaped and focused by the triplet electrostatic quadruple lenses. The switching magnet has a double function: to analyze protons according to their energy and charge, and mainly to direct the beam into different beamlines hosting dedicated experiments. Each beamline is optimized for a specific type of experiments. In the PIXE experiment, a typical proton current on the target in the range of nA up to a few tens of nA. The working pressure in the vacuum

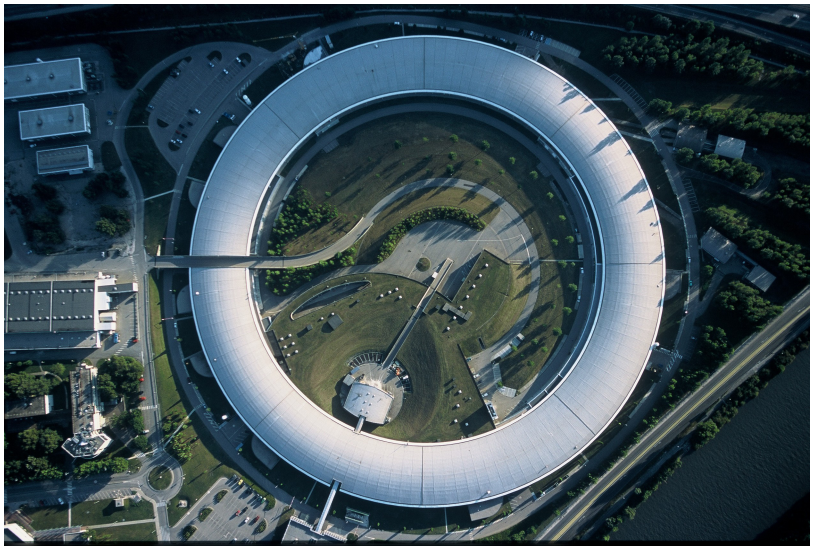


Figure 3.6: Photo of the European Synchrotron Radiation Facility in Grenoble.

chambers hosting endstations is in the order of 10^{-6} mbar and is usually achieved using turbomolecular pumps. A typical PIXE spectrum measured at MIC is shown in Figure 3.5 as an example.

3.2 ESRF ID26 Beamline Description

Synchrotron radiation is emitted when charge particles with velocity near the speed of light move along a circular trajectory. This phenomenon is exploited in the synchrotron facilities representing a high brilliant x-ray source. The European Synchrotron Radiation Facility (ESRF, Figure 3.6) in Grenoble is one of the largest third-generation synchrotron light sources. Electrons are produced with an electron gun and initially accelerated to 200 MeV in the linear accelerator (Linac). The Linac also group electrons into bunches, which are injected into the booster synchrotron. The booster synchrotron is a pre-accelerator with a circumference of 300 m where the electrons reach the energy of 6 GeV. Finally, the bunches of electrons are injected into the storage ring with the circumference of 844 m. The booster synchrotron is used to refill the storage ring two times a day. The 992 simultaneously circulating electron bunches result in a maximum current of 200 mA. Different types of magnets are positioned along the storage ring: focusing, bending and undulator magnets. The magnets are installed on 32 straight and 32 curved sections which alternate around the ring. In the curved sections bending magnets force the electron path into circular direction and in the straight section focusing magnets are used to correct the electron path so that they remain close to their ideal orbit. The x-rays are emitted from bending magnets where the electrons are deflected. In order to produce more focused and brilliant x-rays, undulator magnets are used. Undulator magnets are made of an array of small magnets, which force the electrons to follow an undulating trajectory. The x-ray energy spectrum emitted from undulator magnets is concentrated at a certain energy which is called the harmonic.

At a ID26 beamline three undulators are used to snake electrons and produce x-rays. In order to define the x-ray direction a set of vertical and horizontal slits are used, so-called primary slits. After slits the beam is deflected away from the storage ring bremsstahlung emission cone by horizontally deflected mirror (HDM1). The monochromatic beam is pro-

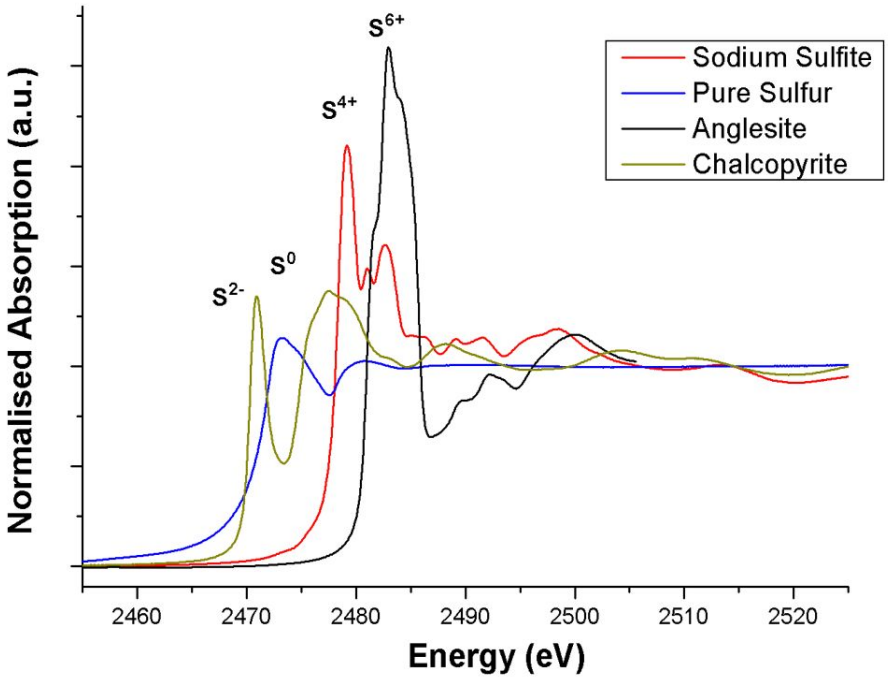


Figure 3.7: The examples of the few sulfur x-ray absorption spectra.

vided by a cryogenically double crystal cooled monochromator with two sets of Si crystals cut in (311) or in (111) crystal plane. The resolution of the monochromator is 0.36 eV at S K-edge (2472 eV) using the Si(111) crystal. Finally, the x-ray beam is focused down to $250 \times 50\mu$m using two mirrors in the Kirkpatrick-Baez configuration [98]. The typical photon flux is around $5{\times}10^{12}$ photon/sec at 2.5 keV using the fundamental undulator radiation. Higher harmonics are suppressed by two Si mirrors at grazing conditions ($\sim$ 5 mrad).

The full spectral range of the ID26 beamline is 2.4-30 keV. The chlorine K absorption edge at 2.822 keV and particularly the sulfur K absorption edge at 2.472 keV are situated practically at the low energy limit of the beamline, while the phosphorus absorption edge at 2.145 keV is already below. In fact it is very common for the beamlines equipped with the Si(111) crystal monochromators that sulfur is the lightest element that can be studied using conventional XAS spectroscopy. On the other hand, very few beamlines are available at synchrotron where phosphorus K absorption edge can be reached with satisfactory experimental conditions. While XAS measurements using tunable synchrotron radiation can therefore be fully exploited to perform a chemical state analysis of sulfur or chlorine as presented in Figure 3.7, an alternative approach is required to analyze also phosphorus. XES spectroscopy can be used as a complementary technique not only in smaller laboratories using laboratory excitation sources but also at synchrotron since the energy of the incoming photon beam only needs to be above the corresponding K shell ionization threshold. As shown later, a 3 keV photon beam was used in our study to record XES spectra and analyze the chemical state of phosphorus at the beamline, which is otherwise not accessible for phosphorus electronic structure studies using common XAS spectroscopy.

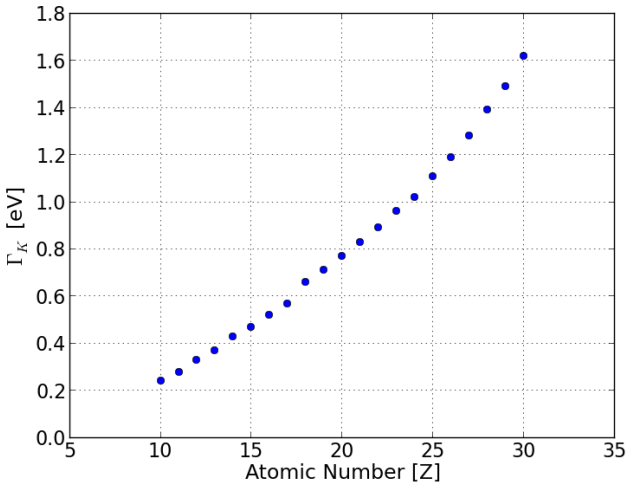


Figure 3.8: Linewidths of the atomic K levels [99].

3.3 Wavelength Dispersive X-Ray Spectroscopy

The mandatory condition to perform XES spectroscopy is the high energy resolution of the spectrometer used to analyze x-rays emitted from the sample. As seen from Equation 2.15 the linewidth of the XES spectrum is ultimately limited by the natural linewidth Γ_i defined by the lifetime of the core hole. In order to resolve the fine structure of the XES spectrum the energy resolution should be on the level of the natural core-hole lifetime broadening. In case of K shell ionized atoms the corresponding Γ_K natural linewidths are presented in Figure 3.8 as a function of the atomic number. The values for third-row elements studied in this work are around 0.5 eV. At the moment no solid state energy dispersive detector can provide such resolution and the wavelength dispersive X-ray (WDX) spectroscopy employing crystal spectrometer is used to perform XES spectroscopy.

In case of WDX spectrometer the dispersion of x-rays according to their wavelength is achieved using Bragg reflection on a crystal analyzer according to the Bragg law, see Figure 3.9. In 1913, W. H. Bragg and W. L. Bragg [100] formulated the condition for x-ray reflection as

$$n\lambda = 2d\sin\theta \tag{3.5}$$

where λ is the wavelength of x-ray, θ is the angle between the incident x-rays and the normal of the scattering planes of the crystal, and n is an integer number giving the order of reflection. The crystal is modelled as a set of the discrete parallel planes by a constant distance $d = a/\sqrt{h^2+k^2+l^2}$, where a is the lattice parameter and h, k, l are the Miller indexes. When the phase difference of x-rays between two planes is constructive, we will get a diffraction peak for a particular angle.

This Bragg reflection rule can be used to measure the intensity distribution of an x-ray spectrum as shown in Figure 3.10 presenting schematically the working principle of the simplest flat single crystal spectrometer. The slit is used to define the angle of the incoming x-ray beam. Diffracted photons can be detected by a position sensitive detector or using an additional slit before the detector to define the angle of detection. If the incident angle is varied, which normally involves rotating the crystal through a controllable angle and the detector by twice this angle amount, the detector will receive radiation over a range of wavelengths and a spectrum will be obtained. The energy resolution of the spectrometer

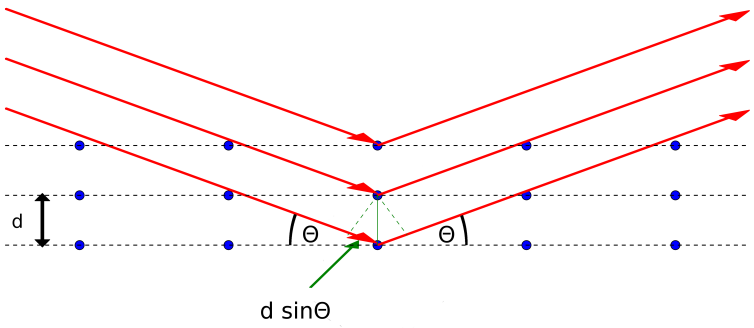


Figure 3.9: Reflection of x-ray on the crystal planes according to the Bragg law.

can be estimated using the derivative of the Bragg equation (3.5)

$$\frac{\Delta\lambda}{\lambda} = \frac{\Delta E}{E} = \frac{1}{\tan\Theta}\Delta\Theta. \tag{3.6}$$

The resolution of the spectrometer therefore depends on the collimation provided by the slit. The ultimate limit to the resolution is imposed by the intrinsic resolution of the crystal itself, which should preserve the inherently good angular collimation of the reflected photons. For this reason, perfect crystals which are essentially free from any defects are used. However, the response function even for a perfect crystal is not a Dirac delta function. The theory which describes diffraction on the perfect crystal is known as a dynamic theory of diffraction, mostly developed by C. G. Darwin [101] and the Darwin reflectivity curve for a perfect crystal is calculated in the following chapter.

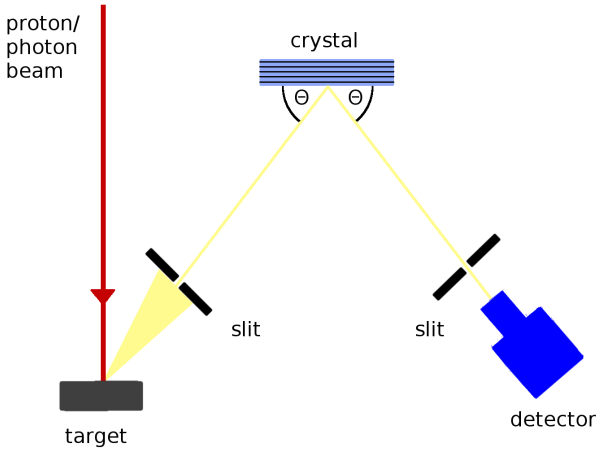


Figure 3.10: The basic working principle of the Bragg crystal spectrometer.

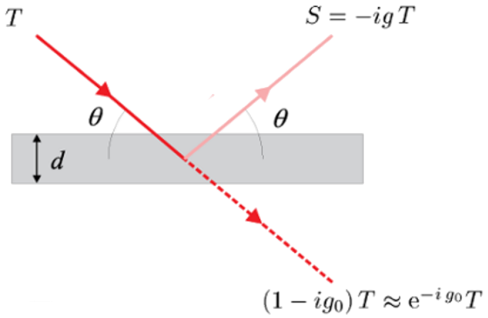


Figure 3.11: Reflection and transmission of the incident beam on a single atomic layer [102].

3.3.1 Dynamic theory of diffraction

In a dynamic theory of diffraction, the crystal is treated as an infinite stack of atomic planes. From each atomic plane a small fraction of incident wave is reflected into exit wave and partly transmitted to the next layer. This is shown schematically in Figure 3.11 presenting the reflection and transmission of the incident wave, T, from a single layer of the crystal near the Bragg case. The thickness of the layer is $d \ll \lambda$, with a density of electrons ρ. The amplitude of the reflected wave is given by [102]

$$g = \frac{\lambda r_0 \rho d}{\sin\Theta} = \frac{2d^2 r_0}{nV}|F| \tag{3.7}$$

and the phase of the reflected wave is shifted by $-\pi/2$ (by a factor of $-i$) with respect to the incident wave yielding finally

$$S = -igT. \tag{3.8}$$

In Equation 3.7 r_0 is the classical electron radius and the electron density ρ was replaced by $|F|/V$ where F is the structure factor of the unit cell and V is its volume. This will allow us later to apply this expression also to the scattering from a layer of unit cells. The transmitted wave is written as

$$T = (1 - ig_0)T \approx \mathrm{e}^{-ig_0}T \tag{3.9}$$

Here

$$g_0 = \frac{|F_0|}{|F|}g \tag{3.10}$$

where we have introduced F_0, the unit cell structure factor in the forward direction ($\Theta = 0$).

These equations can be now applied to the crystal with an infinite number of layers, each of which is labeled by the index j, starting from the surface as shown in Figure 3.12. From Bragg's law, it is known that the reflected wave from the layer $j+1$ will be in phase with the one from layer j if the pathlength differs by an integer number of wavelengths. As we are interested in deriving the small bandwidth of the reflected region, then the phase change is restricted to small deviations around $n\pi$ and it is given by

$$\phi = n\pi + \Delta \tag{3.11}$$

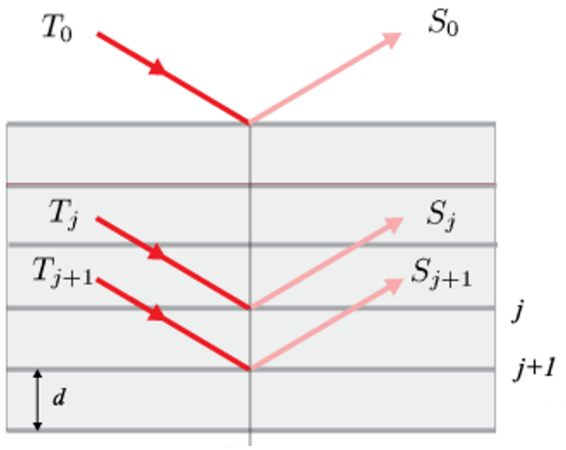


Figure 3.12: Symmetric Bragg diffraction from an infinite set of atomic planes [102].

where Δ is a small parameter and will be used as the independent variable. The small relative deviation in the phase must be equal to corresponding relative deviation in scattering vector ζ, so it can be written as $\Delta = n\pi\zeta$. The incident and reflected waves just above layer j will be denoted as T_j and S_j, respectively. The total reflected wave from jth layer is obtained from the reflection of the wave T_j and we must also add the part reflected from the $j+1$th layer. The wave S_{j+1} changes its phase during transmission through the jth layer, so we will have

$$S_j = -igT_j + (1 - ig_0)S_{(j+1)}\mathrm{e}^{i\phi}. \tag{3.12}$$

In a similar way we can consider the wave just below the jth layer. The transmitted wave is composed of the wave $S_{j+1}\mathrm{e}^{i\phi}$ after it has been re-scattered from the bottom of the jth layer and from the wave T_j after it has been transmitted through the jth layer.

$$T_{j+1}\mathrm{e}^{-i\phi} = (1 - ig_0)T_j - igS_{j+1}\mathrm{e}^{i\phi}. \tag{3.13}$$

Suitable trial solutions for Equations 3.12 and 3.13 can be written as

$$T_{j+1} = \mathrm{e}^{-\eta}\mathrm{e}^{in\pi}T_j \quad \& \quad S_{j+1} = \mathrm{e}^{-\eta}\mathrm{e}^{in\pi}S_j. \tag{3.14}$$

The wave is attenuated only slightly from one layer to the next one, so the real part of η must be positive and small. This leads to the following expression for η

$$\eta^2 = g^2 - (\Delta - g_0)^2 \quad \Rightarrow \quad i\eta = \pm\sqrt{(\Delta - g_0)^2 - g^2}. \tag{3.15}$$

In order to calculate amplitude reflectivity S_0/T_0 we first use Equation 3.14 to write $S_1 = \mathrm{e}^{-\eta}\mathrm{e}^{in\pi}S_0$ which is then inserted into Equation 3.12 to get

$$S_0 = -igT_0 + (1 - ig_0)\mathrm{e}^{-\eta}\mathrm{e}^{in\pi}\mathrm{e}^{im\pi}\mathrm{e}^{i\Delta}. \tag{3.16}$$

Rearranging this equation and considering that η and Δ are $\ll 1$ we reach finally

$$r = \frac{S_0}{T_0} = \frac{-ig}{1 - (1 - ig_0)(1 - \eta)(1 + i\Delta)} = \frac{g}{i\eta + \Delta - g_0}. \tag{3.17}$$

The final Darwin reflectivity curve describing the intensity reflectivity is usually given as

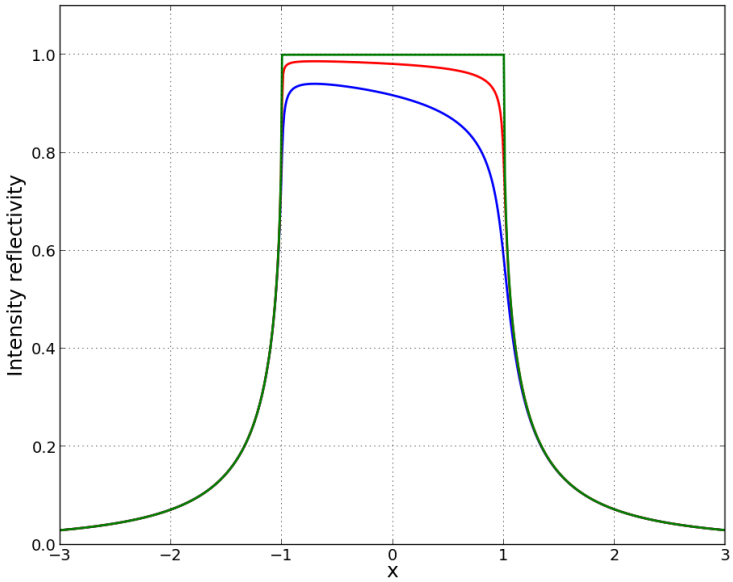


Figure 3.13: The Darwin reflectivity curve calculated without *(green)* and with absorption effects *(blue and red)*.

a function of the variable x

$$x = \frac{(\Delta - g_0)}{g} \tag{3.18}$$

and is written

$$R(x) = \left(\frac{S_0}{T_0}\right)\left(\frac{S_0}{T_0}\right)^* = \begin{cases} (x - \sqrt{x^2-1})^2 & \text{for } x \geq 1, \\ 1 & \text{for } |x| \leq 1, \\ (x + \sqrt{x^2-1})^2 & \text{for } x \leq -1. \end{cases} \tag{3.19}$$

The Darwin reflectivity curve calculated from Equation 3.19 is presented in Figure 3.13. For values $|x| < 1$ the reflectivity is 100% and this is the region of total reflection.

The most important parameter for us is the width of the Darwin reflectivity curve, which determines the quality of the crystal intrinsic resolution. The region of the total reflection in variable x has the width of 2. In order to convert this in terms of resolution we can replace the small phase shift Δ in Equation 3.18 by a change of the scattering vector $\Delta = n\pi\zeta$ and write

$$\zeta = \frac{gx + g_0}{n\pi}. \tag{3.20}$$

The change of the scattering vector ζ is equivalent to the wavenumber and energy bandwidth $\zeta = \Delta k/k = \Delta\lambda/\lambda = \Delta E/E$ and the final total reflection width is given by

$$\zeta_{width} = \frac{2g}{n\pi} = \frac{4d^2}{\pi n^2}\frac{r_0|F|}{V}. \tag{3.21}$$

The width of the Darwin reflectivity curve represents intrinsic limitation of the energy resolution and it is typically in the order of 10^{-4} for photon energies around 12.5 keV [102]. As an example Darwin widths are given in Table 3.2 for commonly used crystal analyzers in x-ray spectroscopy, silicon and germanium.

Table 3.2: The calculated Darwin widths of silicon and germanium crystals for different crystal cuts [102].

	$\zeta_{width} \times 10^{-4}$		
	(111)	(220)	(400)
Silicon	1.398	0.611	0.263
Germanium	3.472	1.60	0.688

So far the absorption effects have not been included in the discussion of the Darwin reflectivity curve. These effects can be included through the imaginary part of g_0 which is proportional to the absorption cross-section. The formula for the reflectivity is practically the same, only the variable x is now a complex number. The absorption effects are manifested in reducing the intensity reflectivity. This is presented in Figure 3.13, on the example of the Si(111) reflection. The red and blue line represent intensity reflection for waves with $\lambda = 0.70926$Å and $\lambda = 1.5405$Å, respectively. The asymmetric behavior of the Darwin curve is the consequence of different phases of the x-ray and atom position. In the region near $x \approx 1$ the x-ray wave is in phase with the position of the atomic planes and in case when $x \approx -1$ they are out of phase.

3.3.2 Different types of WDX spectrometers

As already shown previously, the K shell core hole broadening is in case of third-row elements studied here $\sim$ 0.5 eV. The emission energies of characteristic lines are in 2-3 keV energy range so the absolute angular resolution $\Delta\Theta$ defining the energy resolution $\Delta E/E$ should be $\sim 2 \times 10^{-4}$. Besides the intrinsic resolution of the crystal the main contribution to the final experimental resolution is the angular collimation, which is in case of the simplest flat crystal spectrometer (Figure 3.10) defined by the slit width and the target-crystal-detector distance. Assuming that a target-crystal-detector distance is 1 m, the slit width of 0.2 mm should be used, resulting in very small efficiency, which is the main disadvantage of WDX spectrometers.

In order to enlarge the solid angle of the spectrometer, a curved crystal in different focusing geometries can be used. In this case, a much bigger crystal surface is involved in the diffraction process. We will restrict our discussion to the spectrometers employing cylindrically curved crystals, which are most relevant for in-vacuum tender x-ray spectrometers. In von Hamos geometry [103] presented schematically in Figure 3.14, the crystal curvature is perpendicular to the dispersion plane and vertical focusing is applied. Different wavelengths from the sample diffract along vertical stripes of the crystal and are focused into separated spots on the position sensitive detector, which is typically applied in von Hamos spectrometers. So, the spectrometer works in dispersive mode and full spectrum is collected simultaneously. The resolution of the Von Hamos spectrometer is defined by the size (width) of the x-ray source, which is given by the size of the incident beam on the target. In case of irradiation with broad beam slits should be used to limit the size of the x-ray source viewed by the crystal.

Another option is the spectrometer employing the Rowland circle focusing geometry presented in Figure 3.14. A Rowland focal circle with a radius R can be defined and the crystal is bent in the dispersion plane to the radius $2R$ so that the crystal planes are parallel to the crystal surface. This is so-called Johann geometry [104] and for a point source on the Rowland circle the Bragg condition is fulfilled for each point on the crystal surface positioned on the focal circle and reflected x-rays are focused back to a single point situated symmetrically on the other side of the focal circle. Such point-to-point focusing

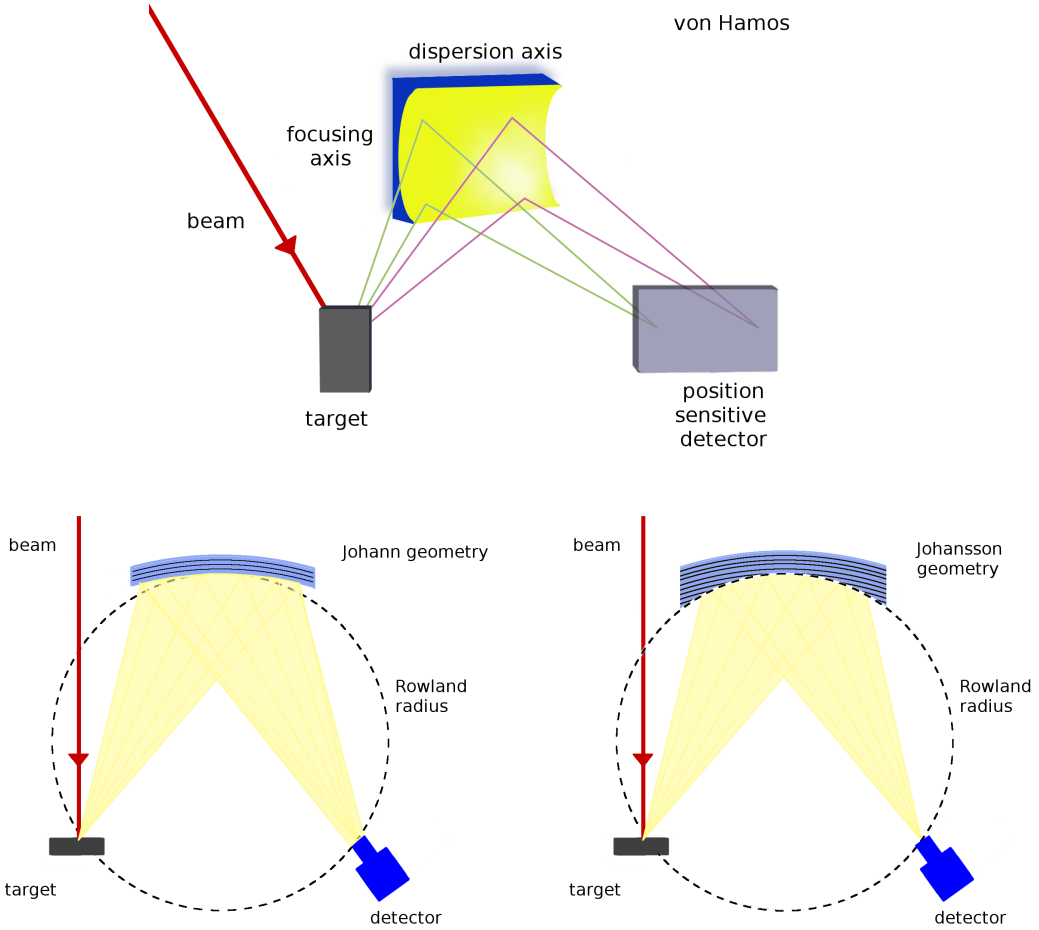


Figure 3.14: The schematic presentation of the Von Hamos (*top*), Johann (*left bottom*) and Johansson geometry (*right bottom*).

spectrometer therefore operates in a single channel mode and a scanning of the Bragg angles is required to record a full spectrum. In Johann type spectrometers the reflected point is in fact slightly broadened because only the central point of the crystal is positioned exactly on the Rowland circle. This problem is solved in the Johansson geometry [105] where the surface of the crystal is grounded to a radius R matching the focal circle, while the crystal planes are still bent to the radius $2R$. In this case the Bragg condition is fulfilled across the whole crystal surface and the Johansson geometry in principle provides theoretically exact focusing improving the energy resolution of the spectrometer.

3.4 Measurements of $K\alpha$ and $K\beta$ XES Spectra of P, S, and Cl Compounds

The $K\alpha$ (core-to-core) and $K\beta$ (valence-to-core) XES spectra were recorded on a set of third-row elements containing compounds. In order to cover different electronic structures of third-row elements a representative set of compounds was selected. The list of all measured compounds is presented in Table 3.3. They were purchased as powder reference materials and then pressed into pellets. The diameter of the pellets was 12 mm with the thickness of several millimeters. The pellets were glued on an Al plate which is used to mount them on the target holder of the spectrometer.

Table 3.3: The chemical formula and the name of compounds used in this thesis.

Phosphorus		Sulfur		Chlorine	
chemical formula	name	chemical formula	name	chemical formula	name
Fe_2P	Iron (III) phosphide	FeS	Iron(II) sulfide	$AlCl_3$	Aluminum chloride
$CaH_4O_4P_2$	Calcium hypophosphite	MoS_2	Molybdenum disulfide	$CaCl_2$	Calcium chloride
Na_2HPO_3	Disodium hydroge phosphite	PbS	Lead(II) sulfide	CsCl	Cesium chloride
$Al(PO_3)_3$	Aluminum metaphosphate	ZnS	Zinc sulfide	$CuCl_2$	Copper(II) chloride
$Ba(PO_3)_2$	Barium metaphosphate	pure S8	Cyclo-octasulfur	KCl	Potassium chloride
$CaFO_3P$	Calcium fluorophosphate dihydrate	Na_2S2O_4	Sodium hydrosulfite	$MgCl_2$	Magnesium chloride
K_3PO_4	Tripotassium phosphate	Na_2S2O_5	Sodium metabisulfite	NaCl	Sodium chloride
KH_2PO_4	Monopotassium phosphate	Na_2SO_3	Sodium sulfite	$KClO_3$	Potassium chlorate
Na_2HPO_4	Disodium phosphate	H_3NSO_3	Sulfamic acid	$NaClO_3$	Sodium chlorate
$Na_4P_2O_7$	Tetrasodium pyrophosphate	$BaSO_4$	Barium sulfate	$KClO_4$	Potassium perchlorate
NaH_2PO_4	Monosodium phosphate	$FeSO_4$	Iron(II) sulfate heptahydrate		
		K_2SO_4	Potassium sulfate		
		Na_2SO_4	Sodium sulfate		

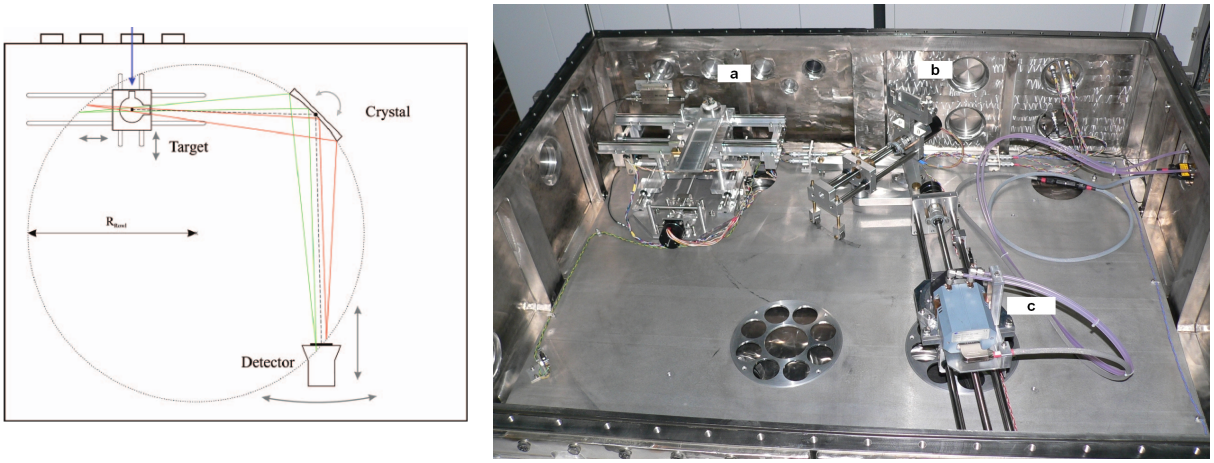


Figure 3.15: *(left)* The geometrical layout of the JSI tender x-ray emission spectrometer. *(right)* The photo of the spectrometer showing the target holder *(a)*, the analyzer crystal holder *(b)*, and the CCD detector *(c)* [4].

Measurements of proton-induced XES spectra were carried out at the 2 MV tandem accelerator of the J. Stefan Institute in Ljubljana and the measurements of photoexcited phosphorus spectra were performed at ID26 beamline of the European Synchrotron Radiation Facility (ESRF) in Grenoble. In both experiments the in-vacuum Johansson type single crystal spectrometer for high-resolution x-ray emission spectroscopy in tender x-ray range was used [4]. The schematic picture of the spectrometer showing the geometrical layout is presented in Figure 3.15 and the photo of the spectrometer within the vacuum chamber is presented in the same Figure. The spectrometer operates in a slightly modified off-Rowland circle geometry. The analyzing crystal and x-ray detector are positioned on the focal circle, while the target is moved within the circle closer to the crystal analyzer. The target position inside the Rowland circle has two important consequences. First, a broad beam can be used for target excitation without any major deterioration of energy resolution. Second, dispersive mode of operation is achieved. Therefore, the full spectrum is measured without moving the crystal or the detector which is crucial for the precise chemical shift measurements.

The incident beam hits the target holder, which is tilted at the angle of 45° and the induced x-rays are emitted at the angle 90°, respectively, to the incoming beam direction. The target holder is equipped with two x, y motors. They are used to align the target with respect to the crystal and the incident beam. The target crystal distance cannot be changed continuously because of the four fixed beam entrance ports. In all our measurements, we have used the second entrance port and the target-crystal distance was fixed to 42 cm. Up to ten samples can be mounted simultaneously on the motorized target holder which is used to exchange the targets without opening the chamber of the spectrometer.

X-rays emitted from the surface are diffracted by the analyzer crystal positioned on the Rowland circle. The crystal size is 70 mm×30 mm and it is curved to the Rowland circle radius of 500 mm. Different crystals are used depending on the measured x-ray energies. In case of P sample the first-order reflection by the $(10\bar{1}0)$ plane of the SiO_2 crystal ($2d = 8.510\mathring{A}$) was used, while the first-order reflection of a Si(111) crystal ($2d = 6.271\mathring{A}$) was used for the measurements of S and Cl compounds. After the diffraction on the crystal, the x-rays are detected according to the diffracted angle by using the charge coupled device (CCD) camera. The CCD chip is thermoelectrically cooled down to −40°C and contains 770×1152 pixels with the pixel size of $22.5 \times 22.5\ \mu m^2$. The crystal and CCD

are mounted on the rhombic stage that enables the rotation of the crystal axis and the detector holder arm, respectively, to adjust the Bragg angle. The detector arm is equipped with an additional independent linear stage that positions the detector on the Rowland circle for each given Bragg angle. Since in the tender x-ray range, full in vacuum operation is mandatory, the complete spectrometer is enclosed in $1.6 \times 1.3 \times 0.4$ m^3 vacuum chamber evacuated by a turbo molecular pump down to 10^{-6} mbar. The Bragg angles which can be reached are restricted by the size of the vacuum chamber to the 30°- 65° Bragg angular range.

The diffraction image recorded by the CCD detector for a given crystal-detector position corresponding to a particular Bragg angle is used to obtain the final emission spectrum. The horizontal axis of the detector corresponds to the dispersion axis and diffracted photons are detected at different horizontal positions according to their wavelength. The vertical axis of the detector serves mainly to accumulate more statistics and the final spectrum is obtained by projecting the image on the horizontal axis. This position spectrum is finally converted into energy scale using the reference line within the spectrum and the nominal $2d$ crystal lattice spacing, detector pixel size, and the crystal-detector distance controlled by the stepper motor driving the linear sledge along the arm of the detector holder. In our experiment the positions of $K\alpha_1$ line of the K_3PO_4, pure S, and NaCl compounds with corresponding reference energies of 2014.5.54 [106], 2307.89 [107], and 2622.44 [107] eV, respectively, were used. In case of the $K\beta$ spectra the $K\beta_{1,3}$ line position of the K_3PO_4, Na_2SO_4 and NaCl compounds with reference energies 2138.0 [48], 2467.15 [22] and 2815.11 [108] eV were used to convert position spectra into energy scale.

The width of the detector defines the energy bandwidth recorded simultaneously at a fixed crystal detector position. In our measurements the bandwidth covered by a single CCD width for the detector positioned at the central Bragg angle, corresponding to the $K\alpha$ emission line were 44, 28, and 53 eV for P, S and Cl $K\alpha$ measurements, respectively. In case of $K\beta$ spectra, smaller Bragg angle results in a slightly larger energy window of 56, 39 and 71 eV for the same elements. An example of the diffraction image recorded by the CCD detector and the final energy spectrum is presented in Figure 3.16 for the case of pure S target bombarded by 2 MeV protons.

For our study, one of the most important parameters of the spectrometer is the energy resolution, which should reach the K shell core-hole lifetime broadening of the third-row elements. The experimental energy resolution of the spectrometer is discussed in more detail in [4]. A few main contributions to the energy resolution of the spectrometer are highlighted here. First, the contribution of the pixel size of the CCD detector is given by

$$\frac{\Delta E}{E} = \frac{W_{pixel}}{2R_{Rowl}\sin\theta_B}\cot\theta_B \tag{3.22}$$

where R_{Rowl} is the Rowland circle and W_{pixel} is the pixel width of the CCD. The absorption of keV photons induces the charge in the pixel, but in many cases this charge is split between neighboring pixels. It was demonstrated that broadening of about two times of the pixel size can be expected from the splitting events. So, the contribution of the pixel size to the energy resolution $\Delta E/E$ of the spectrometer is estimated in the range of $2.3\times10^{-5} - 1.6\times10^{-4}$ for the allowable Bragg angles. Next contribution to the final energy resolution comes from the finite height of the x-ray spot on the target. The divergence in the vertical dimensions results in a slightly curved vertical focal line on the detector. The finite height of the x-ray source, h_{source}, produces broadening of the focal line on the detector and this contribution to the energy resolution can be estimated by

$$\frac{\Delta E}{E} = \frac{h^2_{source}}{8(2R_{Rowl}\sin\theta_B)^2}\cot^2\theta_B. \tag{3.23}$$

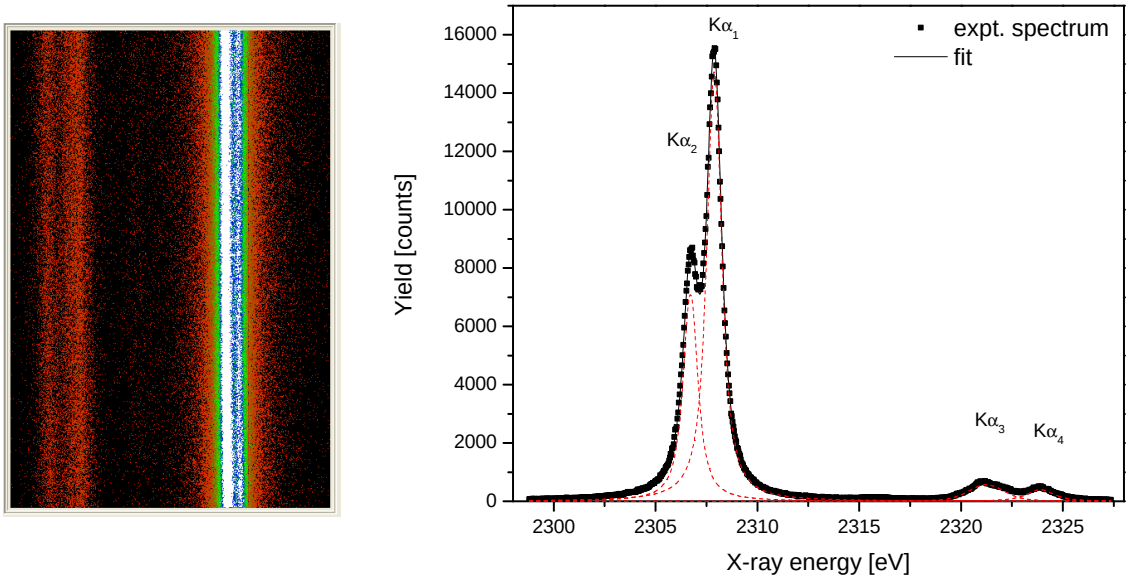


Figure 3.16: *(left)* The CCD image corresponding to $K\alpha$ spectrum of pure S target induced by 2 MeV protons. *(right)* High energy resolution S $K\alpha$ proton-induced spectrum decomposed by the fitting model. The $K\alpha_{3,4}$ satellite line on the high energy side is due to KL double ionization induced in proton-atom collision.

In case of proton excitation, when broad beam in the range of few millimeters is used, the contribution is in the range $10^{-6} - 10^{-4}$ for the limiting Bragg angles that can be reached by the spectrometer. The ultimate limitation of the spectrometer resolution is the intrinsic crystal broadening, which is discussed in Section 3.3.1. In case of cylindrically bent crystal, the intrinsic broadening is slightly enlarged due to the bending variations and crystal imperfections. The width of the Darwin reflectivity curve for the crystal bent to 1 m radius is estimated to be in the order of 0.2 mrad yielding final value of $\Delta E \sim 0.2 - 0.4$ eV. Based on these values the expected energy resolution of the spectrometer $\Delta E/E$ is estimated to be $\sim 1 - 2 \times 10^{-4}$. This was confirmed also experimentally at the synchrotron by recording the signal of the elastic scattering yielding 1.3×10^{-4}. Very high experimental energy resolution is presented also in our XES spectra. In the $K\alpha$ proton-induced spectrum of pure S presented in Figure 3.16 the $K\alpha_1$, $K\alpha_2$ spin orbital splitting of 1.115 eV [99] is clearly resolved indicating sub eV energy resolution. A more quantitative value can be obtained by fitting a model spectrum to the experimental one as also presented in Figure 3.16.

The experimental $K\alpha_{1,2}$ spectra were fitted by two Voigt functions, which is a convolution of the Lorentzian natural line shape with Gaussian profile corresponding to the response function of the spectrometer. The Lorentz linewidths were taken from Ref. [99] and fixed for both lines, where the width of Gaussian functions was a free parameter. Two additional Voigt profiles were added in the model spectrum to account for additional spectral lines $K\alpha_{3,4}$ on the high energy side of the $K\alpha$ diagram line. These lines correspond to the 1s→2p transitions in the KL doubly ionized atom. From Figure 3.16 it can be seen that this fitting model almost perfectly reproduced the measured spectrum. The FWHM values of the Gaussian component determined from the fit can be used as an experimental

energy resolution. In case of P photoexcited XES spectra at ESRF the energy resolution was ~ 0.4 eV, while in case of PIXE measurements using broad beam the experimental energy resolution was determined between 0.50 and 0.60 eV, depending on the Bragg angle corresponding to each of three measured elements.

This experimental setup was therefore applied to record $K\alpha$ and $K\beta$ XES spectra of P, S, and Cl in different compounds. In case of phosphorus two sets of spectra were recorded using monochromatic synchrotron radiation and MeV proton excitation, respectively. In case of S and Cl compounds only proton excitation was used. For the P photoexcited measurements performed at ESRF the incident photon beam was focused down to 250×50 μm^2, the photon energy was tuned to 3 keV and the photon flux on the target was $\sim 5\cdot10^{12}$ photons/s. In all PIXE measurements a broad unfocused proton beam with 8×8 mm^2 cross section was used. The energy of the proton beam was set to 2 MeV and the current was in the range of 50-100 nA.

The count rate at the top of P $K\alpha_1$ line was around 60 counts/s and approximately 30 times lower in case of $K\beta$ emission lines for synchrotron measurements with corresponding acquisition times 500 and 2500 s. In case of PIXE measurements the count rate at the top of P $K\alpha_1$ line was 2 counts/s and for S and Cl samples the count rate increased to 10 counts/s. This change in count rate is repercussion of the lower reflection of SiO_2 analyzer crystal used in P measurements in comparison to Si(111) crystal used in S and Cl measurements. An overall acquisition time per target was 2000 s for P and it was reduced to 500 s for S and Cl compounds. For the Kβ emission lines the count rates were approximately 30 times lower so the total acquisition times were increased to several hours in the PIXE experiment. In order to avoid radiation damage during long measurements, accumulation of short exposures from several fresh target spots was used to reach reasonable statistics. A few examples of typical $K\alpha$ and $K\beta$ spectra are presented in Figure 3.17 for each of the three studied elements.

The main parameters we have tried to extract from the measured $K\alpha$ spectra were the small energy shifts of the $K\alpha_{1,2}$ emission line, as seen from Figure 3.17. The high energy resolution with good statistics in the measured spectra allows us to extract energy shifts of $K\alpha$ line with high precision. The fitting error of the energy shifts was between 1-2 meV, which is almost negligible. The full spectrum is simultaneously recorded at fixed crystal and detector positions so possible errors introduced by limited precision of the motors are completely avoided. The main source of uncertainty originates from slight random variations in target positions relative to the crystal which are introduced during target exchange and might lead to tiny shifts of the line on the detector. This contribution was determined by the independent measurements of several targets prepared out of the same chemical compound. These targets were mounted on different positions on the sample holder and measurements of the $K\alpha$ line were performed. The standard deviation of the absolute position of the measured lines was 0.40 detector channels. The latter was converted into energy using corresponding Bragg angles yielding final energy uncertainties of 27, 15, and 27 meV for P, S, and Cl measurements, respectively.

In case of $K\beta$ spectra we are predominantly interested in the shape of the spectrum reflecting the chemical environment of the x-ray emitting atom. While XANES spectra collected in fluorescence mode are exposed to self-absorption effects leading to large uncertainties, the self-absorption should generally not influence the XES spectra of single valence systems. In order to confirm this property of XES technique we have measured $K\beta$ spectra of pure S diluted with boron nitride (BN) to different concentrations, and measured spectra are presented in Figure 3.18. The shape of the spectra is independent from the S/BN ratio, only acquisition time increases as the amount of S compound in target decreases. Therefore, any additional correction of the $K\beta$ spectral shape is not required.

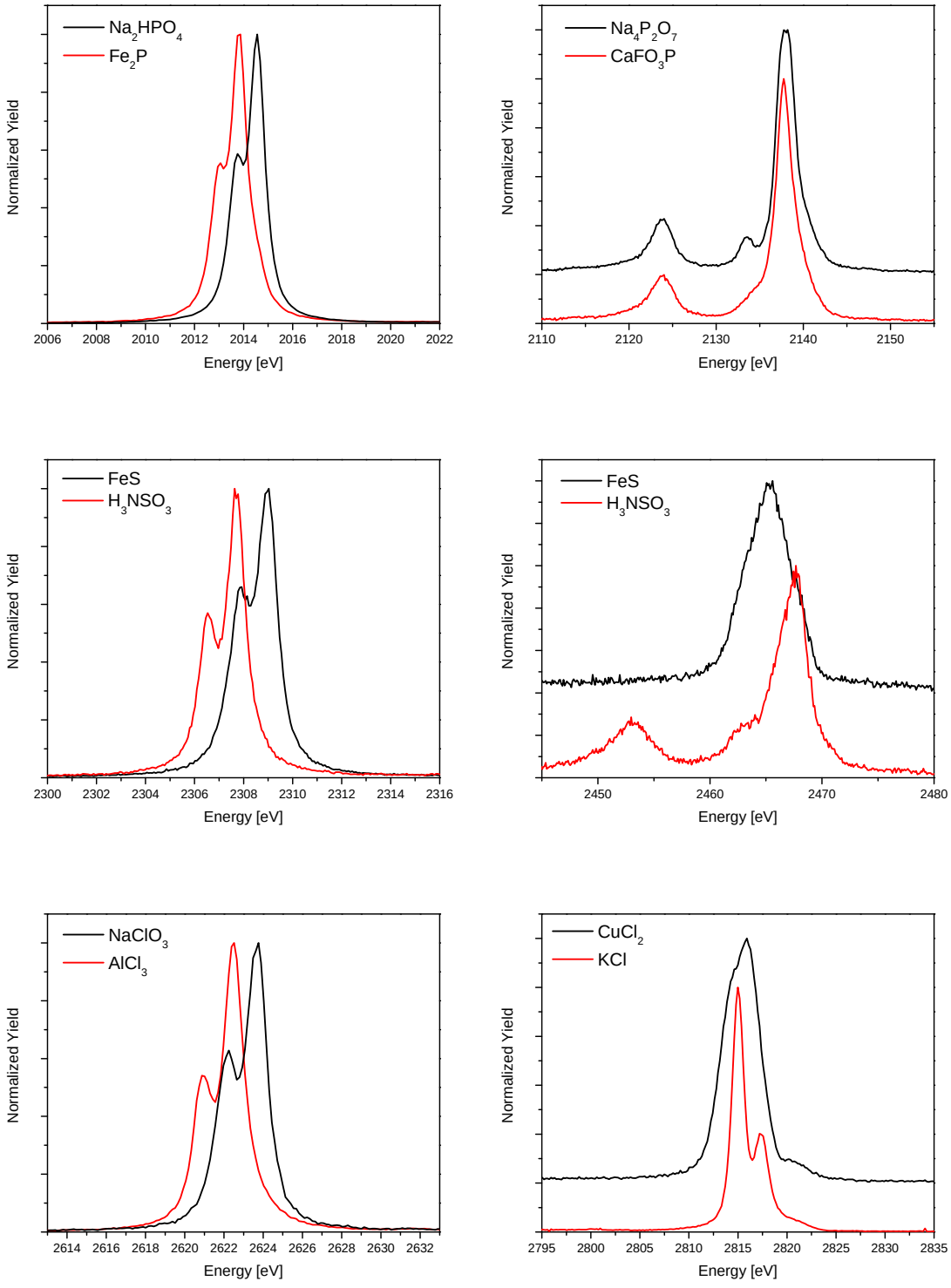


Figure 3.17: The examples of the high energy resolution experimental $K\alpha$ *(left)* and $K\beta$ *(right)* x-ray emission spectra of the P, S, and Cl compounds from the top to bottom.

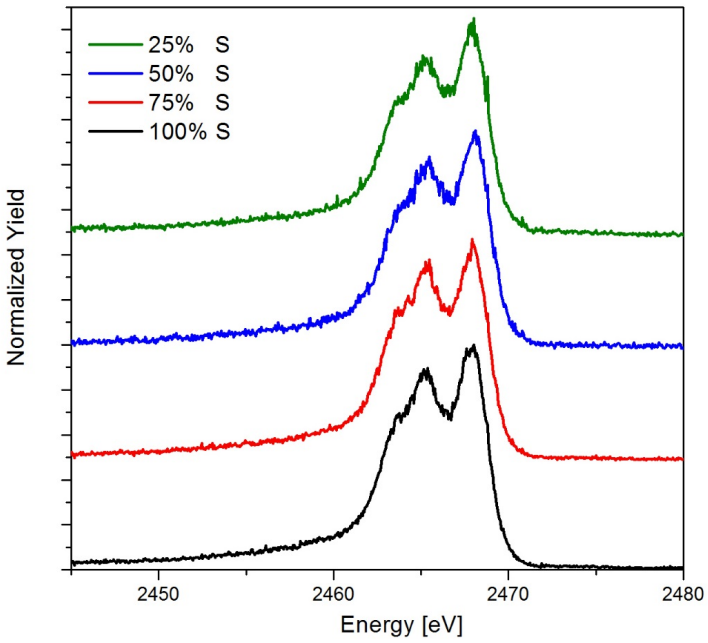


Figure 3.18: High resolution $K\beta$ emission spectra of pure S diluted with BN.

Chapter 4

Results

In this chapter the final experimental and theoretical results are presented. We start with the analysis of measured $K\alpha$ x-ray emission energies correlated with the formal oxidation state and the effective local charge of the central atom, which can be used to determine the oxidation state of third-row elements in different chemical environments. This is followed by the analysis of measured $K\beta$ spectral shape demonstrating that the electronic structure is defined by the local symmetry of the molecular system. The influence of the hydrogen covalent bonding breaking the tetrahedral symmetry of the phosphate ion is discussed next, followed by the analysis of a slightly larger more complex molecular system. Finally, the S XES spectra of lithium polysulfides (Li_2S_x) are studied experimentally and theoretically to explore the potential of XES spectroscopy for characterization of sulfur within the Li-S battery.

4.1 Oxidation State Analysis Using Core-to-Core XES

The $K\alpha$ line corresponds to the electron transition between deep atomic like $2p$ and $1s$ orbitals and is the most intense line in K x-ray emission spectrum. Since the emitted spectrum corresponds to core-to-core (CtC) electron transition, the spectral shape exhibits a typical Lorentz-shaped atomic $K\alpha_{1,2}$ doublet structure. This can be seen in the measured $K\alpha_{1,2}$ lines for each of three investigated elements corresponding to compounds with the highest and the lowest formal oxidation state in Figure 4.1. The high experimental resolution on the level of the natural lifetime broadening allows us to observe tiny energy shifts of the measured $K\alpha$ emission lines depending on the oxidation state of the element in the sample. The experimental $K\alpha_{1,2}$ emission energies were extracted by fitting the measured spectra with two Voigt functions, which is a convolution of the natural Lorentzian shape with the Gaussian function corresponding to the instrumental function of the spectrometer. For both spectral components, the corresponding Lorentzian and Gaussian components were constrained to the same values.

An example of such fit was already presented in the experimental section (Figure 3.16). The final experimental $K\alpha$ emission energies extracted from the fit are tabulated in Table 4.1 for all measured compounds. In case of P compounds the emission spectra were induced with 2 MeV protons and also 3 keV photons, but both sets of spectra are practically the same and differences between extracted energies are below experimental uncertainties so the average energies of both experiments are reported. The experimental 2p level spin orbit splitting was found 0.864(5), 1.180(11), and 1.592(15) eV for the case of P, S, and Cl compounds, respectively, and shows no dependence on the chemical state so only experimental $K\alpha_1$ emission energies are reported in Table 4.1.

From the tabulated values, a clear trend is observed for measured compounds of all

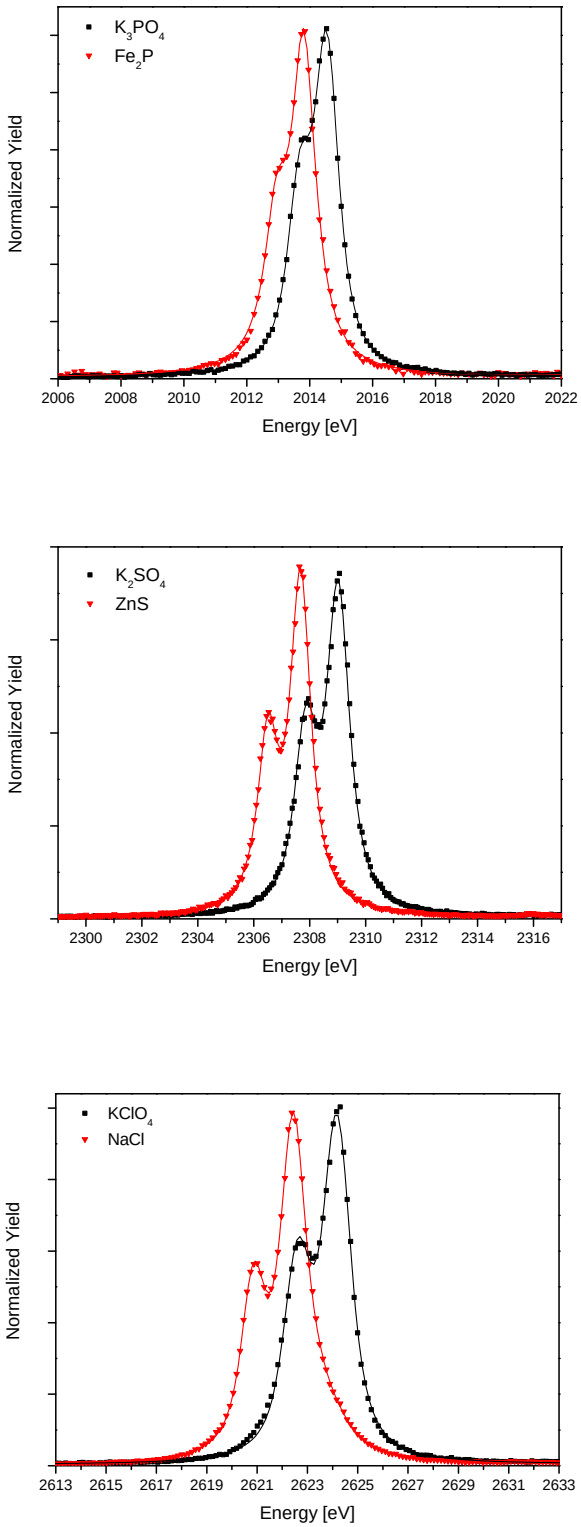


Figure 4.1: The high energy resolution $K\alpha_{1,2}$ x-ray emission spectra of two P *(upper)*, *S (center)*, and Cl *(bottom)* compounds corresponding to the lowest and the highest oxidation state. All spectra were induced by 2 MeV proton beam.

Table 4.1: The experimental $K\alpha_1$ emission energies of various phosphorus, sulfur and chlorine compounds extracted from the fit.

Phosphorus			Sulfur			Chlorine		
chemical formula	oxidation state	$K\alpha_1$[eV] measured	chemical formula	oxidation state	$K\alpha_1$[eV] measured	chemical formula	oxidation state	$K\alpha_1$[eV] measured
Fe_2P	3−	2013.80	FeS	2−	2307.71	$AlCl_3$	1−	2622.49
$CaH_4O_4P_2$	1+	2014.22	MoS_2	2−	2307.77	$CaCl_2$	1−	2622.47
Na_2HPO_3	3+	2014.43	PbS	2−	2307.71	CsCl	1−	2622.46
$Al(PO_3)_3$	5+	2014.60	ZnS	2−	2307.69	$CuCl_2$	1−	2622.54
$Ba(PO_3)_2$	5+	2014.52	pure S8	0	2307.89	KCl	1−	2622.45
$CaFO_3P$	5+	2014.53	Na_2S2O_4	3+	2308.33	$MgCl_2$	1−	2622.49
K_3PO_4	5+	2014.53	Na_2S2O_5	4+	2308.55	NaCl	1−	2622.44
KH_2PO_4	5+	2014.52	Na_2SO_3	4+	2308.67	$KClO_3$	5+	2623.68
Na_2HPO_4	5+	2014.55	H_3NSO_3	5+	2308.97	$NaClO_3$	5+	2623.68
$Na_4P_2O_7$	5+	2014.51	$BaSO_4$	6+	2309.06	$KClO_4$	7+	2624.19
NaH_2PO_4	5+	2014.54	$FeSO_4$	6+	2309.08			
			K_2SO_4	6+	2309.05			
			Na_2SO_4	6+	2309.07			

three elements. The $K\alpha$ line is shifted towards higher emission energy with increasing formal oxidation state. The absolute energy shifts yielding values around 0.8, 1.3, and 1.7 eV between the lowest and highest oxidation state of P, S and Cl elements, respectively. In Figure 4.2 the experimental $K\alpha_1$ emission energies are plotted versus formal oxidation state for each of three elements studied in this work and a high correlation is observed. On the other hand, measured energies for different compounds with the same oxidation state tabulated in Table 4.1 basically match each other indicating similar valence electron configuration, e.g. phosphate (5+), sulfate (6+) or chloride (1-).

Table 4.2: Calculated energy position of $K\alpha_1$ lines and DFT-calculated valence electron population of the first coordination sphere of P compounds.

chemical formula	oxidation state	$K\alpha_1$[eV] calculated	DFT electron configuration
Fe_2P	3−	2013.78	$3s^{1.66}3p^{2.97}3d^{0.11}$
$H_2O_2P^{1-}$	1+	2014.32	$3s^{1.04}3p^{2.48}3d^{0.44}$
HPO_3^{2-}	3+	2014.43	$3s^{0.89}3p^{2.38}3d^{0.53}$
PO_4^{3-}	5+	2014.54	$3s^{0.70}3p^{1.79}3d^{0.54}$

In order to enable a more quantitative analysis DFT calculations of the $K\alpha$ emission energies were performed. We have started with the calculations of P compounds and first considered only the first coordination sphere around the phosphorus atom. The calculated energy values for the Fe_2P molecule and $H_2O_2P^-$, HPO_3^{2-} and PO_4^{3-} ions are presented in Table 4.2 and already these calculations, including only first neighbors, reproduced very well the measured energy shifts. In the next step we have expanded the calculation also to other compound and additional coordination spheres were included in calculations in order to account for the neutral molecules. Since we could not achieve convergence for every measured system, only calculations of four representative samples are performed and presented together with measurements values in Figure 4.2. In case of P^{5+} group the average calculated value of different phosphate is plotted with standard deviation of the calculated values given as error bar. In order to provide absolute energies, which can be directly compared to experimental values, an overall shift of -1.16 eV (P), +0.77 eV (S),

and +3.34 eV (Cl) was applied to all calculated energies. Most importantly, the theory also confirmed clearly the correlation of $K\alpha$ emission energies with the oxidation state as observed in the experiment.

The explanation of the small chemical shift of the CtC emission spectra can be found if we look at the valence electron population. The chemical environment of the center atom slightly modifies the electron density of the investigated atoms. Therefore, variation of the valence electrons population affects the screening of the nuclear potential experienced by core electrons producing chemical shifts. These shifts depend on the oxidation state confirmed by our experimental and theoretical values. Measured $K\alpha$ emission energies of different compounds with the same oxidation state are almost the same, with two exceptions indicating some differences in the valence electron configuration. The first small exception is the $Al(PO_3)_3$ exhibiting slightly higher energy compared to other P(5+) compounds. This can be explained qualitatively with larger Al electronegativity compared to other metal ligands (Na, K) which increases phosphorus effective charge and consequently the energy of $K\alpha$ line. The second interesting exception which we would like to study in more detail are two sulfur samples with the same formal oxidation state (4+) but with different energies of $K\alpha$ emission energies. In case of Na_2SO_3 and $Na_2S_2O_5$ compounds the difference in measured $K\alpha$ emission energy is 0.12 eV, which is significant compared to scattering of measured energies within other compounds of the same oxidation number. Also, the difference is larger than three times measured uncertainty (15 meV, see 3.4) and therefore cannot be assigned to statistical fluctuations. This difference is qualitatively explained by the number of oxygen atoms per single S atom, which is smaller in $Na_2S_2O_5$ compared to Na_2SO_3. Because oxygen atoms have large electronegativity, they slightly overtake electrons from the sulfur atom. This leads to the increase of the local electronic charge of the sulfur atom in $Na_2S_2O_5$ compared to Na_2SO_3, yielding slightly lower $K\alpha$ emission energy of $Na_2S_2O_5$ compound.

Table 4.3: Calculated energy position of $K\alpha_1$ lines and DFT-calculated valence electron population.

chemical formula	oxidation state	$K\alpha_1$[eV] calculated	DFT electron configuration
Fe_2P	3−	2013.78	$3s^{1.66}3p^{2.97}3d^{0.11}$
$CaH_4O_4P_2$	1+	2014.22	$3s^{1.10}3p^{2.50}3d^{0.41}$
Na_2HPO_3	3+	2014.38	$3s^{0.89}3p^{2.40}3d^{0.52}$
$CaFO_3P$	5+	2014.44	$3s^{0.72}3p^{2.41}3d^{0.58}$
K_3PO_4	5+	2014.46	$3s^{0.74}3p^{2.49}3d^{0.56}$
KH_2PO_4	5+	2014.64	$3s^{0.72}3p^{2.31}3d^{0.58}$
Na_2HPO_4	5+	2014.63	$3s^{0.73}3p^{2.39}3d^{0.57}$
NaH_2PO_4	5+	2014.56	$3s^{0.75}3p^{2.32}3d^{0.57}$
ZnS	2−	2307.85	$3s^{1.87}3p^{4.16}3d^{0.03}$
$Na_2S_2O_5$	4+	2308.55	$3s^{1.67}3p^{3.02}3d^{0.40}$
Na_2SO_3	4+	2308.59	$3s^{1.67}3p^{2.89}3d^{0.38}$
K_2SO_4	6+	2308.97	$3s^{1.05}3p^{3.03}3d^{0.66}$
NaCl	1−	2622.64	$3s^{1.97}3p^{5.59}3d^{0.00}$
$KClO_3$	5+	2623.63	$3s^{1.76}3p^{3.71}3d^{0.40}$
$NaClO_3$	5+	2623.65	$3s^{1.76}3p^{3.69}3d^{0.40}$
$KClO_4$	7+	2624.07	$3s^{1.31}3p^{3.57}3d^{0.68}$

In order to provide more explicit quantitative explanation, the Mulliken population

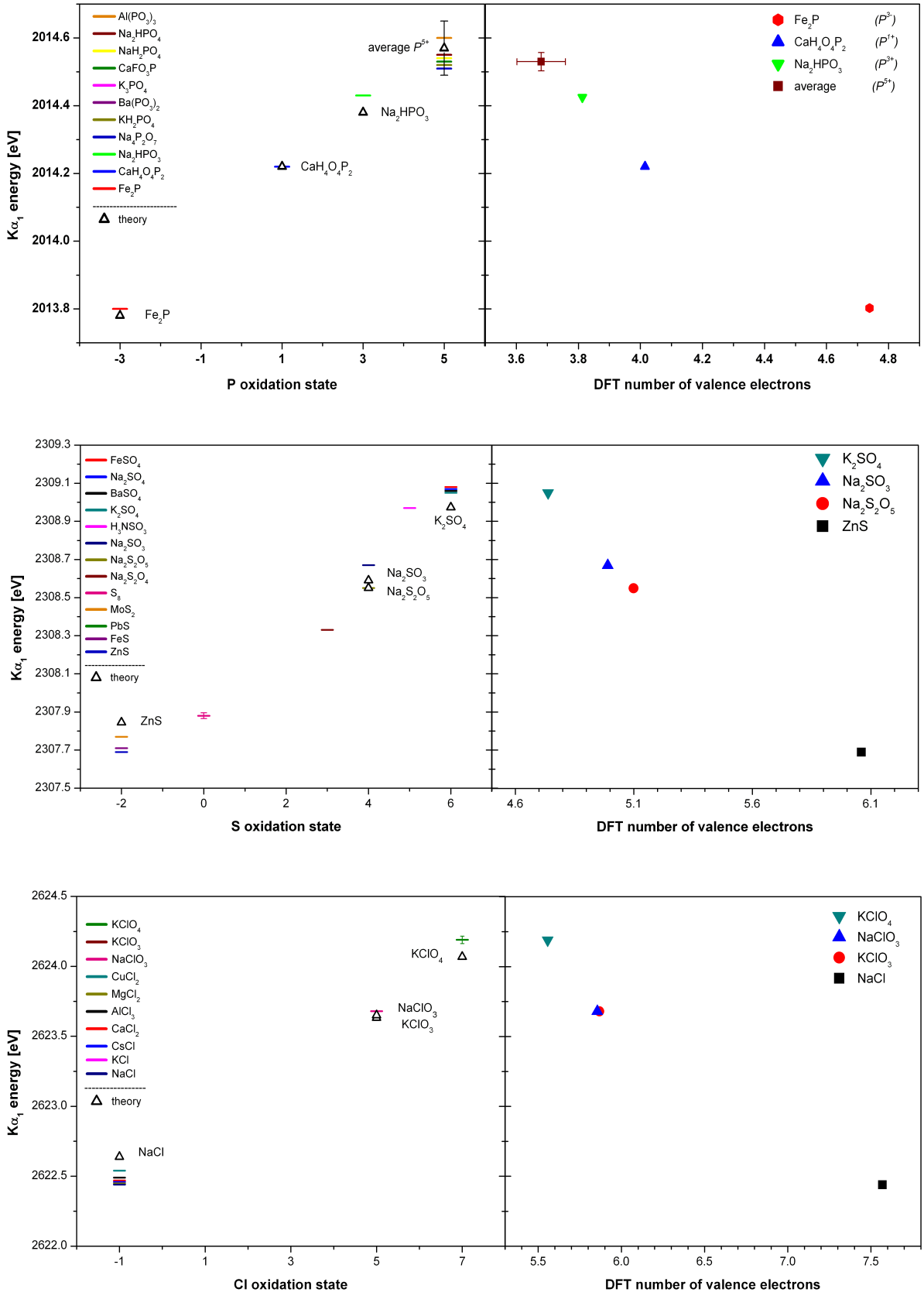


Figure 4.2: *(left)* The experimental and theoretical $K\alpha_1$ emission energies versus formal oxidation state. *(right)* The experimental $K\alpha_1$ emission energies vs DFT calculated number of valence electrons.

analysis of the valence electrons distribution was done on the DFT calculated ground state electron density. The theory enables us to determine small differences in effective electronic charge of compounds with the same oxidation number. The results of such analysis are presented in Table 4.3, where the numbers in the superscript of s, p, and d labels represent the electron charge in valence orbitals ($3s$, $3p$, and $3d$) of P, S or Cl atoms. In case of sulfur 4+ oxidation state, the DFT valence electron populations show an increase of the effective electronic charge (number of valence electrons) for S atom within $Na_2S_2O_5$ compared to Na_2SO_3 compound. The Mulliken population analysis confirms the upper discussion that the difference in the measured energy of the $K\alpha$ line originates from the difference in the valence electron population for S atom in these two compounds. On the other hand, the compounds with the same oxidation number and similar measured $K\alpha$ energy also have very similar effective electronic charge, e.g. phosphate group or $KClO_3$ and $NaClO_3$ compounds. In Figure 4.2 the measured $K\alpha$ energies are plotted versus the DFT calculated number of valence electrons. Compared to the dependence on the formal oxidation number, the degree of correlation between the two variables is enhanced even further and an almost perfect correlation is observed in this plot with the Na_2SO_3 and $Na_2S_2O_5$ compounds ordered directly in accordance with their calculated effective charge. The $K\alpha$ emission energy, therefore, reflects with high accuracy the valence electron population and can be used to determine the effective charge of the central P, S, and Cl atoms in a different chemical environment.

The $K\alpha$ emission spectra of all three elements show clear dependence on the oxidation state of the element in the sample. The spectral shape exhibits a pure atomic-like $K\alpha_{1,2}$ structure for all three studied elements and is not influenced by the chemical environment. On the other hand the screening of the nuclear potential is affected by the valence orbital electron population. The high experimental resolution on the level of natural lifetime broadening allows us to record tiny energy shifts of the measured $K\alpha$ emission lines in correlation with the oxidation state of the element in the sample. The energy shift of $K\alpha$ line between the lowest and the highest oxidation state in P, S, and Cl is typically an order of magnitude smaller compared with the corresponding shifts measured in the absorption spectra. However, due to the relatively simple and narrow line shape, the energy shift can be determined with very high precision and can be used effectively as a clean and robust merit of the oxidation state and effective electronic charge of P, S, and Cl elements in the sample.

In many cases the analyzed samples might be composed as mixtures of several molecular systems with different oxidation states and the determination of selective amounts of single valence configuration might be of crucial importance. A relatively simple and narrow $K\alpha_{1,2}$ lineshape, with high sensitivity of $K\alpha$ energy to the oxidation state of element in sample, allows us to use CtC emission spectroscopy to determine the amount of particular species in mixed valence systems. In order to test the possibility of doing this type of analysis, we have measured $K\alpha$ spectrum from the mixed ZnS and Na_2SO_4 powder sample (Figure 4.3). The pure ZnS and Na_2SO_4 powders were mixed in 2.5:1 molar quantity ratio, so the corresponding mass percentage of S in the oxidation state 2- should be 71.4%. The measured spectrum has three characteristic peaks and it was fitted with two Voigt doublets corresponding to the S $K\alpha_{1,2}$ lines of pure ZnS and Na_2SO_4 compounds. The only free parameter in the fitting procedure was the intensity ratio of two Voigt doublets, which reflects the ratio of S in oxidation state 2- and 6+ in the mixed sample. The fitting model reproduced the measured spectrum and the intensity of both components was extracted. The percentage of S^{2-} obtained from the fit was 73.4(2)%, which is slightly larger than the expected value. In case of heterogeneous powder samples with a relatively large grain size exceeding the x-ray absorption length, which is in case of $K\alpha$ MeV proton-induced emission

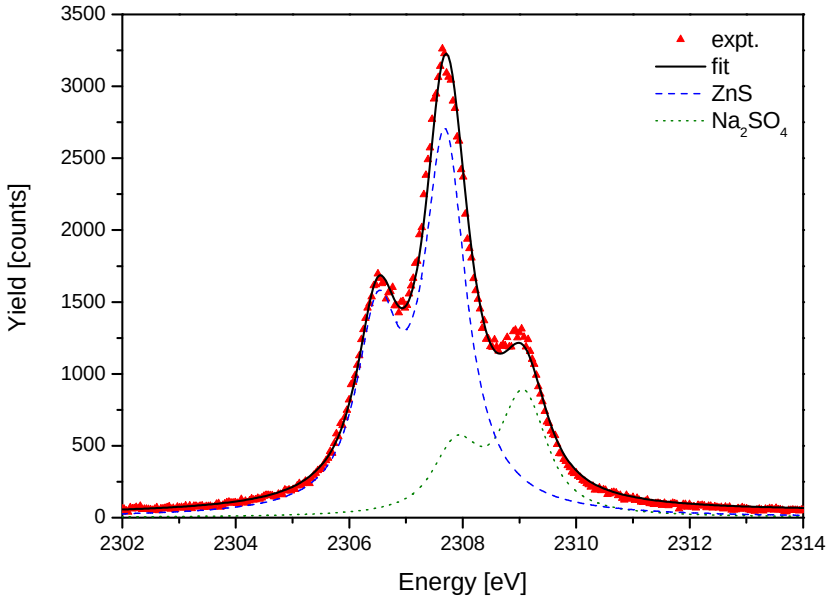


Figure 4.3: S $K\alpha$ emission spectrum of ZnS / Na_2SO_4 mixed sample fitted with a linear combination of pure ZnS and Na_2SO_4 reference measured spectra.

of P, S, and Cl between 10-20 μm, different self-absorption of separate single-compound grains might influence the overall accuracy of such multi-valence compound systems. So, the small discrepancy between nominal and measured value can be attributed to the self absorption in different grains.

Another important aspect in this type of oxidation state analysis is the minimum detection limit (MDL). The corresponding detection limit was evaluated following the procedure used previously in the HR-PIXE analysis [109]. In general, the MDL is defined by the peak to background ratio and the width of the measured lines. The FWHM of the S $K\alpha$ line for the pure S sample was recorded yielding a value of 0.87 eV and the count rate of 35 counts/s at the top of the S $K\alpha_1$ line was achieved. In the fitting procedure of our measured spectra an average background level of 0.015 counts/s was determined. With the acquisition time of 1 h and with the proton beam current in the range of 50-100 nA the final value of < 200 ppm was obtained. This value can be improved by an order of magnitude using synchrotron radiation with very high incident photon flux resulting in much higher count rates. On the other hand, an order of magnitude higher concentrations would be typically required not only to detect the signal but also to determine the $K\alpha$ emission energy with sufficient precision. Application of such CtC XES oxidation state analysis on the diluted samples with a concentration of a few 100 is therefore possible using synchrotron radiation. In case of phosphorus the $(10\bar{1}0)$ quartz analyzer crystal is used in the emission spectrometer, which has lower reflectivity compared to the Si(111) crystal used for S and Cl. This results in significantly lower count rates and consequently slightly higher MDLs in the order of a few 1000 ppm can be reached for phosphorus.

4.2 P, S, and Cl Oxides in Different Local Symmetries Studied by Valence-to-Core XES

The $K\alpha$ emission line corresponding to CtC electron transition reflects the valence electron density only indirectly by screening the nuclear potential. On the other hand, the $K\beta$ emission spectrum arises as a result of the dipole transitions from the occupied molecular orbitals in the valence band and therefore yields p-density of occupied valence state providing with high sensitivity information of the chemical environment. Consequently, this valence-to-core(VtC) emission spectrum should directly reflect the local symmetry and chemical environment of the investigated atom. The VtC XES is complementary to the XANES spectroscopy, but an important difference is that XES can be combined with a different (also laboratory) excitation source. In order to experimentally verify that the VtC x-ray emission spectral shape does not depend on the excitation mode phosphorus VtC XES spectra have been recorded using 2 MeV protons and 3 keV monochromatic photon beam and the comparison of the experimental $K\beta$ emission spectra of four different phosphate compounds are shown in Figure 4.4. The measured spectra induced with photon and proton beam are basically the same, the main difference is only better statistics in the synchrotron radiation induced spectra due to higher incident photon flux, similar as in case of CtC spectra.

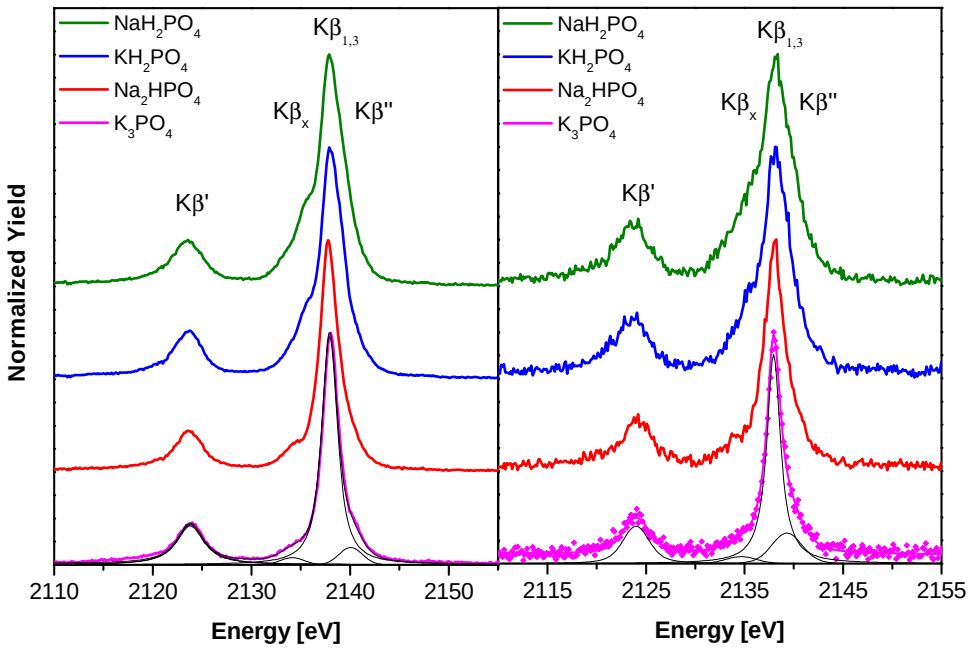


Figure 4.4: P-$K\beta$ emission spectra of four different phosphates induced by *(left)* 3 keV photons and *(right)* 2 MeV protons.

Three sets of compounds with T_d, C_{3v}, and C_{2v} local symmetries corresponding to XO_4^{n-}, XO_3^{n-} and XO_2^n (X=P,S,Cl) ions, respectively, were studied experimentally and theoretically. These three sets were selected to study the influence of local symmetry on the $K\beta$ emission spectra shape. In Figure 4.5 the arrangement of atoms in the molecular

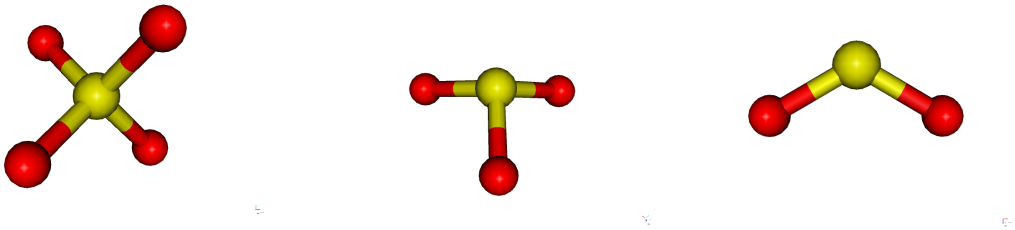


Figure 4.5: The presentation (*left*) of the XO_4^{n-} ion with the T_d local symmetry, (*center*) the XO_3^{n-} ion with C_{3v} local symmetry and (*right*) the XO_2 molecule with C_{2v} local symmetry. The investigated atoms X (X=P, S, or Cl) are presented with yellow and oxygen atoms with red.

Table 4.4: The DFT calculated distances between central P, S, Cl atom and neighboring oxygen atoms in XO_4^{n-} and XO_3^{n-} ions and in neutral molecules. Existing literature crystallographic data is added for comparison.

	Distance between P, S, or Cl and O [Å]		
Molecule name	calculated by StoBe		Literature data
	ion	molecule	
PO_4^{3-}/K_3PO_4	1.615	1.607	1.542 [110]
SO_4^{2-}/K_2SO_4	1.541	1.536	1.486 [111]
$ClO_4^{1-}/\ KClO_4$	1.513	1.512	1.460 [112]
PO_3^{3-}/Na_2HPO_3	1.665	1.575	1.525 [113]
SO_3^{2-}/Na_2SO_3	1.598	1.596	1.500 [98]
$ClO_3^{1-}/NaClO_3$	1.556	1.561	1.485 [114]

structure of T_d, C_{3v}, and C_{2v} local symmetries is schematically presented. The experimental data for distances between the central P, S, and Cl atom and neighboring oxygen atoms for the corresponding neutral molecule are collected in Table 4.4. They can be used to check the quality of our calculated distances, which are also tabulated in Table 4.4. In general, the calculated and experimental distances are in good agreement. Small deviation between the calculated value for the PO_3^{3-} anion and literature data for the Na_2HPO_3 molecule is due to the fact that PO_3^{3-} isolated anion is only a theoretical model and cannot exist in a real system.

4.2.1 Molecular systems with T_d local symmetry

In the top part of Figure 4.6, P, S, and Cl $K\beta$ x-ray emission spectra measured from K_3PO_4, K_2SO_4 and $KClO_4$ compounds are presented. The spectra shape exhibits two main peaks, characteristic for all three compounds. From historical spectroscopic reason these two peaks are commonly labeled as $K\beta'$ and $K\beta_{1,3}$ and we will keep this notation in our work. If the energy resolution of the setup is high enough, two additional side peaks are observed next to the $K\beta_{1,3}$ line usually labeled as $K\beta_x$ and $K\beta''$. In case of P and S spectra, the side peaks are positioned on both sides of the main $K\beta_{1,3}$ line, whereas for Cl spectrum both peaks are shifted on the low-energy side of the $K\beta_{1,3}$ peak. Measured spectra were fitted by a model spectrum composed of four Voigt profiles also presented in Figure 4.6. The experimental energies and intensities of separate spectral components extracted from the fit are tabulated in Table 4.5.

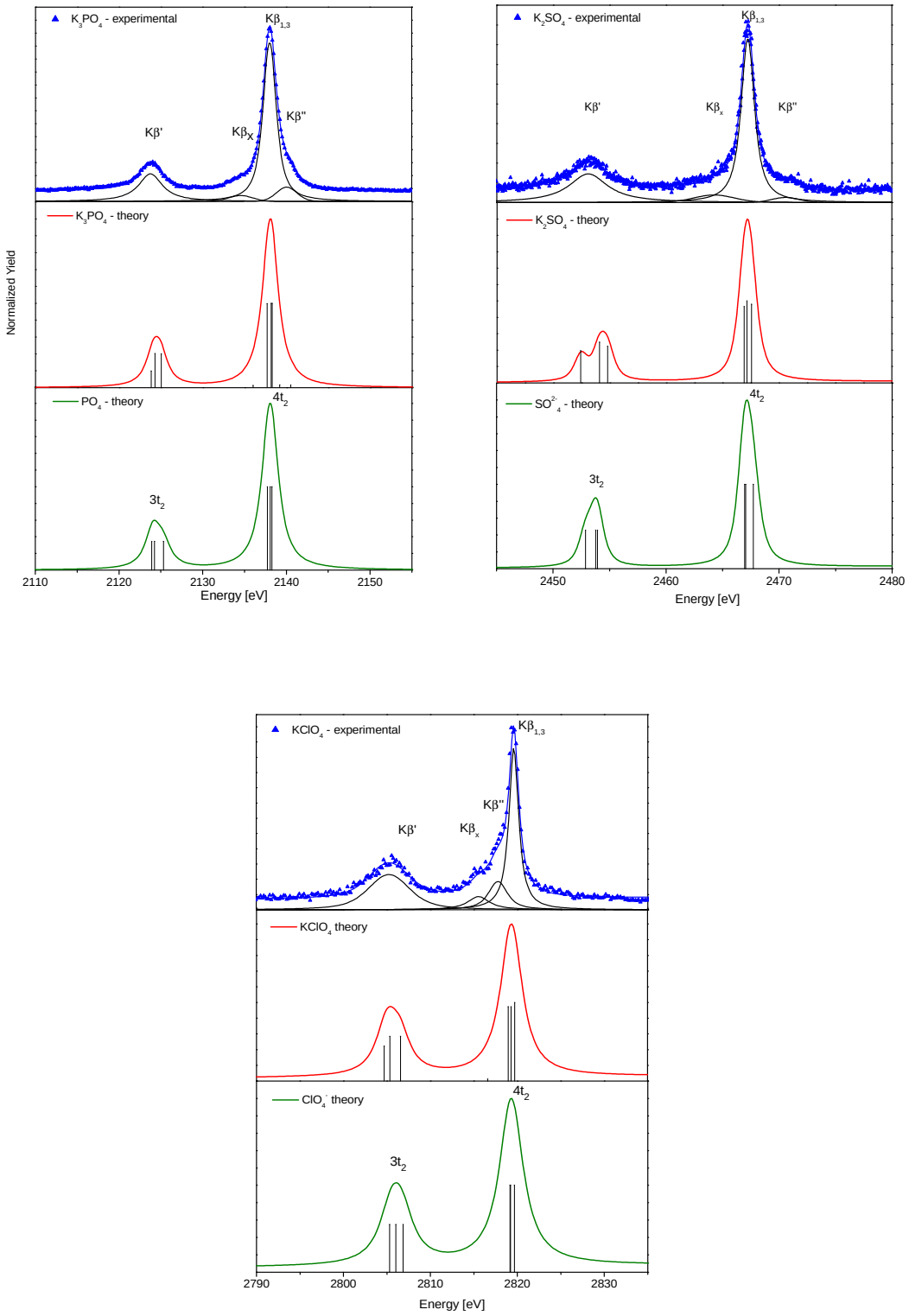


Figure 4.6: Experimental and theoretical $K\beta$ x-ray emission spectra of phosphorus (left), sulfur (center) and chlorine (right) in T_d local symmetry.

Table 4.5: Extracted experimental energies and relative intensities of main spectral components for the K_3PO_4, K_2SO_4 and $KClO_4$ compounds. The error estimates from the fit are given in parentheses.

	$K\beta'$	$K\beta_x$	$K\beta_{1,3}$	$K\beta''$	$K\beta'/K\beta_{1,3}$
K_3PO_4					
Energy [eV]	2123.75(2)	2134.4(2)	2138.03(1)	2140.45(6)	
Intensity [%]	23.1(0.5)	3.8(1.0)	67.4(2.3)	5.7(1.2)	0.34(0.01)
K_2SO_4					
Energy [eV]	2453.10(4)	2464.2(4)	2467.236(5)	2470.6(2)	
Intensity [%]	31.7(1.6)	6.3(1.9)	59.3(2.3)	2.7(1.4)	0.53(0.03)
$KClO_4$					
Energy [eV]	2805.25(7)	2815.5(5)	2819.60(1)	2817.8(2)	
Intensity [%]	34.1(2.3)	8.1(7.8)	44.0(5.6)	13.8(13.7)	0.77(0.11)

Table 4.6: The overall shift of the absolute energy scale applied to each calculated XO_4^{n-} and XO_3^{n-} spectrum.

Molecule name	calculated by StoBe	
	ion	molecule
PO_4^{3-}/K_3PO_4	-3.930	-3.589
SO_4^{2-}/K_2SO_4	-0.992	-1.053
$ClO_4^{1-}/\ KClO_4$	0.891	0.802
PO_3^{3-}/Na_2HPO_3	-3.934	-4.047
SO_3^{2-}/Na_2SO_3	-1.115	-1.089
$ClO_3^{1-}/NaClO_3$	0.979	1.219

In order to interpret the measured spectra, *ab-initio* quantum chemical calculation of the electronic transition corresponding to the $K\beta$ emission spectrum was performed. We have started with the simplest model, incorporating only the first coordination sphere around the center atom building the XO_4^{n-} anions. In the next step the calculations were expanded to the full neutral molecule. The theoretical spectra were built from the calculated line spectra using Voigt profiles. The width of the Voigt profiles was adjusted to match the experimentally observed line shape widths, and an overall shift of the calculated absolute energy scale of a few eV was applied in order to reproduce the experimental spectra. The absolute energy shifts applied to calculated absolute energies are given in Table 4.6. As seen from Figure 4.6, there are no significant differences between the theoretical model spectra of the isolated XO_4^{n-} ion and the neutral molecule. This behavior can be understood if we look into chemical bonding of molecules. The metallic ligand is bound with an ionic bound to the XO_4^{n-} ion and the valence electron from ligand is transferred to the ion without significantly perturbing the electronic structure of the ion. Our DFT calculations therefore suggest that the influence of the cation on the $K\beta$ emission spectra shape is almost negligible. Therefore, the main characteristics of the VtC emission spectra can be successfully modelled only with the first coordination sphere around the center atom.

The DFT calculated ground state electronic configuration for the XO_4^{n-} ion is the same for all three elements, including fifty electrons arranged through twelve degenerate orbitals. The structure of the MO reflects the tetrahedral molecular geometry and MO are labeled according to the irreducible representation of the T_d point group. The first five orbitals $1a_1^2$, $2a_1^2$, $1t_2^6$,$3a_1^2$, and $2t_2^6$ correspond to X $1s$, O $1s$, X $2s$, and X $2p$ atomic-like orbitals.

The valence molecular orbitals $4a_1^2$, $3t_2^6$, $5a_1^2$, $4t_2^6$, $1e^4$, $5t_2^6$, and $1t_1^6$ are built from the X $3s$, $3p$ and $3d$ and the O $2s$ and $2p$ atomic orbitals. According to the dipole selection rule, electron transition to the 1s state is allowed only from the orbitals of t_2 symmetry so only these orbitals contribute to the measured $K\beta$ emission spectrum. Based on the structure of valence MOs, three spectral components could be anticipated, corresponding to dipole transition from the $3t_2$, $4t_2$, and $5t_2$ MO, respectively. The electron transitions from $3t_2$ and $4t_2$ correspond to the $K\beta'$ and $K\beta_{1,3}$ main spectral components. The calculated intensities for transitions from $5t_2$ orbitals were found negligible and they do not contribute to the theoretical spectra.

Table 4.7: Ground state electronic configuration of separate XO_4^{n-} ions with T_d local symmetry performed by Mulliken population analysis. For comparison ground state electronic configuration of corresponding neutral molecules is also given. Contribution of particular MO to the corresponding spectral components is noted in the first column.

		PO_4^{3-}					K_3PO_4				
peak	M.O.	P $3s$	P $3p$	P $3d$	O $2s$	O $2p$	P $3s$	P $3p$	P $3d$	O $2s$	O $2p$
	$4a_1$	8	0	0	81	11	8	0	0	79	10
$K\beta'$	$3t_2$	0	7	2	87	4	0	7	2	79	3
	$5a_1$	26	0	0	26	47	27	1	0	26	44
$K\beta_{1,3}$	$4t_2$	0	21	0	7	72	0	24	0	10	64
	$1e$	0	0	4	0	96	0	0	4	0	91
	$5t_2$	0	2	5	0	93	0	9	5	0	89
	$1t_1$	0	0	0	0	100	0	0	0	0	97
		SO_4^{2-}					K_2SO_4				
peak	M.O.	S $3s$	S $3p$	S $3d$	O $2s$	O $2p$	S $3s$	S $3p$	S $3d$	O $2s$	O $2p$
	$4a_1$	26	0	0	60	13	28	0	0	58	12
$K\beta'$	$3t_2$	0	11	2	81	5	0	11	2	81	5
	$5a_1$	24	0	0	46	29	24	0	0	47	27
$K\beta_{1,3}$	$4t_2$	0	27	0	16	56	0	29	0	19	50
	$1e$	0	0	5	0	95	0	0	5	0	93
	$5t_2$	0	8	5	0	87	0	11	5	0	79
	$1t_1$	0	0	0	0	100	0	0	0	0	99
		ClO_4^-					$KClO_4$				
peak	M.O.	Cl $3s$	Cl $3p$	Cl $3d$	O $2s$	O $2p$	Cl $3s$	Cl $3p$	Cl $3d$	O $2s$	O $2p$
	$4a_1$	45	0	0	41	13	45	0	0	40	13
$K\beta'$	$3t_2$	0	18	2	72	8	0	18	2	72	7
	$5a_1$	20	0	0	66	14	19	1	0	63	15
$K\beta_{1,3}$	$4t_2$	0	32	0	26	41	0	31	0	26	41
	$1e$	0	0	5	0	94	0	0	5	0	94
	$5t_2$	0	9	6	0	85	0	9	6	0	84
	$1t_1$	0	0	0	0	100	0	0	0	0	99

In order to interpret valence MO in terms of atomic orbitals, Mulliken population analysis was performed on the calculated ground state of all three (XO_4^{n-}) ions and the corresponding full neutral molecule, and the results are presented in Table 4.7. Our calculations are in good agreement with the orbital composition obtained by Adachi and Taniguchi [115] with discrete variational $X\alpha$ cluster calculation on the same ions. While the structure of the $K\beta$ emission spectrum for all measured (XO_4^{n-}) molecules is practically the same, the $K\beta'/K\beta_{1,3}$ intensity ratio is showing an increasing trend by going from P

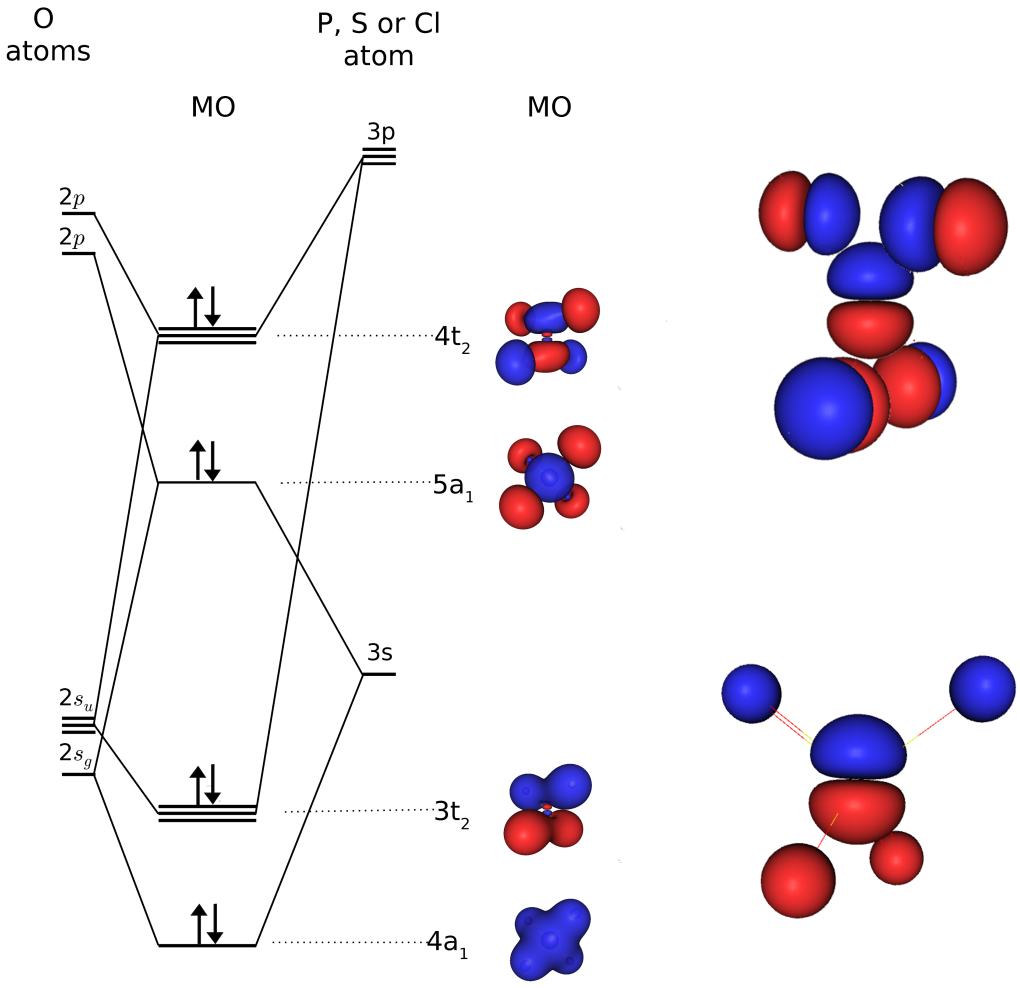


Figure 4.7: (*left*) Qualitative molecular diagram for the XO_4^{n-} ions, only occupied MO contributing to the $K\beta$ emission spectrum are presented. (*center*) The calculated isosurfaces of electron density for corresponding valence MO are plotted. (*right-up* and *right-down*) Construction of the $4t_2$ and $3t_2$ MOs with atomic X $3p$ and O $2s$, $2p$ orbitals is presented.

to Cl. The same behavior of two main peaks is also reproduced by the calculated spectra. The explanation is provided by the Mulliken population analysis, presented in Table 4.7. The ratio of the amount of atomic 3p character in the $3t_2$ and $4t_2$ MO is increasing with increased Z of the central atom in the (XO_4^{n-}) anion resulting in increased intensity ratio of the $K\beta'$ and $K\beta_{1,3}$ peaks. The comparison of the Mulliken population analysis of the XO_4^{n-} ions and the corresponding full neutral molecule have shown very little difference in the calculated ground state electronic configuration confirming further that the cation effect to the electronic structure of the central atom is practically negligible.

Finally, we have schematically constructed also a molecular diagram together with the corresponding $3t_2$ and $4t_2$ molecular orbitals contributing to the $K\beta$ emission spectrum. Despite that such MO diagram is slightly simplified, it can provide a very helpful concept in understanding the molecular valence electronic structure. In a similar way as the formation of in-phase (σ_g) and out-of-phase (σ_u) σ orbitals in a diatomic molecule discussed in Section 2.4, also, the four O $2s$ atomic orbitals in T_d symmetry form two types of orbitals,

one orbital corresponds to the bonding ($2s_g$) with a_1 symmetry and three orbitals are antibonding ($2s_u$) orbitals with t_2 symmetry. Only orbitals with the same symmetry can build molecular orbitals. So, the X $3s$ orbital with the a_1 symmetry together with oxygen ($2s_g$) orbital forms the MOs $4a_1$ and $5a_1$ in the XO_4^{n-} anions. On the other hand, the O ($2s_u$) orbitals with the same symmetry as X $3p$ orbitals form the $3t_2$ and $4t_2$ MO. This is presented schematically in the molecular diagram in Figure 4.7.

Besides the level diagram we can try to construct also the $3t_2$ and $4t_2$ MO corresponding to $K\beta'$ and $K\beta_{1,3}$ spectral components, respectively. The $3t_2$ MO is composed mostly of O $2s$ orbitals, which can be nicely arranged around the X $3p$ atomic orbital along the z axis as shown in Figure 4.7. The $4t_2$ MO is composed mostly of O $2p$ and X $3p$ atomic orbitals. In order to arrange O $2p$ orbitals around X $3p$, we need to expand the picture from s-type orbitals in diatomic molecules also to the p-type orbitals. The p orbitals can form σ- and π-type MOs. The σ_g orbitals are composed of two O $2p$ orbitals along the x axis and another two along the y axis. Together with a perpendicular X 3p orbital along the z axis also the $4t_2$ MO is built and presented schematically in Figure 4.7. This simplified model can be compared to the isosurfaces of our DFT calculated electron density of corresponding MO also presented in Figure 4.7. This comparison shows that the mixing of O $2s$ and $2p$ orbitals changes the electronic structure and leads to different ratios of O $2s$ and $2p$ atomic orbitals. However, the main structure of the calculated orbitals is very similar and such simple formation of molecular orbitals and level diagrams can be successfully used to explain the main components of the $K\beta$ emission spectrum.

4.2.2 Molecular systems with C_{3v} local symmetry

The same approach as for the T_d symmetry has also been applied to the analysis of XO_3^{n-} molecular systems with C_{3v} local symmetry. High-resolution P, S, and Cl $K\beta$ x-ray emission spectra measured from Na_2HPO_3, Na_2SO_3 and $NaClO_3$ compounds are presented in the upper part of Figure 4.8. In case of S and Cl compounds the spectral structure is very similar to each other, exhibiting three main peaks. We kept the same notations as in the case of XO_4^{n-} molecular systems with T_d local symmetry. The two main peaks are labeled as $K\beta'$ and $K\beta_{1,3}$, whereas for two side peaks next to the main $K\beta_{1,3}$ peak the labels $K\beta_x$ and $K\beta''$ are used. For the new peak at higher energies the label $K\beta_{xx}$ is applied. In case of Na_2HPO_3 compound, the $K\beta_{xx}$ component is absent from the spectrum. The measured VtC emission spectra were fitted by a model spectrum composed of several Voigt profiles, also presented in Figure 4.8. The experimental energies and intensities of separate spectral components extracted from the fit are reported in Table 4.8. Compared to the measured spectra of XO_4^{n-} systems two distinct features can be recognized. The first is an additional $K\beta_{xx}$ spectral peak in S and Cl compounds and the second is a decrease of the $K\beta'/K\beta_{1,3}$ intensity ratio for all measured spectra of C_{3v} molecular systems.

Similar analysis as in case of the T_d molecular system, is now applied also to the system in C_{3v} local symmetry. The DFT calculations of the electronic transitions corresponding to the $K\beta$ x-ray emission spectra were performed for the first coordinate sphere around the center atom building the XO_3^{n-} anions and for the neutral molecule. The final theoretical spectra were built from the calculated line spectra using Voigt profiles; the width of the Voigt profiles was adjusted to fit the experimental line widths. Also in this case, an overall shift of the calculated absolute energy scale of a few eV was applied in order to match the experimental energies and the values are given in Table 4.6. The final theoretical spectra for the neutral molecules and the corresponding XO_3^{n-} anions are presented in Figure 4.8. For all three compounds, the theoretical spectra of the neutral molecule are in good agreement with the measured spectra. In case of S and Cl the theoretical spectra of the isolated XO_3^{n-} ion and the neutral molecule are practically the same so the influence of the sodium

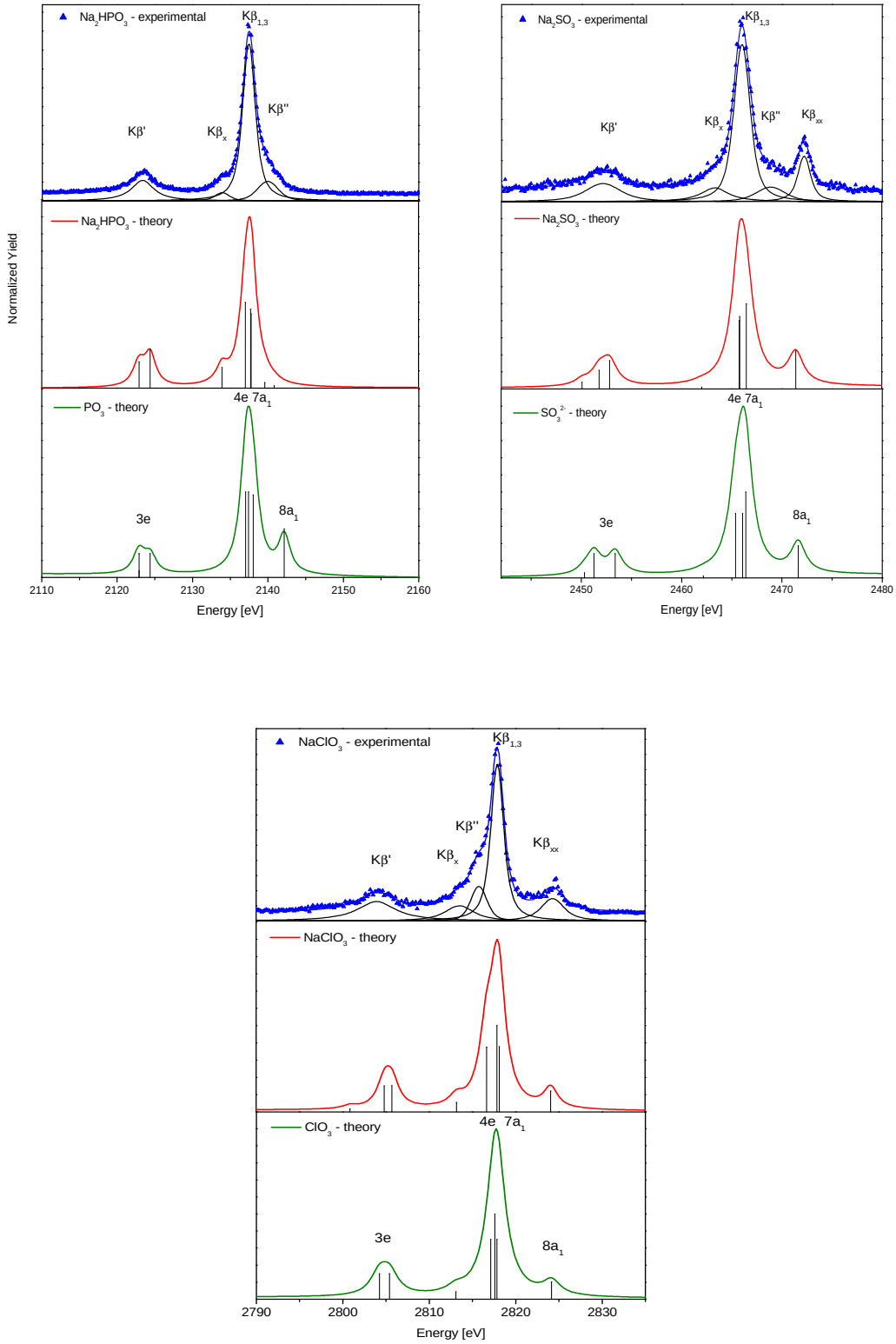


Figure 4.8: Experimental and theoretical $K\beta$ x-ray emission spectra of phosphorus (left), sulfur (center) and chlorine (right) in C_{3v} local symmetry.

Table 4.8: Extracted experimental energies and relative intensities of main spectral components for the Na_2HPO_3, Na_2SO_3 and $NaClO_3$ compounds. The fitting errors are reported in parentheses.

	$K\beta'$	$K\beta_x$	$K\beta_{1,3}$	$K\beta''$	$K\beta_{xx}$	$K\beta'/K\beta_{1,3}$
Na_2HPO_3						
Energy [eV]	2123.33(5)	2133.9(1)	2137.46(1)	2140.11(9)	-	
Intensity [%]	13.6(0.8)	4.2(1.4)	72.2(3.0)	10.0(1.8)	-	0.19(0.01)
Na_2SO_3						
Energy [eV]	2452.13(8)	2463.3(5)	2466.00(1)	2468.9(5)	2472.20(3)	
Intensity [%]	14.2(2.0)	9.6(5.4)	54.2(10.3)	8.9(15.4)	13.0(4.7)	0.26(0.06)
$NaClO_3$						
Energy [eV]	2803.9(1)	2813.4(2.5)	2817.90(4)	2815.7(2)	2824.24(8)	
Intensity [%]	19.7(2.1)	9.8(24.6)	47.2(12.0)	11.2(38.5)	12.0(1.7)	0.42(0.11)

atoms on the electronic structure of sulfite and chlorate is negligible. In case of theoretical spectrum of PO_3^{n-} anion, the additional $K\beta_{xx}$ component appears in the spectrum, similar to the experimental and theoretical spectrum of the S and Cl compounds. When the neutral Na_2HPO_3 molecule is considered in the calculation, the $K\beta_{xx}$ peak disappears from the spectrum in agreement with the experiment. In T_d molecular system and also for Na_2SO_3 and $NaClO_3$ molecules the influence of cation was found negligible, so the difference in the spectrum was addressed to hydrogen bonding to PO_3^{3-} ions. The strong covalent bonding of hydrogen atom directly to P atoms perturbes significantly the electronic structure of the PO_3^{3-} anion.

In order to check the hydrogen influence on the electronic structure of the PO_3^{3-} ion, we have performed geometrical optimization of the neutral Na_2HPO_3 molecule and then increased the distance between the Na_2PO_3 molecular fragment and the hydrogen atom in steps of 0.5Å, while all other atoms were kept at fixed, initial position. For each distance, the calculation in ground state approximation was performed and also for the $Na_2PO_3^-$ molecular fragment. As we have not done the individual optimization for each electronic state, a relatively larger overall shift of the calculated absolute energy scale of 67.4 eV was applied to all theoretical spectra in order to match the experimental energies. Theoretical $K\beta$ x-ray emission spectra are presented in Figure 4.9. The results have clearly shown the decrease of the $K\beta_{xx}$ intensity when the hydrogen atom is approaching its actual position within the Na_2HPO_3 molecule.

The MO of XO_3^{n-} anions are labeled according to the irreducible representation of the C_{3v} point group. The 16 electrons are arranged in the molecular core orbitals $1a_1^2$, $2a_1^2$, $1e^4$, $3a_1^2$, $2e^4$ and $4a_1^2$ which correspond to X $1s$, O $1s$, X $2s$, and X $2p$ atomic-like orbitals, respectively. The DFT calculated valence electronic structure for the PO_3^{3-} and SO_3^{2-} ions is the same and the MO orbitals are arranged in energy in the order $5a_1^2$, $3e^4$, $6a_1^2$, $4e^4$, $7a_1^2$, $5e^4$, $6e^4$, $1a_2^2$ and $8a_1^2$. The calculated valence MO order for the ClO_3^- ion is slightly different: $5a_1^2$, $3e^4$, $6a_1^2$, $7a_1^2$, $4e^4$, $5e^4$, $6e^4$, $8a_1^2$ and $1a_2^2$. The Mulliken population analysis was performed on the calculated ground state of the XO_3^{n-} ions and neutral molecular systems and results are presented in Table 4.9. The differences between ions and neutral molecules for S and Cl compounds are almost negligible and they come from a small contribution of Na orbitals. In case of PO_3^{3-} ions and Na_2HPO_3 molecule the differences in the electronic structure are very large so that it is not possible to assign MO of the Na_2HPO_3 molecule to the $5e$, $6e$, $1a_2$, and $8a_1$ MO of the PO_3^{3-} ions. Their atomic composition and also energy order are significantly different, which confirms the significant effect of the hydrogen atom on the electronic structure of the PO_3^{3-} ion.

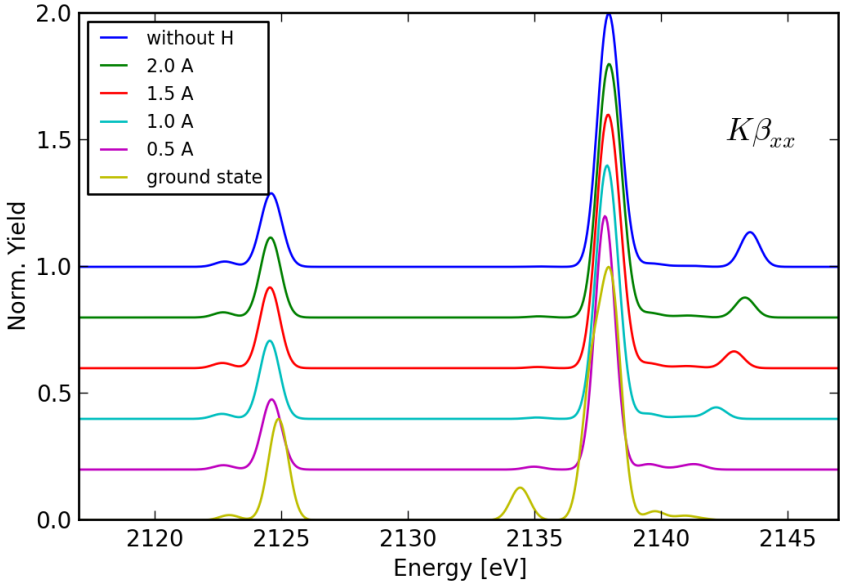


Figure 4.9: Theoretical P $K\beta$ emission spectra of Na_2HPO_3 with different distances between the Na_2PO_3 molecular fragment and the hydrogen atom. The calculated stick spectra were convoluted with 0.9 eV FWHM Gaussian function.

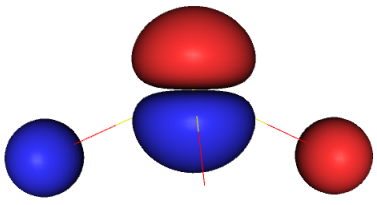


Figure 4.10: Schematic arrangement of X $3p_z$ and O $2s$ orbitals producing zero overlap.

Table 4.9: Ground state electronic configuration of separate XO_3^{n-} ions with C_{3v} local symmetry performed by Mulliken population analysis. For comparison ground state electronic configuration of corresponding neutral molecules is also given. Contributions of particular MO to the corresponding spectral components are noted in the first column.

		PO_3^{3-}					Na_2HPO_3				
peak	M.O.	P 3s	P 3p	P 3d	O 2s	O 2p	P 3s	P 3p	P 3d	O 2s	O 2p
	$5a_1$	13	0	0	81	6	7	1	0	76	9
$K\beta'$	3e	0	8	1	88	3	0	8	2	84	2
	$6a_1$	38	1	0	20	40	34	8	0	19	20
$K\beta_{1,3}$	4e	0	21	0	6	72	0	22	0	12	65
$K\beta_{1,3}$	$7a_1$	2	36	0	2	60	1	33	0	7	44
	5e	0	3	3	0	94	-	-	-	-	-
	6e	0	6	2	0	92	-	-	-	-	-
	$1a_2$	0	0	0	0	100	-	-	-	-	-
$K\beta_{xx}$	$8a_1$	16	19	2	16	47	-	-	-	-	-
		SO_3^{3-}					Na_2SO_3				
peak	M.O.	S 3s	S 3p	S 3d	O 2s	O 2p	S 3s	S 3p	S 3d	O 2s	O 2p
	$5a_1$	29	1	0	61	9	27	1	0	60	9
$K\beta'$	3e	0	11	1	84	4	0	9	2	83	4
	$6a_1$	38	3	0	38	21	40	2	0	37	20
$K\beta_{1,3}$	4e	0	27	0	13	59	0	27	0	13	58
$K\beta_{1,3}$	$7a_1$	2	49	0	3	46	2	44	0	3	41
	5e	0	3	4	0	93	0	1	4	0	91
	6e	0	5	2	0	93	0	5	2	0	92
	$1a_2$	0	0	0	0	100	0	0	0	0	98
$K\beta_{xx}$	$8a_1$	13	11	2	5	69	13	13	0	2	63
		ClO_3^{3-}					$NaClO_3$				
peak	M.O.	Cl 3s	Cl 3p	Cl 3d	O 2s	O 2p	Cl 3s	Cl 3p	Cl 3d	O 2s	O 2p
	$5a_1$	48	1	0	41	9	38	1	0	30	7
$K\beta'$	3e	0	16	2	76	5	0	15	2	76	6
	$6a_1$	32	7	0	55	5	34	8	0	52	6
$K\beta_{1,3}$	$7a_1$	0	60	0	8	31	0	34	0	21	43
$K\beta_{1,3}$	4e	0	33	0	23	44	0	56	0	14	28
	5e	0	3	4	0	93	0	1	4	0	94
	6e	0	5	2	0	93	0	5	2	0	92
	$8a_1$	7	6	3	1	84	6	7	3	0	69
$K\beta_{xx}$	$1a_2$	0	0	0	0	100	0	0	0	0	100

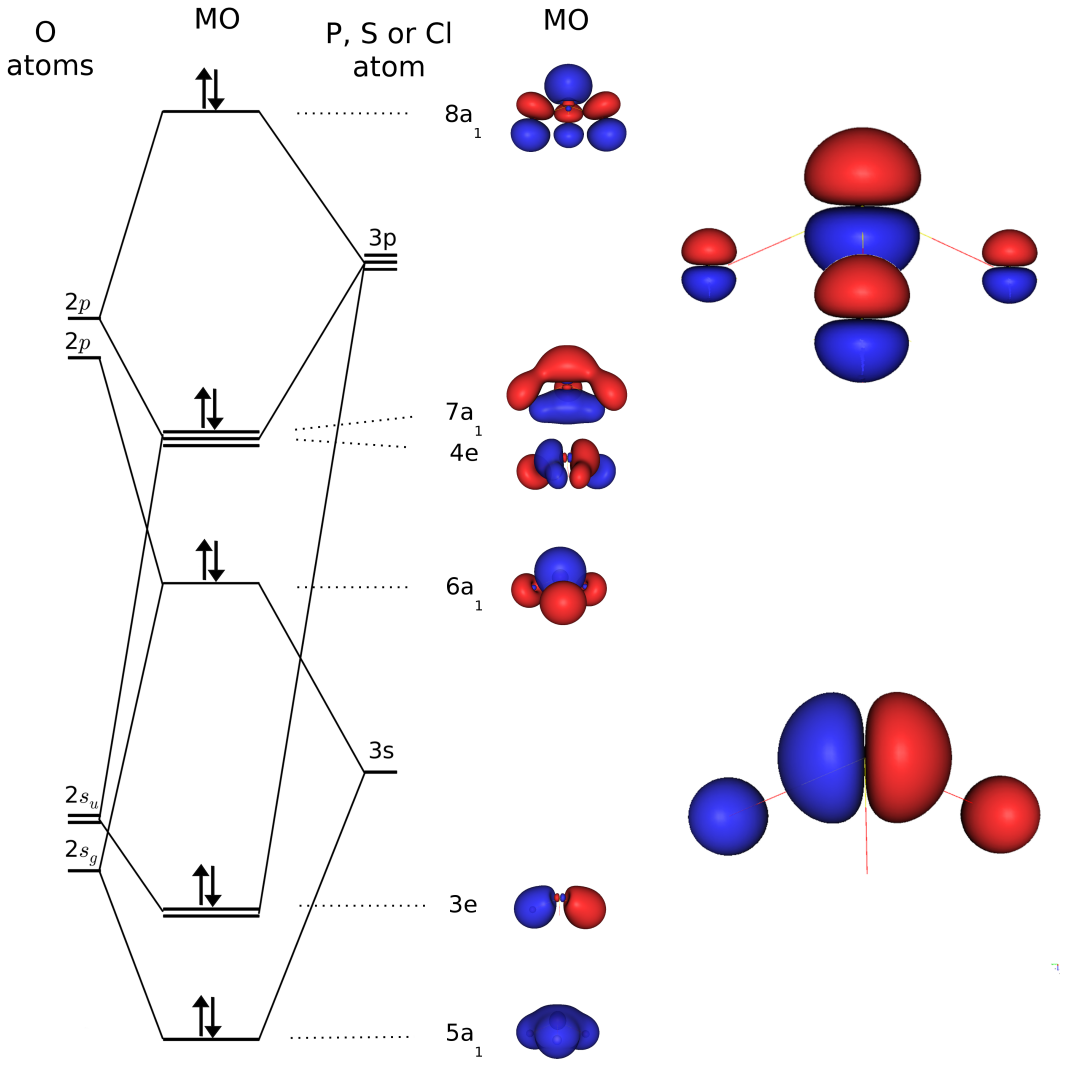


Figure 4.11: (*left*) Qualitative molecular diagram for the XO_3^{n-} ions, only occupied MO contributing to the spectrum are presented. (*center*) The calculated isosurfaces of electron density for corresponding valence MO are plotted. (*right*) The schematic presentation of the $3e$ and $7a_1$ MO.

In the molecular system with C_{3v} local symmetry, electron dipole transitions to the $1s$ state are allowed from the MO with a_1 and e symmetry. The $K\beta'$ spectral component is addressed to the electron transition from the $3e$ MO. The atomic orbital composition of $3e$ MO is similar to the $3t_2$ MO in T_d molecular system, only the number of MO which contribute to the $K\beta'$ peak is reduced from three to two. It is important to note that in T_d local symmetry all four O $2s$ orbitals contribute equally to the $3t_2$ MO, whereas in case of C_{3v} symmetry the O $2s$ contribution is not equal for each of degenerate $3e$ sets. The reduction of the MO is explained by the geometrical structure of the molecule. In the case of the T_d molecular system all Cartesian axes are equivalent and X $3p$-orbitals have two O 2s orbitals on the top and two on the bottom side, as it is presented in Figure 4.7. The geometrical structure of the C_{3v} molecular system is slightly different, the center atom is much closer to the oxygen plane. Consequently, the overlap integral between the O $2s$ and X $3p_z$ is negligible and the X $3p_z$ which is perpendicular to the oxygen plane and O $2s$ orbitals cannot build a valence-type molecular orbitals. The schematic arrangement of X $3p_z$ and O $2s$ is presented in Figure 4.10.

On the other hand, the X $3p_{x,y}$ orbitals form two 3e MO with the oxygen $2s$ orbitals in the same way as in T_d symmetry. The result is that the character of the $K\beta'$ spectral line in C_{3v} symmetry is similar as for the system of T_d symmetry, while the reduction of MOs contributing to the $K\beta'$ component results in the decrease of the $K\beta'$ relative intensity. The electron transitions from the $4e$ and $7a_1$ MO contribute to the $K\beta_{1,3}$ peak. The atomic orbital composition given by the Mulliken population analysis is for the $4e$ MO similar as for the $4t_2$ MO in T_d symmetry and they are built in the same way as $4t_2$ MO in the tetrahedral symmetry. The X $3p_{x,y}$ orbitals and O $2p$ constructs the two $4e$ MO in XO_3^{n-} anions. Again, the geometry of the molecule defines the interaction between orbitals. The X $3p_z$ orbital cannot interact with O $2p$ orbitals in the same way as was in the T_d symmetry and the overlap integral between X $3p_z$ and O $2p_{x,y}$ is zero. However, the X $3p_z$ interact with the O $2p_z$ orbitals to form a π-type bond. The symmetry of the X $3p_z$ orbital is a_1, so also the O $2p_z$ orbitals need to be arranged in the a_1 symmetry. The schematic arrangement of $7a_1$ MO is presented in the upper-right part in Figure 4.11. The $7a_1$ corresponds to the π-bonding orbital and contributes to the $K\beta_{1,3}$ spectral component. The π-antibonding MO corresponds to $8a_1$ orbital with a slightly higher energy and the electron transitions from this $8a_1$ orbital correspond to the additional peak $K\beta_{xx}$ on the high energy side of the main $K\beta_{1,3}$ peak.

4.2.3 Molecular systems with C_{2v} local symmetry

We can reduce the symmetry further and perform a similar analysis also for C_2v molecular systems. Among measured compounds only the $CaH_4O_4P_2$ exhibit the C_{2v} symmetry. In this compound both P atoms are surrounded with two H atoms and two O atoms. Experimental P $K\beta$ emission spectrum is presented in the top part of Figure 4.12 and the spectrum shape is similar as in the case of the Na_2HPO_3 compound. The two main peaks $K\beta'$ and $K\beta_{1,3}$ and two side peaks $K\beta_x$ and $K\beta''$ are labeled as before. The experimental energies and relative intensities of each spectral component are extracted by a fitting procedure and tabulated in Table 4.10. An observed decrease of the $K\beta'/K\beta_{1,3}$ intensity ratio by going from T_d to C_{3v} molecular system is now extended also to C_{2v} symmetry.

The DFT calculations of the first coordinate sphere around the P atom were again performed to interpret the measured spectrum. The final theoretical spectrum was built from the calculated stick spectrum using Voigt profiles in the same way as before. With the exception of the $K\beta''$ spectral component the theoretical model spectrum very well reproduced the experimental one and the main components can be properly assigned. The 34 electrons of the $H_2PO_2^-$ ion are arranged through the MOs which are labeled

Table 4.10: Experimental energies and intensities of the main spectral components for $CaH_4O_4P_2$ together with the average atomic character of the group of transitions building the model spectra.

	$K\beta'$	$K\beta_x$	$K\beta_{1,3}$	$K\beta''$
$H_2PO_2^{1-}$				
Energy [eV]	2122.87(7)	2132.7(1)	2137.22(1)	2140.59(5)
Intensity [a.u.]	12.3(0.8)	3.0(0.9)	72.2(1.5)	12.4(1.0)
AO orbital population[%]	P3p 12	P3p 10	P3p 29	-
	P3d 2	P3s 40	O2s 8	
	O2s 81	O2s 15	O2p 46	
	O2p 4	O2p 6	H1s 15	
		H1s 27		

Table 4.11: Ground state electronic configuration of separate SO_2 and ClO_2^+ molecule obtained by Mulliken population analysis. Contribution of particular MO to the corresponding spectral components are noted in the first column.

		SO_2					ClO_2^+				
peak	M.O.	S 3s	S 3p	S 3d	O 2s	O 2p	Cl3s	Cl3p	Cl3d	O 2s	O 2p
	$5a_1$	27	3	1	59	9	43	3	1	43	10
$K\beta'$	$3b_1$	0	14	2	78	6	0	17	2	72	8
	$6a_1$	46	3	0	35	14	42	7	0	47	3
$K\beta_{1,3}$	$2b_2$	0	51	0	0	47	0	67	0	0	32
$K\beta_{1,3}$	$4b_1$	0	20	0	19	61	0	23	0	27	48
$K\beta_{1,3}$	$7a_1$	3	41	1	5	50	1	50	0	10	37
	$1a_2$	0	0	4	0	96	0	0	4	0	96
	$5b_1$	0	6	3	0	91	0	5	3	0	92
$K\beta_{xx}$	$8a_1$	14	7	5	1	71	43	3	1	43	10

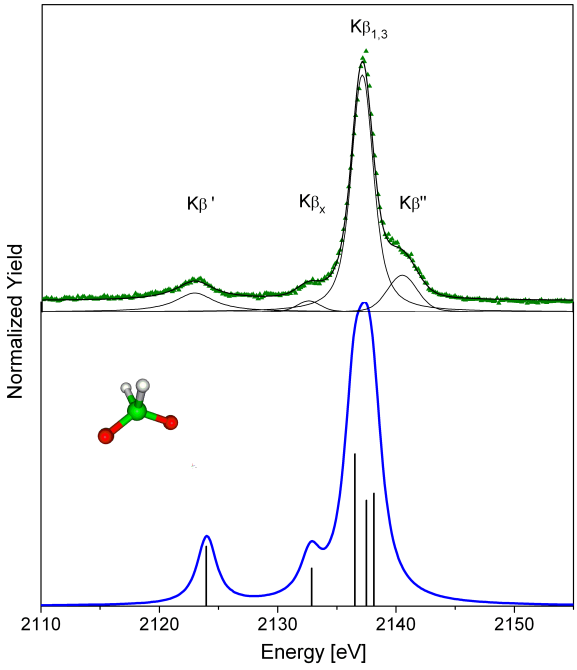


Figure 4.12: Experimental *(green)* P $K\beta$ emission spectrum of $CaH_4O_4P_2$ compared to the theoretical model *(blue)* calculated for the $H_2PO_2^{1-}$ ion.

according to the irreducible representation of C_{2v} point group: $1a_1^2$, $2a_1^2$, $1b_1^2$, $3a_1^2$, $1b_2^2$, $4a_1^2$, $2b_1^2$, $5a_1^2$, $3b_1^2$, $6a_1^2$, $2b_2^2$, $7a_1^2$, $4b_1^2$, $8a_1^2$, $1a_2^2$, and $5b_1^2$. On the calculated ground state the Mulliken population analysis of MO was performed and the results are tabulated in Table 4.10. Within the dipole selection rule transitions from MO of a_2 symmetry to the $1s$ state are forbidden and all other valence MO can contribute to the $K\beta$ emission spectrum. The electron transitions from the $3b_1$ MO contribute to the $K\beta'$ peak and the atomic composition is similar as for the $3t_2$ MO in case of T_d and for the $3e$ MO in case of C_{3v} molecular systems. The reason for this further reduction of MO number is the geometry of the $H_2PO_2^-$ ion. Only one P $3p$ orbital directed in line with oxygen atoms can interact with O $2s$ orbitals. Another two P $3p$ orbitals have zero overall integral with O $2s$. In case of the $K\beta_{1,3}$ spectral component three MO $2b_2$, $7a_1$, and $4b_1$ contribute to the spectrum. The average atomic composition of this three MO is similar as in case of $4t_2$ MO in T_d symmetry, but with additional contribution of H $1s$ orbital.

In case of S and Cl elements in C_{2v} local symmetry only theoretical spectra will be discussed. For the SO_2 and ClO_2^+ molecular systems DFT calculations were performed and the theoretical model spectra are presented in Figure 4.13. The calculations were performed in the ground state approximation without separate optimization of the initial and final state. The DFT calculated emission spectra were shifted for 77 and 85 eV in case of S and Cl compounds, respectively. The results of Mulliken population analysis performed on the ground state of the molecule are tabulated in Table 4.11 together with the corresponding labels of the main spectral components. Similar as for $H_2PO_2^-$ ion only one MO contributes to the $K\beta'$ component. Therefore, for all three elements the intensity ratio $K\beta'/K\beta_{1,3}$ decreases going from higher T_d to lower C_{2v} local symmetry and this behavior is correlated with the numbers of MO which contribute to the $K\beta'$ spectral

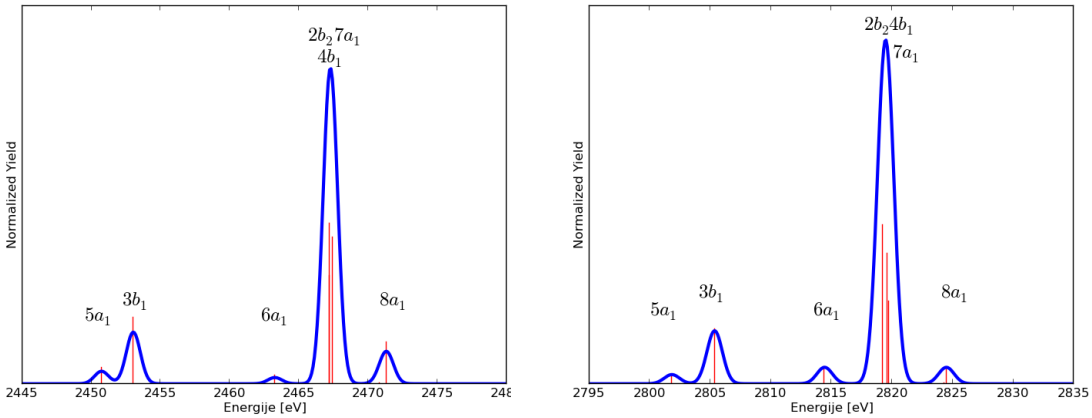


Figure 4.13: Theoretical spectra of (left) SO_2 and (right) ClO_2^+ molecule. The calculated stick spectra were convoluted with the Gaussian function.

component. The atomic character of $2b_2$, $4b_1$, and $7a_1$ MO differs slightly. However, the atomic character of $2b_2$ and $4b_1$ MO is similar to the character of $4e$ MO in the C_{3v} molecular system so they can be addressed to this type of MO. The atomic composition of $7a_1$ and $8a_1$ in C_{2v} symmetry is similar to the $7a_1$ and $8a_1$ in C_{3v} molecular systems. These two MO are built like π-bonding and π-antibonding in a similar way as in the C_{3v} local symmetry. The electronic structure of the molecular system with C_{3v} and C_{2v} is therefore very similar. The absence of the $K\beta_{xx}$ peak in the spectrum of $H_2PO_2^-$ ion can be addressed to hydrogen bonding in the same way as in the case of the Na_2HPO_3 molecule.

4.3 The Influence of Hydrogen Atoms Breaking the T_d Symmetry of the Phosphate Group

So far we have restricted our analysis on the first coordinate sphere around the central atom and the main spectral features were described with this approach. Now we would like to discuss effects of the second coordinate sphere to the $K\beta$ x-ray emission spectra, in particular the effect of hydrogen atoms bound to the phosphate ion. For this purpose three different phosphate compounds are selected and their experimental $K\beta$ emission spectra are shown in Figure 4.15. All measured phosphorus spectra exhibit four main components which were labeled as before: $K\beta_{1,3}$, $K\beta'$, $K\beta_x$, and $K\beta''$. In our previous discussion about the molecular systems in T_d symmetry the influence of the metallic cation on the measured $K\beta$ emission spectra was found practically negligible. In case of hydrogen atoms bound to the phosphate ion the characteristic structure composed of main $K\beta_{1,3}$ and $K\beta'$ peaks still remains the same, however, the intensity of the $K\beta_x$, and $K\beta''$ side peaks clearly increases with additional hydrogen atoms bound to the PO_4^{3-} ion.

In order to understand the influence of additional hydrogen atoms bound to the phosphate ion, DFT calculations of the electronic transitions corresponding to the phosphate $K\beta$ x-ray emission spectrum were performed. The theoretical spectra were built from the calculated stick spectrum using Voigt profiles. The Gaussian width was fixed to 0.42 eV corresponding to experimental broadening extracted from the fitting procedure of P $K\alpha$ line. In order to experimentally describe the observed linewidths, the Lorentzian width was increased with respect to the natural lifetime broadening to $\sim$ 1.9 eV. An overall shift of the absolute energy scale of slightly less than -5 eV was applied to theoretical spectra

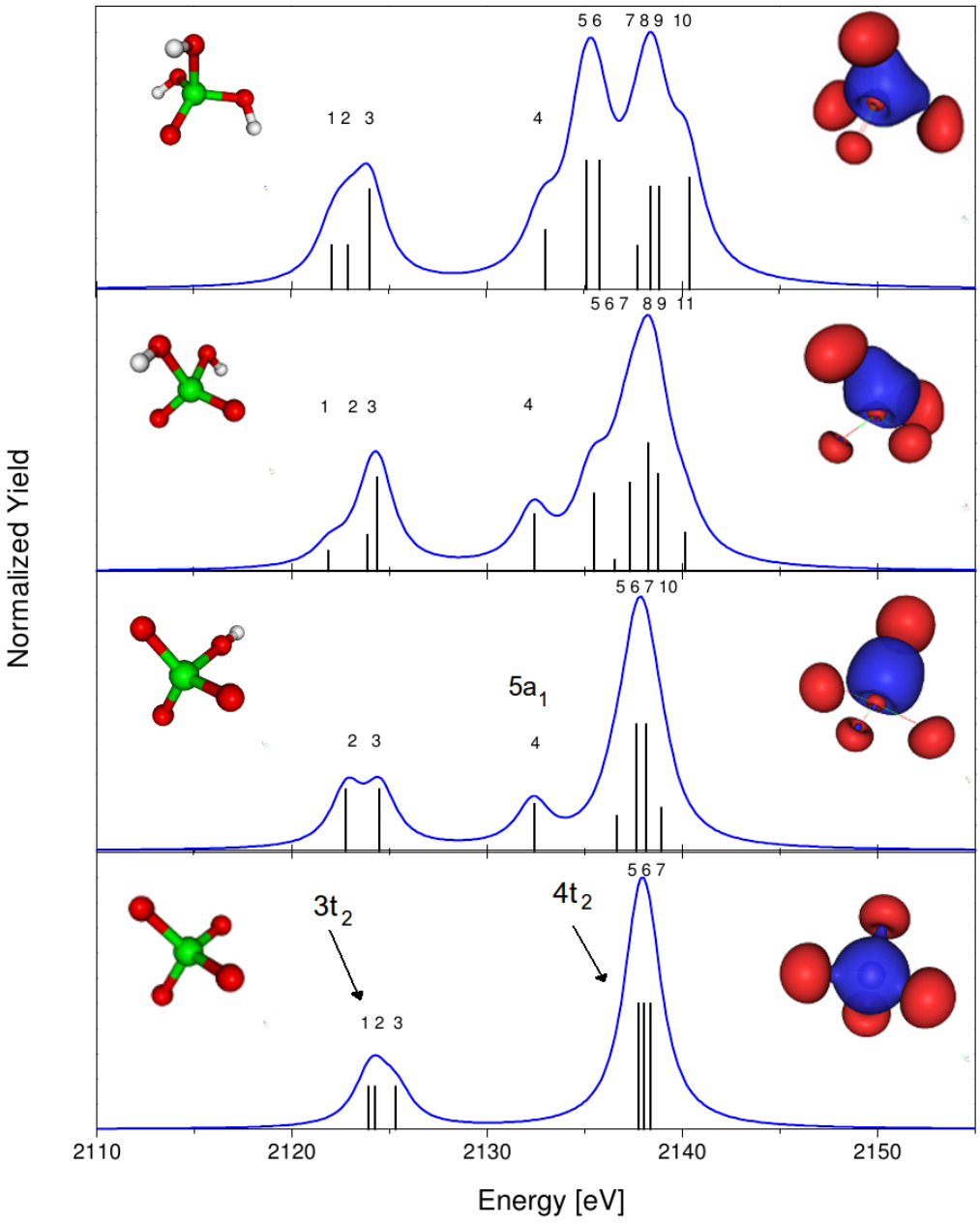


Figure 4.14: Theoretical spectra of (from bottom to top) PO_4^{3-}, HPO_4^{2-}, $H_2PO_4^{1-}$ and H_3PO_4 phosphate ions. Geometrical structure of the molecule is presented on the left with green, red and white representing the P, O and H atoms, respectively. The development of the $4th$ ($5a_1$) orbital building, the $K\beta'$ peak is presented on the right side. The red and blue color represent the negative and positive values of the wavefunction.

Table 4.12: Atomic orbital contributions to the molecular orbitals in PO_4^{3-}, HPO_4^{2-}, $H_2PO_4^{1-}$ and H_3PO_4 used to build the model spectra. The $1t_1$ and $4a_1$ orbitals are omitted since they do not contribute to the spectra.

MO		AO orbital population [%]						AO orbital population [%]					
		P3s	P3p	P3d	O2s	O2p	H1s	P3s	P3p	P3d	O2s	O2p	H1s
		PO_4^{3-}						HPO_4^{2-}					
1	$3t_2$	-	7	2	87	4	-	1	4	-	85	10	-
2	$3t_2$	-	7	2	87	4	-	-	9	1	85	4	-
3	$3t_2$	-	7	2	87	4	-	-	9	2	85	4	-
4	$5a_1$	26	-	-	26	47	-	10	9	1	10	53	17
5	$4t_2$	-	21	-	7	72	-	16	7	-	21	52	4
6	$4t_2$	-	21	-	7	72	-	-	20	-	10	70	-
7	$4t_2$	-	21	-	7	72	-	-	20	-	10	70	-
8	1e	-	-	4	-	96	-	-	-	2	-	97	1
9	1e	-	-	4	-	96	-	-	-	2	-	97	1
10	$5t_2$	-	2	5	-	93	-	-	18	2	-	75	5
11	$5t_2$	-	2	5	-	93	-	-	6	6	-	88	0
12	$5t_2$	-	2	5	-	93	-	-	6	6	-	88	0
		$H_2PO_4^{1-}$						H_3PO_4					
1		-	4	1	87	7	1	-	5	1	87	6	1
2		5	5	2	79	7	1	-	5	1	87	5	1
3		-	10	2	83	4	-	3	7	1	81	6	1
4		13	7	-	6	58	15	18	3	-	6	59	13
5		-	10	1	1	68	18	-	12	2	-	67	18
6		14	2	-	23	53	6	-	12	2	-	67	18
7		-	16	-	11	62	8	11	8	-	21	54	4
8		-	18	-	10	70	-	-	15	-	12	65	5
9		1	11	1	9	76	-	-	15	-	12	65	5
10		-	-	3	-	94	2	-	10	2	8	78	1
11		-	5	3	-	90	-	-	4	4	1	90	-
12		-	13	5	-	81	-	-	4	4	1	90	-

in order to match the experimental energies. As a starting point, the theoretical spectrum of the PO_4^{3-} ion is presented in the bottom part of Figure 4.14. As already explained the $K\beta'$ and $K\beta_{1,3}$ spectrum components are addressed to transitions from the $3t_2$ and $4t_2$ MO. The atomic character of each separate molecular orbital contributing to the model spectrum obtained by the Mulliken population analysis is given in 4.12.

In order to explain also both side peaks $K\beta_x$ and $K\beta''$ and its dependence on the number of hydrogen atoms bound to PO_4^{3-} ion observed in experimental spectra we have expanded the calculations to include also the next coordination shell. With additional hydrogen atoms bound to PO_4^{3-} ion the original tetrahedral T_d symmetry is broken leading to different mixing of the atomic orbitals and changing the dipole transition matrix elements that contribute to the spectrum. In principle one cannot label the orbitals according to the irreducible representations of the T_d point group any more but in order to keep the same number of electrons and follow each orbital only additional protons were actually introduced in our theoretical model and consequently the same labels were used. By adding additional protons the theoretical spectrum starts to develop both side peaks which also grow in intensity with an increasing number of hydrogens in agreement with experimental

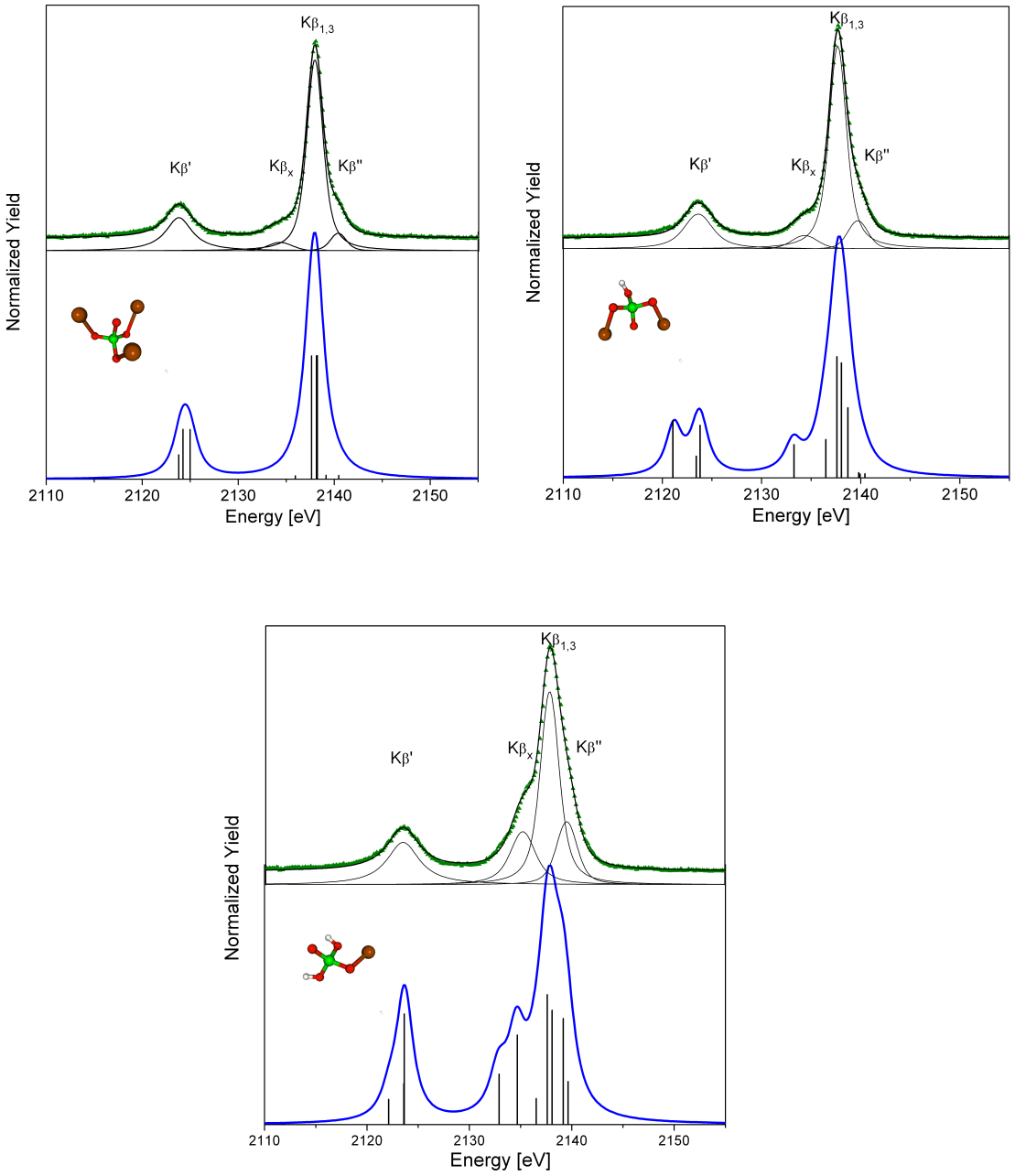


Figure 4.15: Experimental P $K\beta$ emission spectra of *(left)* K_3PO_4, *(right)* Na_2HPO_4 and *(botton)* NaH_2PO_4 compared to theoretical model spectra *(blue)*.

observation.

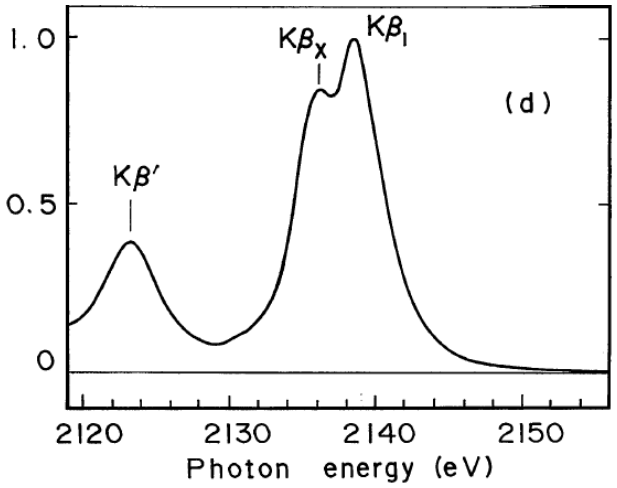


Figure 4.16: P $K\beta$ emission spectrum of H_3PO_4 measured by Sugiura [47].

In tetrahedral symmetry the electron dipole transition from the $5a_1$ MO to atomic-like $1s$ orbital is forbidden. However, the $K\beta_x$ contribution on the low energy tail of the main $K\beta_{1,3}$ peak is explained as a transition from the $5a_1$ MO which changes its atomic character yielding a significant amount of P $3p$ contribution. In a similar way also $K\beta''$ contribution on the high energy side of the main $K\beta_{1,3}$ peak is explained as a transition from $1e$ orbital which also changes its atomic character with a large amount of P $3p$ contribution. In addition also the intensity of transitions from $5t_2$ orbitals is increased compared to the PO_4^{3-} ion. So our calculations qualitatively reproduce the measured phosphate spectra and also explain the increasing intensity of $K\beta_x$ and $K\beta''$ side peaks depending on the number of hydrogens bound to the PO_4^{3-} ion. We have not recorded the H_3PO_4 spectrum but our calculations reproduce very well the spectrum measured by Sugiura [47], presented in Figure 4.16.

Finally, the theoretical model spectra for three typical measured phosphates taking into account a full molecule are presented in Figure 4.15 and compared to the experimental spectra. In order to extract energies and relative intensities of the main spectral components the model spectrum built from four Voigt profiles was fitted to experimental spectra, and the fitted spectra are also shown in Figure 4.15. The extracted values are tabulated in Table 4.13 together with the atomic character of each spectral contribution. This character was obtained by performing Mulliken analysis and averaging the atomic characters of separate molecular orbitals contributing to the particular spectral component. As already discussed before, the influence of the cation on the K_3PO_4 spectrum profile is almost negligible and the experimental spectrum is reproduced by the PO_4^{3-} model. Because of ionic bonding with potassium, a valence electron is transferred to the phosphate ion resulting in an almost pure PO_4^{3-} spectrum. On the other hand, large effects of hydrogen atoms bound covalently to the phosphate ion are observed. In case of covalent bonding with hydrogen, the electron is shared with the phosphate perturbing significantly the structure of valence molecular orbitals contributing to the $K\beta$ emission spectrum.

4.4 Electronic Structure of Sodium Metabisulfite

In this section we would like to extend our analysis of small basic molecular systems with well defined symmetries also to a bit larger molecule and for this purpose the sodium

Table 4.13: Experimental energies and intensities of the main spectral components for the phosphate group along with the average atomic character of the group of transitions building the model spectra. The error estimates from the fit are given in parentheses.

	$K\beta'$	$K\beta_x$	$K\beta_{1,3}$	$K\beta''$
K_3PO_4				
Energy [eV]	2123.75(2)	2134.4(2)	2138.03(1)	2140.45(6)
Intensity [a.u.]	23.1(0.5)	3.8(1.0)	67.4(2.3)	5.7(1.2)
AO orbital population[%]	P3p 7 P3d 2 O2s 79 O2p 3 K3p 9	P3p 1 P3s 27 O2s 26 O2p 44	P3p 24 O2s 10 O2p 64	P3p 1 P3d 3 O2p 90 K3s 4
Na_2HPO_4				
Energy [eV]	2123.61(2)	2134.5(2)	2137.80(1)	2139.82(8)
Intensity [a.u.]	19.9(0.5)	5.5(1.3)	65.7(3.4)	8.9(1.9)
AO orbital population[%]	P3p 6 P3s 1 P3d 1 O2s 84 O2p 5	P3p 6 P3s 14 O2s 15 O2p 54 H1s 9	P3p 19 O2s 10 O2p 66 H1s 1	P3p 5 P3d 4 O2p 86 Na2p 3
NaH_2PO_4				
Energy [eV]	2123.40(2)	2135.27(1)	2137.90(4)	2139.5(1)
Intensity [a.u.]	20.7(0.5)	17.7(3.5)	46.0(7.9)	15.6(4.2)
AO orbital population[%]	P3p 5 P3s 2 O2s 84 O2p 5 H1s 1	P3p 8 P3s 8 O2s 9 O2p 62 H1s 11	P3p 15 O2s 10 O2p 70 H1s 2	P3p 5 O2s 4 O2p 89
KH_2PO_4				
Energy [eV]	2123.50(2)	2135.4(1)	2138.00(4)	2139.4(5)
Intensity [a.u.]	21.1(0.5)	14.9(4.0)	48.1(11.4)	15.9(7.9)
AO orbital population[%]	P3p 5 P3s 1 O2s 83 O2p 5 H1s 1	P3p 8 P3s 8 O2s 9 O2p 61 H1s 11	P3p 15 O2s 9 O2p 69 H1s 2	P3p 4 P3d 2 O2p 90 H1s 1

metabisulfite ($Na_2S_2O_5$) is chosen. The measured S $K\beta$ x-ray emission spectrum is shown in the top part of Figure 4.17. It exhibits five spectral components which were labeled in the same way as before for measured S $K\beta$ x-ray emission spectra of Na_2SO_3 compound. The experimental energies and intensities of separate spectral components extracted from the fit are tabulated in Table 4.14.

In order to build the theoretical spectrum, DFT calculations of the corresponding electronic transitions were performed for the neutral molecule. First the geometry optimization of the molecule was performed and the calculated positions were found in good agreement with the published crystal structure of sodium metabisulfite [116]. Two separate calculations for both S atoms were performed in the ground state approximation without energy corrections and then summed together to reach the final result. An overall shift was applied to the absolute calculated energy scale in order to match the experimental ones. The theoretical spectrum was built from the calculated stick spectra broadened by the Voigt profile in order to fit the experimental linewidths and is also presented together with the experimental spectrum in Figure 4.17. The green and red bars represent the components calculated for sulfur atom surrounded by two (SO_2) and three (SO_3) oxygen atoms, respectively. The theoretical spectrum is in very good agreement with the experimental one.

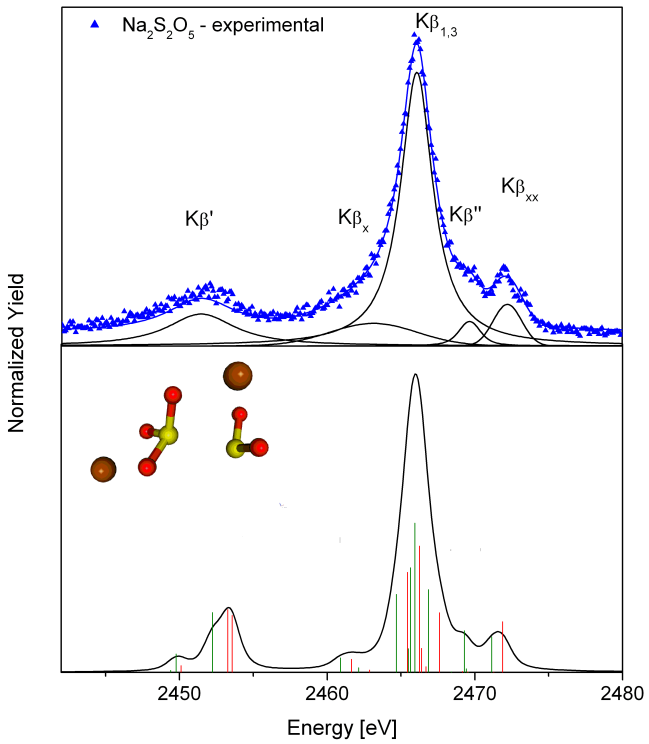


Figure 4.17: (*top*) The experimental and (*bottom*) the theoretical S $K\beta$ emission spectrum of the $Na_2S_2O_5$ molecule, with the model of $Na_2S_2O_5$ molecule, where yellow, red, and brown represent S, O, and Na atoms, respectively.

In previous analyses of the XO_3 and XO_4 systems the influence of metallic cations to the emission spectra was found negligible. In addition, a relatively large distance between the two sulfur atoms 2.2172(11) [116] Å allows us to interpret the spectrum structure with

the help of SO_2 and SO_3 building blocks. The calculated emission spectrum of the SO_3 block within the full $Na_2S_2O_5$ molecule (red bars) basically has the same shape as already discussed in the previous section. Two MOs contributing to the $K\beta'$ component are built by the S $3p_{x,y}$ orbital interacting with the O $2s$ orbitals. The contribution in the $K\beta_{xx}$ component is due to the formation of an "π-antibonding" MO between S $3p_z$ and O $2p_z$ orbitals. In case of calculated emission spectrum of the SO_2 block (green bars) only one of the S $3p$ orbitals interacts with the O $2s$ to form the single MO contributing to the $K\beta'$ spectral component. Two components on the high energy side of the main $K\beta_{1,3}$ peak are due to the formation of MO between S $3p$ and O $2p$ orbitals as was discussed in the previous section. While originally three MO contributions built from S $3p$ and O $2p$ orbitals are found in the main $K\beta_{1,3}$ peak for each isolated block, several additional components are observed in the calculated $Na_2S_2O_5$ spectrum. However, this is not due to the changed electronic structure of the SO_2 and SO_3 building blocks. Within the neutral molecule new additional MO orbitals are being formed as a linear combination of MOs from SO_2 and SO_3 contributing to the $K\beta_{1,3}$ spectral component for both S atoms. This is confirmed by the results of Mulliken population analysis performed on the ground state of the molecule, which is presented in Table 4.14. Besides the main spectral components interpreted as a sum of the SO_2 and SO_3 contributions two additional minor spectral components are observed in the theoretical spectrum on the low energy side of the main $K\beta'$ and $K\beta_{1,3}$ components. The Mulliken population analysis of the MO contributing to these components reveals atomic character similar to the $4a_1$ and $5a_1$ orbitals for the XO_4 system in the T_d symmetry. In a molecular system with pure T_d symmetry electron transition from orbitals of a_1 symmetry to $1s$ atomic orbital are dipole forbidden. However, in a neutral molecule the atoms of a second coordinate sphere modify slightly the character of the a_1 MO and electron transitions to $1s$ are no longer forbidden resulting in these small additional spectral contributions.

Table 4.14: Experimental energies and intensities of the spectral components together with the average atomic character of the group of transitions building the $Na_2S_2O_5$ model spectrum. The error estimates from the fit are given in parentheses.

	$K\beta'$	$K\beta_x$	$K\beta_{1,3}$	$K\beta''$	$K\beta_{xx}$
$Na_2S_2O_5$					
Energy [eV]	2451.4(1)	2463.1(2.5)	2466.06(1)	2469.6(1)	2472.21(9)
Intensity [a.u.]	15.89(1)	9.8(9.9)	65.3(14.8)	3.3(2.7)	5.7(1.7)
Character of the MO [%]	S 3p 11 S 3d 3 O 2s 80 O 2p 5	S 3s 43 S 3p 6 O 2s 35 O 2p 15	S 3s 1 S 3p 34 O 2s 10 O 2p 54	S 3s 10 S 3p 6 S 3d 4 O 2s 2 O 2p 73 Na 2s 4	S 3s 10 S 3p 19 S 3d 3 O 2p 63 Na 2s 3

4.5 X-ray Emission Spectroscopy as a Possible Analytical Tool for Sulfur Speciation in Li-S Batteries

X-ray emission spectroscopy can be applied to characterize the electronic structure of third-row elements in different system in chemistry, biology, geology, and others. One such very interesting and important example are the lithium-sulfur (Li-S) batteries, which

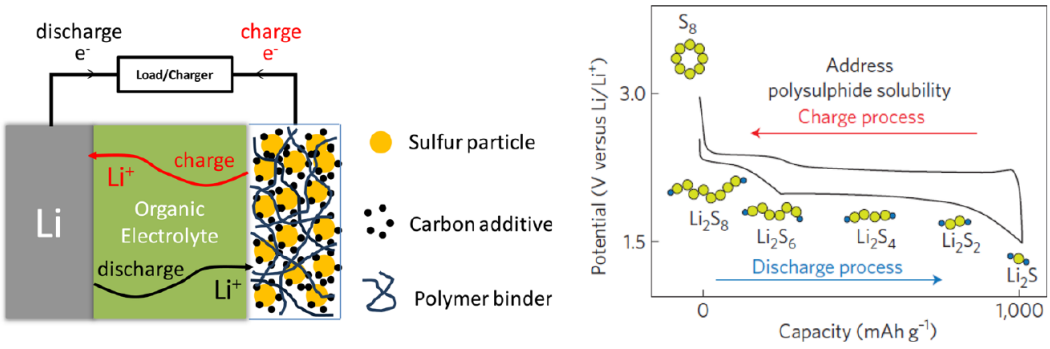


Figure 4.18: (*left*) Schematical picture of a Li-S battery cell. (*right*) Voltage profiles of Li-S battery. During discharge sulfur is reduced by Li to reach the final discharge product Li_2S [28].

are currently considered as one of the most promising candidates for next generation batteries in applications where high energy density is required. This is primarily due to a largely increased theoretical gravimetric capacity compared to those of Li-ion systems. In addition, sulfur is one of the most abundant elements in Earth's crust and relatively inexpensive, which reduces the cost factor [28]. A Li-S battery is composed of a lithium metal anode and a sulfur-based cathode, separated by a porous separator wetted with the electrolyte, which is presented in Figure 4.18. In general, the reaction in the Li-S battery is known, the elemental sulfur (crystalline α-S_8) from the cathode is reduced to lithium sulfide (Li_2S) according to $S_8 + 16\ Li^+ + 16e^- \rightarrow 8Li_2S$. In reality, the process goes through a series of stepwise redox reactions forming various long-chain highly soluble lithium polysulfides (Li_2S_x; x=2-8). Large complexity of the sulfur mechanism during the battery discharge/charge has so far prevented reaching a full reversible theoretical capacity.

Our understanding of the reaction mechanisms occurring within the Li-S battery cell during discharge relies on the application and development of different (preferably in-situ) analytical tools and inner shell x-ray spectroscopy is among the most promising techniques. Among different phases in the Li-S system only elemental sulfur and fully reduced Li_2S are crystalline phases, which limits the application of long-range order techniques such as x-ray diffraction. So far, operando XAS spectroscopy, which has the capability to detect also the amorphous polysulfide phase, was predominantly used for this purpose [117]. Detailed *ab-initio* quantum chemical calculation of the S K absorption edge was performed [118] to interpret the measured spectral features. Recently, also resonant inelastic x-ray scattering (RIXS) measurements were performed on the Li-S battery *in operando* mode to determine relative amounts of each sulfur compounds during the discharge [119]. However, the full discharge mechanism is still not fully understood and additional complementary analytical techniques which could provide accurate quantitative information on the mechanisms of the lithium polysulfide formation should be applied. Here, we would like to explore the capabilities of x-ray emission spectroscopy to address the electrochemical processes in Li-S battery.

We will start with the sulfur $K\alpha$ emission spectra. As already discussed, the $K\alpha$ emission spectrum exhibits an atomic-like doublet structure and small energy shits are recorded reflecting the effective electronic charge of the sulfur atom. In the discharge process the elemental α-S_8 with oxidation state 0 is reduced to the Li_2S compound with S in oxidation state 2−. According to the result of our study (Table 4.1) the $K\alpha$ energy shift between these two sulfur phases is ~ 0.2 eV. For the intermediate Li polysulfide the

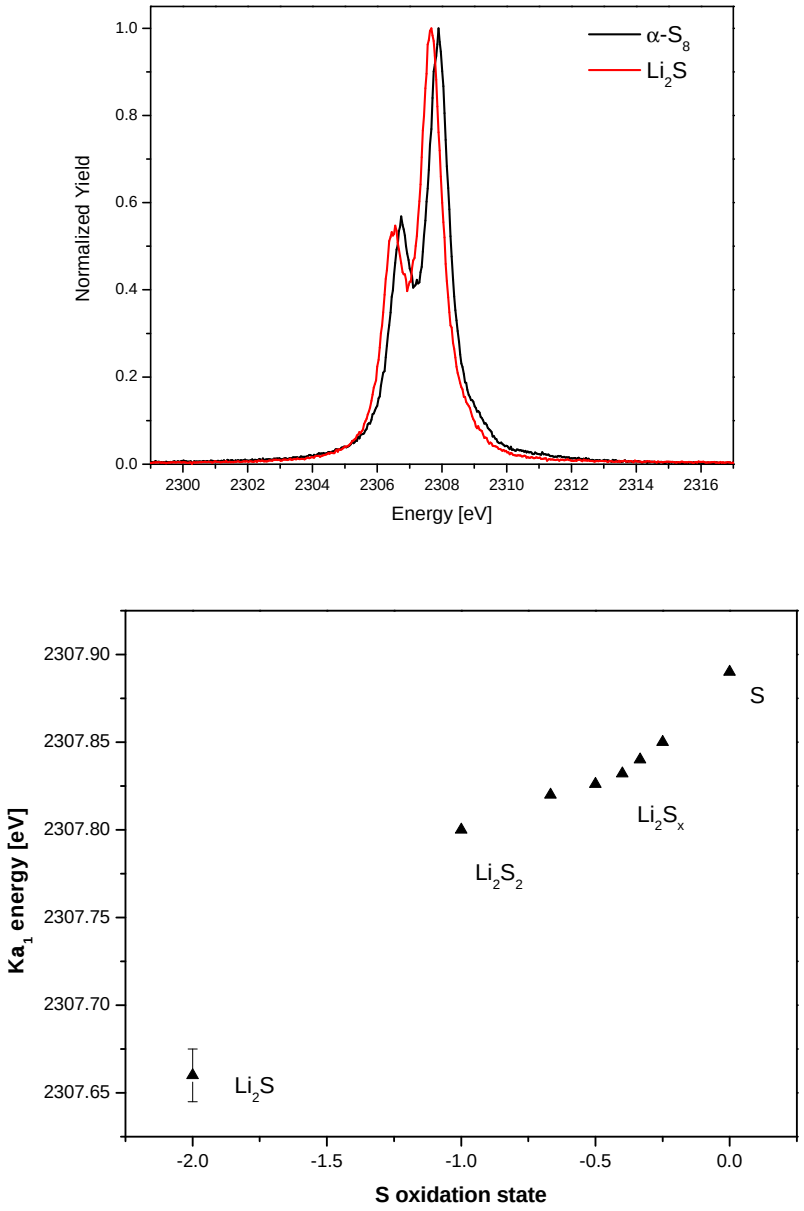


Figure 4.19: (*upper*) The high energy resolution S $K\alpha$ spectra of α-S_8 and Li_2S compounds. (*bottom*) The experimental $K\alpha_1$ x-ray emission energies versus the effective oxidation state.

Table 4.15: Electron density on the various Li_2S_x polysulfides calculated by Bader analysis.

	Calculated by StoBe		Ref.[118]	
Li_xS_x	Terminal	Internal	Terminal	Internal
2	-0.943	-	-0.845	-
3	-0.804	-0.250	-0.735	-0.189
4	-0.744	-0.185	-0.686	-0.189
5	-0.729	-0.131	-0.670	-0.142

Table 4.16: The results of Mulliken population analysis for the Li_2S_x compounds. In the last column the difference between the electronic charge on the terminal and internal sulfur atoms is given.

	Terminal[3s-3p-3d]	Internal[3s-3p-3d]	difference
2	1.931-4.335-0.022	-	
3	1.951-4.271-0.028	1.972-3.903-0.065	0.348
4	1.950-4.254-0.031	1.951-3.935-0.070	0.279
5	1.956-4.256-0.031	1.948-3.950-0.070	0.275

effective charge should be somewhere between the two values so very tiny energy shifts might be predicted providing an experimental signature of the Li polysulfide chain length.

In order to verify this, first the *ab-initio* DFT calculations were performed for Li_2S_x (x=2, 3, 4, and 5) systems. On the ground state of our systems the Mulliken population analysis was made and also Bader analysis yielding the electron density on the sulfur atom. The results are presented in Tables 4.16 and 4.15, respectively. For comparison, results of a more elaborated theoretical approach [118] considering also the electrolyte is also presented in Table 4.15. Most importantly, both analyses, Mulliken and Bader, suggest that the S atoms can be divided into two groups: terminal and internal. The internal S atoms are directly bound to two neighboring S atoms and the electron density is lower compared to terminal S atoms which are at the end of the sulfur chain. Larger effective electronic charge results in lower $K\alpha_1$ emission energy. This can be applied to the Li-S system, the terminal S atoms with larger electronic charge should yield lower energy of the $K\alpha$ emission line, when in case of the internal S atoms the energy of the $K\alpha$ line should be slightly higher. Both types of atoms contribute to the S $K\alpha$ x-ray emission spectrum and measured emission energy reflects the average values, which depend on the length of the Li_2S_x polysulfide.

For the experimental verification our former RIXS measurements on a reference set of chemically prepared Li_2S_x polysulfide standards [119] was used. In the RIXS experiment a sequence of $K\alpha$ emission spectra is recorded while scanning the energy of incident monochromatic x-ray beam across the sulfur K absorption edge building a two-dimensional RIXS map. For the purpose of our study the S $K\alpha$ spectra from the end of the RIXS maps, with excitation energy of 2485 eV where the spectrum is already fully developed, were considered. In Figure 4.19 the measured $K\alpha$ spectra of Li_2S and elemental α-S_8 samples are presented. In order to extract experimental energies, the $K\alpha_{1,2}$ emission lines were fitted with two Voigt functions. For the lithium polysulfides the "effective oxidation" can be defined as the number of Li atoms divided by the number of S atoms. The experimental $K\alpha_1$ emission energies can be plotted *versus* effective oxidation state for each polysulfides compounds and this is presented in Figure 4.19. A nice systematic dependence of the mea-

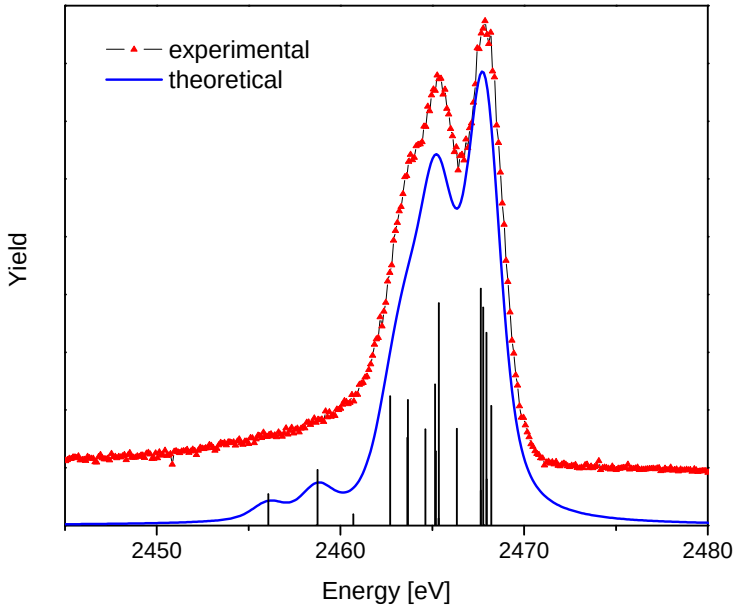


Figure 4.20: Experimental and theoretical S $K\beta$ emission spectrum of α-S_8 sample.

sured $K\alpha_1$ emission energies on the effective oxidation state is observed. $K\alpha$ XES could be therefore used to detect and specify Li_2S_x polysulfides produced in the Li-S battery during the discharge process.

In the next step the possibility to use VtC $K\beta$ x-ray emission spectra to analyze the electronic structure of sulfur within compounds produced in the Li-S battery during the discharge process was studied theoretically. We have started with the construction of the theoretical $K\beta$ x-ray emission model spectrum for the elemental S, which corresponds to the battery cathode in the initial state and can be also directly compared to the experimental spectrum. After the geometry optimization eight S atoms were arranged in a crystalline α-S_8 structure. In geometry optimization the same (73111/6111/1) basis set was used for all eight S atoms. In calculation of the S $K\beta$ x-ray emission spectrum seven S atoms were described by means of an effective core potential, to avoid linear combination of core-orbitals from neighboring atoms. For the atomic nucleus and electrons from K and L atomic shell electrostatic potential was used, while for the valence electrons (311/211/1) basis set was used. Only for the central S atom (73111/6111/1) basis set has been kept to calculate $K\beta$ spectrum. The theoretical spectrum was built from the calculated stick spectrum using Voigt profiles. The width of the Voigt profiles was adjusted in order to fit the experimentally observed lineshape, yielding the final width of 0.57 eV and 0.61 eV for the Gaussian and Lorentzian component, respectively. An overall shift of the absolute energy scale of 75.42 eV was applied to the theoretical spectrum in order to match experimental energies.

The experimental $K\beta$ emission line of elemental S has two characteristic close-lying components and the spectrum calculated on the theoretical α-S_8 model very well reproduces the experimental spectrum. The same theoretical framework can now be applied also to Li_2S_x molecular systems. In geometry optimization of each lithium polysulfide the basis set (73111/6111/1) was used for all S atoms. In the calculation of $K\beta$ XES the basis

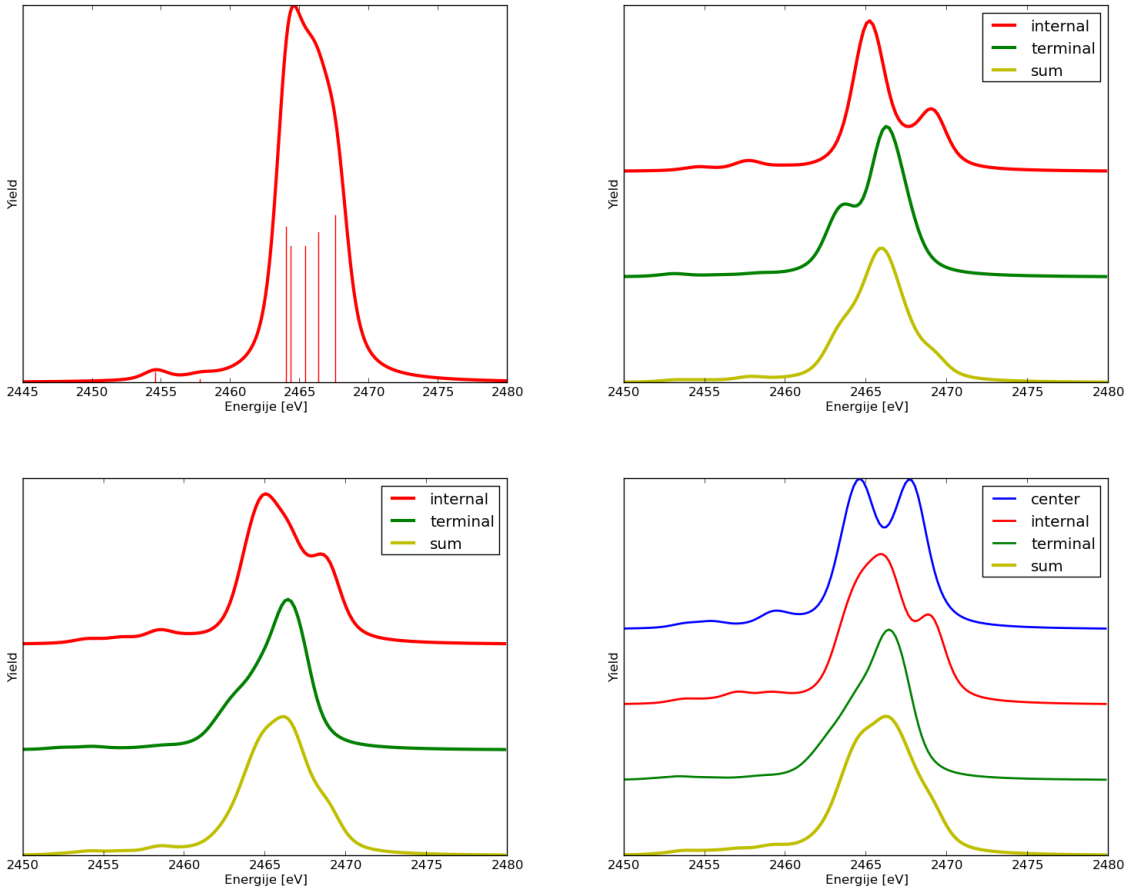


Figure 4.21: Theoretical S $K\beta$ x-ray emission spectra of Li_2S_2 (*left-up*), Li_2S_3 (*right-up*), Li_2S_4 (*left-bottom*), and Li_2S_5 (*right-bottom*) polysulfides.

set was then reduced in the same way as before. The core and valence electrons of all S atoms were described by core potential and (311/211/1) basis set, respectively. Again, the (73111/6111/1) basis set was used for the central S atom to calculate the $K\beta$ spectrum. Also in this case the model spectra were built from the calculated stick spectra, the overall shift and width of the Voigt profiles were the same as the ones used in the model spectrum of elemental S. The obtained theoretical spectra for Li_2S_x (x=2, 3, 4, and 5) molecules are presented in Figure 4.21.

In a rough description of the Li_2S_2 molecule, covalent bonding between two S atoms is assumed like in a diatomic molecule while the Li atoms are ionically bound to the S_2 molecule. Ionical bond does not change the electronic structure of the S_2 molecule, but each Li gives one electron to the molecule. This is confirmed with the Bader analysis in Table 4.15, where the calculated charge of the S atoms is -0.943. The calculations of the S $K\beta$ spectra were performed for both S atoms in Li_2S_2 molecule and the spectral shape is the same. In case of Li_2S_3, Li_2S_4, and Li_2S_5 molecules the S atoms are grouped in internal atoms and terminal atoms as already discussed previously and we need to separately calculate the emission spectrum for each S atom. Both terminal atoms have the same spectral shape which is similar for all calculated molecules and slightly differ from the spectral shape of internal atoms. In case of the Li_2S_5 molecule the central S atom has a different spectral shape from other internal atoms and needs to be treated separately. The final S $K\beta$ spectra were built as a sum of separate spectra of each S atom.

The sensitivity of VtC XES to the electronic structure of S within different Li_2S_x polysulfides is confirmed by our calculations. The theoretical $K\beta$ x-ray emission spectra exhibit distinct changes which could be used as a fingerprint for particular polysulfide species produced in Li-S battery during the discharge process. Due to the general experimental problem, which is a lack of clean single phase lithium polysulfide materials preventing to measure reliable reference spectra, our calculated data are not directly compared to the experiment. However, the analytical potential of x-ray emission spectroscopy to characterize sulfur electrochemical processes within Li-S battery is confirmed by our study. As already mentioned and demonstrated in our work, XES spectroscopy can be performed with laboratory excitation sources. In addition the techniques are perfectly compatible with *in-situ* conditions. *In-operando* sulfur XES measurements therefore provide a new promising analytical tool, which could yield insight into the mechanism of lithium-polysulfide formation in the Li-S battery.

Chapter 5

Conclusions

X-ray emission spectroscopy (XES) in the tender x-ray range has been used to study the electronic structure of phosphorus, sulfur and chlorine. Target x-ray fluorescence was induced by MeV proton beam provided by the MV Tandem accelerator at the J. Stefan Institute. The $K\alpha$ core-to-core (CtC) and $K\beta$ valence-to-core (VtC) x-ray emission spectra from a series of phosphorus, sulfur, and chlorine containing compounds covering the full range of oxidation states and different local symmetries were recorded by the in-vacuum curved-crystal tender x-ray emission spectrometer in the Johansson geometry. The spectrometer provided energy resolution on the level of the natural core-hole lifetime broadening of the corresponding third-row elements. In case of phosphorus compounds, additional measurements using monochromatic synchrotron radiation were performed at the European Synchrotron Radiation Facility (ESRF) verifying experimentally that the measured spectral shape is independent from the type of excitation.

In order to interpret spectral features, e.g. energy position and spectral shape, the *ab-initio* quantum chemical calculations were performed using the StoBe-deMon molecular cluster package based on the density functional theory (DFT). DFT framework allows us to find the ground state of the molecular system on which the CtC and VtC x-ray emission spectra were calculated. The theoretical spectra were compared with the measured ones and spectral features were addressed to effective electronic charge and molecular orbital composition. In the study of molecular structure the Mulliken population analysis was used. The Mulliken population analysis represents a conceptual link between the calculated electron cloud, obtained by solving quantum equations, and the classical picture of the atomic orbital.

The shape of $K\alpha$ emission line corresponding to CtC electron transition was found independent from the chemical environment. Small chemical shifts of the $K\alpha$ emission line were recorded on a series of measured compounds, which were correlated with the formal oxidation number. The correlation was improved even further using the effective charge based on the DFT calculated valence electron population. The energy position of $K\alpha$ line reflects with high sensitivity the local electronic charge on the P, S, and Cl elements and can be used effectively to determine the oxidation state of low-Z elements in different chemical environments. Good selectivity between different oxidation states can be used to decompose and analyze also mixed valence systems. The method is applicable to diluted samples with concentrations in the range of a few 1000 ppm for MeV proton excitation and can be lowered down to 100 ppm for photoexcitation employing high photon flux delivered by the synchrotron.

The $K\beta$ x-ray emission spectrum corresponds to electron transitions from valence orbitals and directly reflects the chemical bonding and local symmetry of the investigated molecular system. The $K\beta$ XES spectra of P, S, and Cl in different compounds exhibiting

T_d, C_{3v}, and C_{2v} local symmetry were systematically studied. In case of compounds with T_d local symmetry, the spectral shape is characterized by two main peaks, $K\beta'$ and $K\beta_{1,3}$. The $K\beta'$ peak, on the lower energy side of the spectrum, corresponds to electron transitions from $3t_2$ MO. Using the Mulliken population analysis and molecular orbital diagram, the origin of the $3t_2$ MO was assigned to bonding between O $2s$ and X $3p$ atomic orbitals. The K$\beta_{1,3}$ peak was addressed to the electron transition from $4t_2$ MO, which was constructed from O $2p$ and X $3p$ atomic orbitals. Compared with molecular systems of T_d local symmetry small changes were observed in the measured spectra of C_{3v} molecular systems. Additional spectral component $K\beta_{xx}$ appeared at the high energy side of the main $K\beta_{1,3}$ peak and the $K\beta'/K\beta_{1,3}$ intensity ratio has decreased. The formation of a new peak $K\beta_{xx}$ is explained by a different formation of MO due to changes in the geometry of the molecule. The X $3p$ atomic orbital is perpendicular to the plane formed by three oxygen atoms and cannot form σ bonds but only π-type bonds with O $2p$ orbitals. The π bonding MO contributes to the main $K\beta_{1,3}$ peak and π antibonding MO with higher energy contributes to the $K\beta_{xx}$ peak on the high energy side. On the other hand, this additional $K\beta_{xx}$ peak is absent in the measured $K\beta$ emission spectra of compounds with a hydrogen atom bonded directly to the central atom, which perturbs the electronic structure. This is demonstrated by the DFT calculations for the Na_2HPO_3 molecule where all positions of atoms were fixed, while the distance between H atom and Na_2PO_3 molecular fragment was varied showing that the $K\beta$ spectrum starts to develop the $K\beta_{xx}$ peak when the H atom is moved away from the rest of the molecule. The decreased $K\beta'/K\beta_{1,3}$ intensity ratio for molecular systems in C_{3v} symmetry is explained by the absence of one out of three degenerate $3t_2$ MO contributing to the $K\beta'$ peak in systems with T_d symmetry. In molecules with C_{3v} local symmetry the overlap integral of X $3p$ atomic orbital perpendicular to the oxygen plane with oxygen $2s$ orbitals is zero so the X $3p$ atomic orbital cannot form MO with oxygen $2s$ resulting in reduced $K\beta'/K\beta_{1,3}$ intensity ratio. Reducing the symmetry even further down to C_{2v}, the calculated electronic structure was found very similar to the structure of C_{3v} systems yielding also similar $K\beta$ measured spectral shape. However, in case of C_{2v} local symmetry only one $3t_2$ MO contributes to the $K\beta'$ peak intensity resulting in further decrease of the $K\beta'/K\beta_{1,3}$ intensity ratio. The approach used here to describe the main $K\beta$ spectral features of the small basic molecular systems with well-defined symmetries can serve as a starting point for more complex studies of a larger molecular system. This is demonstrated on the example of sodium metabisulfite ($Na_2P_2O_5$). The measured S $K\beta$ x-ray emission spectrum was well reproduced by the theoretical model spectrum built of a combination as smaller molecular blocks with C_{3v} and C_{2v} local symmetries.

The main $K\beta$ x-ray emission spectral features were quite well reproduced by the DFT calculations including only the first coordination sphere around the central atom. While metallic cations in the second coordinate sphere bound ionically to the central ion do not change the electronic structure, significant effects of the second coordinate sphere were recognized in the measured spectra of phosphate compounds. In the measured phosphate compounds containing a different number of hydrogen atoms the increasing intensity of $K\beta_x$ and $K\beta''$ side peaks with additional hydrogen atoms bound to the phosphate ion was observed. This dependence was confirmed also by the calculations and was addressed to the changes of the atomic character of the valence orbitals. In the PO_4^{3-} ion the predominantly s-type MO gets a significant amount of additional phosphorus $3p$ contribution with additional hydrogen atoms in the second coordinate sphere. These H atoms form covalent bonds with the phosphate ion sharing the electron between them, which perturbs significantly the electronic structure.

Based on the results of this work, we can conclude that XES in the tender x-ray range is a sensitive probe of the chemical environment of P, S, and Cl atoms and can be used

effectively for the analysis of their electronic structure in different bulk materials. As an interesting example, the theoretical analysis of the sulfur characterization in Li_2S_x systems performed by XES is presented. This particular case is motivated by the need to acquire precise information about local environment of S in the cathode of the high energy density Lithium-Sulfur battery during its operation. In general, XES technique in the tender x-ray range provides a powerful analytical tool and can be used complementary to XAS technique implemented commonly at the 3^{rd} generation synchrotron sources. Compared to XAS, the XES method could be used also at the hard x-ray beamlines which cannot reach the energies of K absorption edges of third-row elements situated in the tender range. Finally, the method is compatible with the laboratory excitation sources used in standard x-ray fluorescence techniques. Such analysis is therefore no longer restricted to synchrotrons but can be performed also in smaller laboratories. In our work, XES have been successfully coupled to MeV proton excitation and the analytical capabilities of the standard proton-induced x-ray emission (PIXE) technique, used to determine the elemental composition of the sample, have been extended also towards chemical speciation.

Appendix A

Mulliken Population Analysis of Phosphorus Compounds

For comparison, the results of the Mulliken analysis yielding atomic character for each of the separate molecular orbitals used to build the model phosphorus Kβ emission spectra are presented. Tabulated values were used also to calculate the average atomic character of the main spectral components presented in Tables 4.10 and 4.13. The calculated energies and relative intensities of each MO are also presented.

Table A.1: Atomic orbital contributions to the molecular orbitals used to build the K_3PO_4 model spectra. Besides atomic character calculated energies and intensities corresponding to electronic transition to 1s atomic orbital are also given. An overall shift of absolute calculated energies by -3.61 eV used to match experimental energies is already applied in the tabulated energies.

Spectroscopic label	Energy [eV]	Intensity %	AO orbital population [%]						
			P 3s	P 3p	P 3d	O 2s	O 2p	K 3s	K 3p
	2123.810	0.198	0	4	1	83	2	0	9
$K\beta'$	2124.243	0.404	0	8	2	77	4	0	9
	2124.983	0.403	0	8	2	77	3	0	9
$K\beta_x$	2135.956	0.028	27	1	0	26	44	0	0
	2138.254	1.000	0	24	0	6	68	0	0
$K\beta_{1,3}$	2138.142	0.998	0	24	0	11	62	0	0
	2137.653	0.997	0	24	0	12	63	0	0
$K\beta''$	2140.478	0.031	0	1	3	0	90	4	1
	2139.154	0.032	0	1	3	0	90	4	0

Table A.2: Atomic orbital contributions to the molecular orbitals used to build the Na_2HPO_4 model spectra. An overall shift of absolute calculated energies by -4.35 eV is already applied.

Spectroscopic label	Energy [eV]	Intensity %	AO orbital population [%] P 3s	P 3p	P 3d	O 2s	O 2p	Na2s/2p	H 1s
	2123.406	0.179	4	3	1	82	6	1	1
$K\beta'$	2121.037	0.473	0	8	1	84	4	1	0
	2123.793	0.434	0	7	1	86	4	0	0
$K\beta_x$	2133.264	0.274	15	6	0	10	55	0	13
	2136.485	0.316	13	6	0	19	54	0	6
	2137.596	1.000	0	23	0	9	65	1	1
$K\beta_{1,3}$	2138.045	0.949	0	22	0	12	63	1	0
	2138.709	0.578	0	13	1	9	71	0	3
	2139.798	0.043	0	1	4	0	90	4	0
$K\beta''$	2139.936	0.032	0	8	4	0	83	3	0
	2140.427	0.033	0	7	4	0	84	2	0

Table A.3: Atomic orbital contributions to the molecular orbitals used to build the NaH_2PO_4 model spectra. An overall shift of absolute calculated energies by -4.38 eV is already applied.

Spectroscopic label	Energy [eV]	Intensity %	AO orbital population [%] P 3s	P 3p	P 3d	O 2s	O 2p	H 1s
	2122.114	0.194	0	3	1	88	4	3
$K\beta'$	2123.599	0.316	5	5	0	79	7	1
	2123.632	0.851	0	8	1	84	5	0
	2132.904	0.388	16	6	0	9	57	11
$K\beta_x$	2134.686	0.688	0	11	1	1	70	15
	2136.530	0.200	9	7	0	17	60	6
	2137.602	1.000	2	18	0	9	67	2
$K\beta_{1,3}$	2138.073	0.880	0	16	0	11	68	2
	2139.168	0.816	0	11	1	9	76	2
$K\beta''$	2139.638	0.331	0	5	1	4	89	0

Table A.4: Atomic orbital contributions to the molecular orbitals used to build the KH_2PO_4 model spectra. An overall shift of absolute calculated energies by -3.77 eV is already applied.

Spectroscopic label	Energy [eV]	Intensity %	AO orbital population [%] P 3s	P 3p	P 3d	O 2s	O 2p	H 1s
	2122.637	0.206	0	3	1	87	3	3
$K\beta'$	2124.128	0.326	4	5	0	79	7	1
	2122.626	0.879	0	8	1	82	6	0
	2133.733	0.402	16	6	0	9	56	11
$K\beta_x$	2135.323	0.748	0	11	1	1	68	16
	2137.139	0.197	9	6	0	18	59	6
	2138.189	1.000	2	18	0	9	67	1
$K\beta_{1,3}$	2138.631	0.962	0	17	0	11	67	2
	2139.797	0.998	0	11	1	9	74	2
	2140.176	0.214	0	3	2	3	90	1
$K\beta''$	2140.302	0.047	0	7	2	0	88	2
	2141.750	0.046	0	2	2	0	93	1

Table A.5: Atomic orbital contributions to the molecular orbitals used to build the HPO_3^{2-} model spectra. An overall shift of absolute calculated energies by -3.89 eV is already applied.

Spectroscopic label	Energy [eV]	Intensity %	AO orbital population [%] P 3s	P 3p	P 3d	O 2s	O 2p	H 1s
$K\beta'$	2124.644	0.430	0	9	2	85	4	0
	2123.886	0.428	0	9	2	85	4	0
$K\beta_x$	2134.500	0.240	30	7	0	20	22	19
$K\beta_{1,3}$	2137.394	0.983	3	30	0	5	44	16
	2138.261	1.000	0	20	0	10	69	0
	2137.903	0.998	0	20	0	10	69	0

Table A.6: Atomic orbital contributions to the molecular orbitals used to build the $H_2PO_2^{1-}$ model spectra. An overall shift of absolute calculated energies by -3.36 eV is already applied.

Spectroscopic label	Energy [eV]	Intensity %	AO orbital population [%] P 3s	P 3p	P 3d	O 2s	O 2p	H 1s
$K\beta'$	2124.557	0.393	0	12	0	81	4	0
$K\beta_x$	2133.455	0.249	40	10	0	15	6	27
$K\beta_{1,3}$	2137.125	1.000	0	44	0	0	18	37
	2138.096	0.696	3	26	0	10	52	8
	2138.722	0.742	0	18	0	14	67	0

Appendix B

The Example of StoBe-deMon Code

The example of the StoBe code for SO_4^{2-} anion is presented in Listing B.1. In this example the symmetry of the molecule is defined with keywords `SYMM Td` in the 4^{th} row. The position coordinates of the S and O atoms are given in the 6^{th} and 7^{th} rows with the nuclear charge of atoms. In case of non-symmetry restriction the `NOSYMM` keyword was used and the position for each atom needed to be defined. The exchange and correctional functional used in the thesis are defined in the 11^{th} row by keywords `BE88` and `PD91`, respectively. It is important to define the molecular spin and charge, which is done in the 13^{th} and the 14^{th} row of the code. In the 20^{th} row the keyword for calculation of the x-ray emission spectrum is defined. The numbers after the `XRAY XES 1 1` keyword define the number of vacancies and the ordinal number of orbit in which the vacancy is constructed, respectively. Also, important for the calculation is to define the Gaussian basis sets and auxiliary basis sets for each atom, which is done in rows $26^{th} - 29^{th}$.

More details about the code can be found on the web page of the code [84] and in the manual of R. Bohinc [120].

Listing B.1: StoBe-deMon code.

```
cat >SO4_XES_SYMM.inp <<.
title
SO4 Td symmetry
SYMM Td
cartesian ANGSTROM
S       0.00000000    0.00000000    0.00000000    16.0      60
O       0.88967675    0.88967675    0.88967675     8.0      50
END
RUNTYPE START
SCFTYPE DIRECT
POTENTIAL NONLOCAL BE88 PD91
GRID FINE NONRANDOM
MULTIPLICITY 1
CHARGE -2
maxcycles 100
ECONVERGENCE 0.0000001
DCONVERGENCE 0.000001
DMIXING MDENS 0.20
DIIS ON
XRAY XES 1 1
END
```

```
FSYM SCFO
ALFA 5 0 2 3 15
BETA 5 0 2 3 15
END
A-SULFUR (5,4;5,4)
A-OXYGEN (5,2;5,2)
O-SULFUR (73111/6111/1)
O-OXYGEN (6311/311/1)
END
/.
```

References

[1] T. Johansson, R. Akselsson, and S. Johansson, *Nucl. Instrum. Meth.*, vol. 84, no. 1, pp. 141–143, 1970.

[2] F. de Groot and A. Kotani, *Core Level Spectroscopy of Solids*. Taylor and Francis Group, 2008.

[3] P. Glatzel and A. Juhin, *Local Structural Characterisation*, D. W. Bruce, D. O'Hare, and R. I. Walton, Eds. John Wiley & Sons, 2014.

[4] M. Kavčič, M. Budnar, A. Mühleisen, F. Gasser, M. Žitnik, K. Bučar, and R. Bohinc, *Rev. Sci. Instrum.*, vol. 83, no. 3, p. 03 311, 2012.

[5] C. Schlesiger, L. Anklamm, H. Stiel, W. Malzer, and B. Kanngiesser, *J. Anal. At. Spectrom.*, vol. 30, pp. 1080–1085, 5 2015.

[6] H. G. J. Moseley, *Phil. Mag.*, vol. 26, p. 1024, 1913.

[7] N.A.Dyson, *X-ray in Atomic and Nuclear Physics*. Cambridge University Press, 1990.

[8] S. A. E. Johansson and J. L. Campbell, *PIXE: A Novel Technique for Elemental Analysis*. John Wiley and Sons, 1988.

[9] E. Gallo and P. Glatzel, *Adv. Mater.*, vol. 26, no. 46, pp. 7730–7746, 2014.

[10] C. J. Pollock and S. DeBeer, *Acc. Chem. Res.*, vol. 48, no. 11, pp. 2967–2975, 2015.

[11] H. Marschner, *Mineral Nutrition of Higher Plants*. London: Academic Press, 1995.

[12] F. J. Maathuis, *Current Opinion in Plant Biology*, vol. 12, no. 3, pp. 250–258, 2009.

[13] L. B. Sheard, X. Tan, H. Mao, J. Withers, G. Ben-Nissan, T. R. Hinds, Y. Kobayashi, F.-F. Hsu, M. Sharon, J. Browse, S. Y. He, J. Rizo, G. A. Howe, and N. Zheng, *Nature*, vol. 468, pp. 400–405, 2010.

[14] F. Westheimer, *Science*, vol. 235, no. 4793, pp. 1173–1178, 1987.

[15] C. R. Benitez-Nelson, *Earth-Sci. Rev.*, vol. 51, no. 1–4, pp. 109–135, 2000.

[16] A. Paytan and K. McLaughlin, *Chem. Rev.*, vol. 107, no. 2, pp. 563–576, 2007.

[17] M. F. Crass, *J. Chem. Educ.*, vol. 18, no. 6, p. 277, 1941.

[18] D. Cordell, J. O. Drangert, and S. White, *Global Environmental Change*, vol. 19, no. 2, pp. 292–305, 2009.

[19] V. Smil, *Annual Review of Energy and the Environment*, vol. 25, no. 1, pp. 53–88, 2000.

[20] D. Kumar, W. Thiel, and S. P. de Visser, *J. Am. Chem. Soc.*, vol. 133, no. 11, pp. 3869–3882, 2011.

[21] D. Manna, G. Roy, and G. Mugesh, *Acc. Chem. Res.*, vol. 46, no. 11, pp. 2706–2715, 2013.

[22] C. Sugiura, Y. Gohshi, and I. Suzuki, *Phys. Rev. B*, vol. 10, pp. 338–343, 2 1974.

[23] P. S. Farrell and E. M. Fleet, *Phys. and Chem. of Minerals*, vol. 28, no. 1, pp. 17–27, 2001.

[24] G. U. v. Oertzen, R. T. Jones, and A. R. Gerson, *Phys. and Chem. of Minerals*, vol. 32, no. 4, pp. 255–268, 2005.

[25] M. E. Fleet, *Can. Miner.*, vol. 43, no. 6, pp. 1811–1838, 2005.

[26] M. Frosch, M. Bilde, and O. F. Nielsen, *J. Phys. Chem. A*, vol. 114, no. 44, pp. 11 933–11 942, 2010.

[27] T. Berndt, O. Böge, F. Stratmann, J. Heintzenberg, and M. Kulmala, *Science*, vol. 307, no. 5710, pp. 698–700, 2005.

[28] A. Manthiram, Y. Fu, S.-H. Chung, C. Zu, and Y.-S. Su, *Chem. Rev.*, vol. 114, no. 23, pp. 11 751–11 787, 2014.

[29] S. Kelemen, G. George, and M. Gorbaty, *Fuel*, vol. 69, no. 8, pp. 939–944, 1990.

[30] G. P. Huffman, S. Mitra, F. E. Huggins, N. Shah, S. Vaidya, and F. Lu, *Energy and Fuels*, vol. 5, no. 4, pp. 574–581, 1991.

[31] G. S. Waldo, O. C. Mullins, J. E. Penner-Hahn, and S. Cramer, *Fuel*, vol. 71, no. 1, pp. 53–57, 1992.

[32] H. G. Gorchev, *Pure Appl. Chem.*, vol. 68, no. 9, pp. 1731–1735, 1996.

[33] K. Ballschmiter, *Pure Appl. Chem.*, vol. 68, no. 9, pp. 1771–1780, 1996.

[34] G. W. Gribble, *Pure Appl. Chem.*, vol. 68, no. 9, pp. 1699–1712, 1996.

[35] J. D. Coates and L. A. Achenbach, *Nat. Rev. Micro.*, vol. 2, pp. 569–580, 2004.

[36] W. A. Jackson, A. F. Davila, D. W. Sears, J. D. Coates, C. P. McKay, M. Brundrett, N. Estrada, and J. Böhlke, *Earth Planet. Sci. Lett.*, vol. 430, pp. 470–476, 2015.

[37] J. Fauvarque, *Pure Appl. Chem.*, vol. 68, no. 9, pp. 1713–1720, 1996.

[38] M. J. Molina, *Pure Appl. Chem.*, vol. 68, no. 9, pp. 1749–1756, 1996.

[39] K. Maeda, A. Tonomura, H. Hamanaka, and K. Hasegawa, *Nucl. Instrum. Meth. Phys. Res. B*, vol. 150, no. 1–4, pp. 124–128, 1999.

[40] T. Tada, H. Fukuda, J. Hasegawa, and Y. Oguri, *Spectrochim. Acta, Part B*, vol. 65, no. 1, pp. 46–50, 2010.

[41] M. Kavčič, A. Karydas, and C. Zarkadas, *Nucl. Instrum. Meth. Phys. Res. B*, vol. 222, no. 3–4, pp. 601–608, 2004.

[42] M. Kavčič, A. G. Karydas, and C. Zarkadas, *X-ray Spectrom.*, vol. 34, no. 4, pp. 310–314, 2005.

[43] K. Maeda, K. Hasegawa, H. Hamanaka, M. Maeda, S. Yabuki, and K. Ogiwara, *Nucl. Instrum. Meth. Phys. Res. B*, vol. 190, no. 1–4, pp. 704–708, 2002.

[44] S. Wonglee, T. Tada, H. Fukuda, J. Hasegawa, and Y. Oguri, *Nucl. Instrum. Meth. Phys. Res. B*, vol. 269, no. 24, pp. 3111–3114, 2011.

[45] Z. Kertész, E. Furu, and M. Kavčič, *Spectrochim. Acta, Part B*, vol. 79 - 80, no. 0, pp. 58–62, 2013.

[46] R. Alonso Mori, E. Paris, G. Giuli, S. G. Eeckhout, M. Kavčič, M. Žitnik, K. Bučar, L. G. M. Pettersson, and P. Glatzel, *Anal. Chem.*, vol. 81, no. 15, pp. 6516–6525, 2009.

[47] C. Sugiura, *J. Phys. Soc. Jpn.*, vol. 64, no. 3, pp. 848–857, 1995.

[48] C. Sugiura, H. Yorikawa, and S. Muramatsu, *J. Phys. Soc. Jpn.*, vol. 65, no. 9, pp. 2940–2945, 1996.

[49] Y. Takahashi, *Bull. Chem. Soc. Jpn.*, vol. 45, no. 1, pp. 4–7, 1972.

[50] M. T. Deluigi, E. Perino, R. Olsina, and A. R. de la Vega, *Spectrochim. Acta, Part B*, vol. 58, no. 9, pp. 1699–1707, 2003.

[51] M. T. Deluigi and J. Riveros, *Chem. Phys.*, vol. 325, no. 2–3, pp. 472–476, 2006.

[52] M. Kavčič, J.-C. Dousse, J. Szlachetko, and W. Cao, *Nucl. Instrum. Meth. Phys. Res. B*, vol. 260, no. 2, pp. 642–646, 2007.

[53] Y. Gohshi, *Adv. X-ray Anal.*, vol. 12, no. 12, p. 518, 1969.

[54] S. Ceppi, G. Tirao, G. Stutz, and J. A. Riveros, *Chem. Phys.*, vol. 354, no. 1–3, pp. 80–85, 2008.

[55] G. Karlsson and R. Manne, *Phys. Scripta*, vol. 4, no. 3, p. 119, 1971.

[56] U. Eiichirou, K. Jun, and M. Uda, *Nucl. Instrum. Meth. Phys. Res. B*, vol. 75, no. 1, pp. 24–27, 1993.

[57] R. A. Mori, E. Paris, G. Giuli, S. G. Eeckhout, M. Kavčič, M. Žitnik, K. Bučar, L. G. M. Pettersson, and P. Glatzel, *Inorg. Chem.*, vol. 49, no. 14, pp. 6468–6473, 2010.

[58] F. Schwabl, *Quantum Mechanics*. Springer-Verlag Berlin Heidelberg, 2007.

[59] H. A. Kramers and W. Heisenberg, *Zeitschrift fur Physik*, vol. 31, no. 1, pp. 681–708,

[60] J.-P. Rueff and A. Shukla, *Rev. Mod. Phys.*, vol. 82, pp. 847–896, 2010.

[61] A. Kotani and S. Shin, *Rev. Mod. Phys.*, vol. 73, pp. 203–246, 1 2001.

[62] P. Atkins and R. Friedman, *Molecular Quantum Mechanics*. Oxford University Press, 2005.

[63] F. Jensen, *Introduction to Computational Chemistry*. John Wiley & Sons, Chichester, 2007.

[64] H. Toffoli, *Lecture notes*, 2009.

[65] H. Eschrig, *The Fundamentals of Density Functional Theory*. B.G. Teubner Verlagsgesellschaft, Leipzig, 1996.

[66] R. G. Parr and W. Yang, *Density-Functional Theory of Atoms and Molecules*. Oxford University Press, 1989.

[67] L. H. Thomas, *Proc. Cambridge Phil. Soc.*, vol. 23, pp. 542–548, 05 Jan. 1927.

[68] E. Fermi, "Un metodo statistico per la determinazione di alcune proprieta dell'atomo," *Atti accad. Lincei*, vol. 6, pp. 602–607, 1927.

[69] P. Hohenberg and W. Kohn, *Phys. Rev.*, vol. 136, B864–B871, 3B Nov. 1964.

[70] W. Kohn and L. J. Sham, *Phys. Rev.*, vol. 140, A1133–A1138, 4A Nov. 1965.

[71] K. Capelle, *ArXiv:cond-mat/0211443*, 2006.

[72] W. Kohn, *Rev. Mod. Phys.*, vol. 71, pp. 1253–1266, 5 1999.

[73] D. M. Ceperley and B. J. Alder, *Phys. Rev. Lett.*, vol. 45, pp. 566–569, 7 1980.

[74] W. Koch and M. C. Holthausen, *A Chemist's Guide to Density Functional Theory*. John Wiley & Sons-VCH, 2001.

[75] R. Stowasser and R. Hoffmann, *J. Am. Chem. Soc.*, vol. 121, no. 14, pp. 3414–3420, 1999.

[76] E. J. Baerends, *Theor. Chem. Acc.*, vol. 103, no. 3-4, pp. 265–269, 2000.

[77] P. A. Hunt, *Lecture notes*, 2013.

[78] F. Jensen, *Introduction to Computational Chemistry, Second Ediion*. John Wiley and Sons, 2007.

[79] K. Hermann, L. Pettersson, M. Casida, C. Daul, A. Goursot, A. Koester, E. Proynov, A. St-Amant, D. Salahub., V. Carravetta, H. Duarte, C. Friedrich, N. Godbout, J. Guan, C. Jamorski, M. Leboeuf, M. Leetmaa, M. Nyberg, S. Patchkovskii, L. Pedocchi, F. Sim, L. Triguero, and A. Vela., *Stobe-demon version 3.1*, 2011.

[80] A. Nilsson and L. G. M. Pettersson, *Surface Science Reports*, vol. 55, no. 2–5, pp. 49–167, 2004.

[81] A. Föhlisch, J. Hasselström, P. Bennich, N. Wassdahl, O. Karis, A. Nilsson, L. Triguero, M. Nyberg, and L. G. M. Pettersson, *Phys. Rev. B*, vol. 61, pp. 16 229–16 240, 23 Jun. 2000.

[82] N. Godbout, D. R. Salahub, J. Andzelm, and E. Wimmer, *Can. J. Chem.*, vol. 70, no. 2, pp. 560–571, 1992.

[83] M. Leetmaa, M. Ljungberg, A. Lyubartsev, A. Nilsson, and L. Pettersson, *J. Electron Spectrosc. Rel. Phenom.*, vol. 177, no. 2-3, pp. 135–157, 2010.

[84] *Documentation for stobe2014*, `http://www.fhi-berlin.mpg.de/KHsoftware/StoBe/StoBeMAN.html`.

[85] A. Becke, *Phys. Rev. A*, vol. 38, pp. 3098–3100, 6 Sep. 1988.

[86] J. Perdew, J. Chevary, S. Vosko, K. Jackson, M. Pederson, D. Singh, and C. Fiolhais, *Phys. Rev. B*, vol. 46, pp. 6671–6687, 11 Sep. 1992.

[87] R. S. Mulliken, *J. Chem. Phys.*, vol. 23, no. 10, pp. 1833–1840, 1955.

[88] R. S. Mulliken, *J. Chem. Phys.*, vol. 23, no. 10, pp. 1841–1846, 1955.

[89] R. S. Mulliken, *J. Chem. Phys.*, vol. 23, no. 12, pp. 2338–2342, 1955.

[90] R. S. Mulliken, *J. Chem. Phys.*, vol. 23, no. 12, pp. 2343–2346, 1955.

[91] P. O. Lowdin, *J. Chem. Phys.*, vol. 18, no. 3, pp. 365–375, 1950.

[92] A. E. Reed, R. B. Weinstock, and F. Weinhold, *J. Chem. Phys.*, vol. 83, no. 2, pp. 735–746, 1985.

[93] G. L. Miessler, P. J. Fischer, and D. A. Tarr, *Inorganic Chemistry, 5e.* 2013.

[94] W. Brandt and G. Lapicki, "Energy-loss effect in inner-shell coulomb ionization by heavy charged particles," *Phys. Rev. A*, vol. 23, pp. 1717–1729, 4 1981.

[95] V. Horvat, *Computer Physics Communications*, vol. 180, no. 6, pp. 995–1003, 2009.

[96] W. Bambynek, B. Crasemann, R. W. Fink, H. U. Freund, H. Mark, C. D. Swift, and R. P. Price R. E. an Venugopala, "X-ray fluorescence yields, auger, and coster-kronig transition probabilities," *Rev. Mod. Phys.*, vol. 44, pp. 716–813, 4 1972.

[97] P. Pelicon, N. C. Podaru, P. Vavpetič, L. Jeromel, N. O. Potocnik, S. Ondračka, A. Gottdang, and D. J. Mous, *Nucl. Instrum. Meth. Phys. Res. B*, vol. 332, pp. 229–233, 2014.

[98] R. A. Mori, "Sulfur-metal interactions in silicate glasses studied by x-ray spectroscopy," PhD thesis, ESFR, Grenoble-France, 2009.

[99] J. Campbell and T. Papp, *Atomic Data and Nuclear Data Tables*, vol. 77, no. 1, pp. 1–56, 2001.

[100] W. H. Bragg and W. L. Bragg, *Proceedings of the Royal Society of London A: Mathematical, Physical and Engineering Sciences*, vol. 88, no. 605, pp. 428–438, 1913.

[101] C. G. Darwin, *Philos. Mag.*, vol. 27, pp. 315–333, 1914.

[102] J. Als-Nielsen and D. McMorrow, *Elements of Modern X-ray Physics*. John Wiley and Sons, 2011.

[103] L. Hámos, *Naturwissenschaften*, vol. 20, no. 38, pp. 705–706, 1932.

[104] H. H. Johann, *Zeitschrift für Physik*, vol. 69, no. 3, pp. 185–206, 1931.

[105] T. Johansson, *Zeitschrift für Physik*, vol. 82, no. 7, pp. 507–528, 1933.

[106] M. Fichter, *Spectrochim. Acta Part B*, vol. 30, no. 10–11, pp. 417–431, 1975.

[107] R. D. Deslattes, E. G. Kessler, P. Indelicato, L. de Billy, E. Lindroth, and J. Anton, *Rev. Mod. Phys.*, vol. 75, pp. 35–99, 2003.

[108] C. Sugiura, *Phys. Rev. B*, vol. 6, pp. 1709–1713, 1972.

[109] M. Kavčič, *Nucl. Instrum. Meth. Phys. Res. B*, vol. 268, no. 22, pp. 3438–3442, 2010.

[110] V. Voronin, Y. Ponosov, I. Berger, N. Proskurnina, V. Zubkov, A. Tyutyunnik, S. Bushmeleva, A. Balagurov, D. Sheptyakov, E. Burmakin, G. Shekhtman, and E. Vovkotrub, *Inorg. Mater.*, vol. 42, no. 8, pp. 908–913, 2006.

[111] J. A. McGinnety, *Acta Crystallographica Section B*, vol. 28, no. 9, pp. 2845–2852, 1972.

[112] N. Mani, *Proceedings of the Indian Academy of Sciences - Section A*, vol. 46, no. 2, pp. 143–151, 1957.

[113] N. Sofina, R. Dinnebier, and M. Jansen, *Zeitschrift fur anorganische und allgemeine Chemie*, vol. 631, no. 15, pp. 2994–2996, 2005.

[114] S. C. Abrahams and J. L. Bernstein, *Acta Crystallographica Section B*, vol. 33, no. 11, pp. 3601–3604, 1977.

[115] H. Adachi and K. Taniguchi, *J. Phys. Soc. Jpn.*, vol. 49, no. 5, pp. 1944–1953, 1980.

[116] K. L. Carter, T. A. Siddiquee, K. L. Murphy, and D. W. Bennett, *Acta Crystallogr., Sect. B: Struct. Sci.*, vol. 60, no. 2, pp. 155–162, 2004.

[117] R. Dominko, M. U. M. Patel, V. Lapornik, A. Vizintin, M. Koželj, N. N. Tušar, I. Arčon, L. Stievano, and G. Aquilanti, *J. Phys. Chem. C*, vol. 119, no. 33, pp. 19 001–19 010, 2015.

[118] T. A. Pascal, K. H. Wujcik, J. Velasco-Velez, C. Wu, A. A. Teran, M. Kapilashrami, J. Cabana, J. Guo, M. Salmeron, N. Balsara, and D. Prendergast, *J. Phys. Chem. Lett.*, vol. 5, no. 9, pp. 1547–1551, 2014.

[119] M. Kavčič, K. Bučar, M. Petric, M. Žitnik, I. Arčon, R. Dominko, and A. Vizintin, *J. Phys. Chem. C*, vol. 120, no. 43, pp. 24 568–24 576, 2016.

[120] R. Bohinc, *Priročnik za uporabo programskega paketa stobe*.

Bibliography

Publications Related to the Thesis

Journal Articles

M. Petric, R. Bohinc, K. Bučar, M. Žitnik, J. Szlachetko, and M. Kavčič, *Anal. Chem.*, vol. 87, no. 11, pp. 5632–5639, 2015.

M. Petric and M. Kavčič, *J. Anal. At. Spectrom.*, vol. 31, pp. 450–457, 2016.

M. Petric, R. Bohinc, K. Bučar, S. H. Nowak, M. Žitnik, and M. Kavčič, *Inorg. Chem.*, vol. 55, no. 11, pp. 5328–5336, 2016.

Conference Paper

M. Petric, K. Bučar, M. Žitnik, and M. Kavčič, *Proceedings of the 8th Jožef Stefan International Postgraduate School Students' Conference*, pp. 261–272, 2016.

Other Publications

Journal Articles

T. Marchenko, S. Carniato, L. Journel, R. Guillemin, E. Kawerk, M. Žitnik, M. Kavčič, K. Bučar, R. Bohinc, M. Petric, V. Vaz da Cruz, F. Gel'mukhanov, and M. Simon, *Phys. Rev. X*, vol. 5, p. 031 021, 2015.

S. H. Nowak, A. Bjeoumikhov, J. von Borany, J. Buchriegler, F. Munnik, M. Petric, M. Radtke, A. D. Renno, U. Reinholz, O. Scharf, and R. Wedell, *J. Anal. At. Spectrom.*, vol. 30, pp. 1890–1897, 2015.

S. H. Nowak, A. Bjeoumikhov, J. von Borany, J. Buchriegler, F. Munnik, M. Petric, A. D. Renno, M. Radtke, U. Reinholz, O. Scharf, L. Strüder, R. Wedell, and R. Ziegenrücker, *X-Ray Spectrom.*, vol. 44, no. 3, pp. 135–140, 2015.

J. Niskanen, C. J. Sahle, K. O. Ruotsalainen, H. Müller, M. Kavčič, M. Žitnik, K. Bučar, M. Petric, M. Hakala, and S. Huotari, *Sci. Rep.*, vol. 6, no. 21012, 2016.

M. Kavčič, K. Bučar, M. Petric, M. Žitnik, I. Arčon, R. Dominko, and A. Vizintin, *J. Phys. Chem. C*, vol. 120, no. 43, pp. 24 568–24 576, 2016.